Investigation of Deformation Mechanisms in Strong and Ductile Alloys

Werner, Konstantin Victor

Publication date:
2023

Document Version
Publisher's PDF, also known as Version of record

Department of Civil and Mechanical Engineering
PhD Thesis

Investigation of Deformation Mechanisms in Strong and Ductile Alloys

Konstantin Victor Werner

Investigation of Deformation Mechanisms in Strong and Ductile Alloys

A THESIS SUBMITTED TO THE TECHNICAL UNIVERSITY OF DENMARK FOR THE DEGREE OF DOCTOR OF PHILOSOPHY IN THE DEPARTMENT OF CIVIL AND MECHANICAL ENGINEERING

June 2023

By

Konstantin Victor Werner

Technical University of Denmark

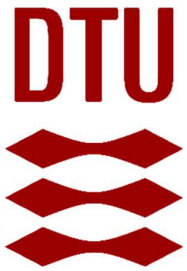

Department for Civil and Mechanical Engineering

Section of Materials and Surface Engineering

Investigation of Deformation Mechanisms in Strong and Ductile Alloys

A doctoral thesis by

Konstantin Victor Werner

E-Mail: Kviwe@mek.dtu.dk

Technical University of Denmark

Department of Civil and Mechanical Engineering - Section of Materials and Surface Engineering

Produktionstorvet 425, room 111

DK-2800 Kgs. Lyngby

Principal Supervisor:

Prof. Marcel A.J. Somers

E-Mail: somers@mek.dtu.dk

Technical University of Denmark

Department of Civil and Mechanical Engineering - Section of Materials and Surface Engineering

Produktionstorvet 425, room 120

DK-2800 Kgs. Lyngby

Co-Supervisor:

Senior researcher Matteo Villa

E-Mail: matv@mek.dtu.dk

Technical University of Denmark

Department of Civil and Mechanical Engineering - Section of Materials and Surface Engineering

Produktionstorvet 425, room 112

DK-2800 Kgs. Lyngby

Published by: Department of Civil and Mechanical Engineering, Section of Materials and Surface Engineering , Produktionstorvet, Building 425, DK-2800 Kgs. Lyngby

Preface

This doctoral thesis is submitted in partial fulfilment of the requirements for receiving the degree of Doctor of Philosophy (Ph.D.) at the Technical University of Denmark (DTU). The project was funded by the Independent Research Fund Denmark as part of the SFETailor project (Grant No. 9041- 00145B) and carried out at the Department of Civil and Mechanical Engineering, Section of Materials and Surface Engineering in the period January 1st, 2020 - June 12th, 2023. The project was supervised by Professor Marcel A. J. Somers and Senior researcher Matteo Villa from the Department of Civil and Mechanical Engineering, Section of Materials and Surface Engineering, DTU.

Declaration

I declare that, if not explicitly stated, none of the presented work in this doctoral thesis has been submitted in support of an application for another degree of this or any other university. I further declare that the presented work is my own work and that I have correctly acknowledged work of others.

Abstract

The stacking fault energy is an important factor in determining the types of plastic deformation mechanisms that occur in face-centered cubic materials and consequently influences their mechanical properties. Experimental observations have shown that as the stacking fault energy decreases, the deformation mechanism transitions from pure dislocation glide to a combination of twinning and dislocation glide, and eventually to a combination of martensite formation and dislocation glide at even lower stacking fault energy values. For austenitic steels, a stacking fault energy of 45 $mJ \cdot m^{-2}$ marks the lower limit for pure dislocation glide, while stacking fault energy values in the range of 20-45 $mJ \cdot m^{-2}$ result in a mixture of dislocation glide and twinning. When the stacking fault energy is even lower, materials tend to form martensite alongside dislocation glide. The presence of deformation twinning and martensite formation in addition to dislocation glide leads to higher work hardening rates compared to dislocation glide alone. Therefore, tailoring the mechanical properties by adjusting the stacking fault energy, such as through controlling the chemical composition, is considered a viable approach to create materials with unprecedented combinations of strength and ductility.

With the emergence of high-entropy alloys, computational materials engineering methods have become crucial for designing potentially promising compositions within the vast space of alloy compositions. Consequently, the computational determination of stacking fault energy, typically using density functional theory, has garnered significant interest. While experiments and density functional theory-based calculations generally agree on stacking fault energy values for stable face-

centered cubic materials, there are severe discrepancies for metastable face-centered cubic materials. Density functional theory calculations predict negative stacking fault energy values, whereas experimental values remain positive.

In this Ph.D. thesis, it was demonstrated that this discrepancy arises because density functional theory treats the stacking fault energy as a variable of state, unaffected by kinetic effects like the mobility of Shockley partial dislocations. In contrast, experimental stacking fault energy values are influenced by the resistance to the movement of Shockley partial dislocations. To reconcile the experimental and theoretical stacking fault energy values, it is proposed to subtract the excess stacking fault energy stemming from the resistance to the movement of Shockley partial dislocations from the experimental values. This correction assumes that the critical resolved shear stress for Shockley partial dislocations approximately corresponds to the critical resolved shear stress for twinning. By considering the correlation with the critical resolved shear stress for twinning, the correction can also explain the grain size dependence observed in experimental stacking fault energy values. Consequently, the corrected experimental values for metastable face-centered cubic materials become negative and align well with the stacking fault energy values obtained from density functional theory calculations. Moreover, this suggested correction has been tested on stable face-centered cubic alloys and pure metals, yielding consistent and quantitatively comparable results between experimental and theoretical stacking fault energy values for the first time.

Resumé

Stablingsfejlenergien er en vigtig faktor i bestemmelsen af de typer plastiske deformationsmekanismer, der forekommer i kubiske materialer med centreret overflade, og påvirker derfor deres mekaniske egenskaber. Eksperimentelle observationer har vist, at når stablingsfejlenergien falder, går deformationsmekanismen fra ren dislokationsglidning til en kombination af tvillings dannelse og dislokationsglidning, og til sidst til en kombination af martensitdannelse og dislokationsglidning ved endnu lavere stablingsfejlenergi. For austenitisk stål markerer en stablingsfejlenergi på 45 mJ/m^2 den nedre grænse for ren dislokationsglidning, mens stablingsfejlenergiværdier i området 20-45 mJ/m^2 resulterer i en blanding af dislokationsglidning og tvillings dannelse. Når stablingsfejlenergien er endnu lavere, har materialerne tendens til at danne martensit sammen med dislokationsglidning. Tilstedeværelsen af deformationstvillingsdannelse og martensitdannelse i tillæg til dislokationsglidning fører til højere arbejdshærdningshastigheder sammenlignet med dislokationsglidning alene. Derfor anses skræddersyning af de mekaniske egenskaber ved at justere stablingsfejlsenergien, f.eks. ved at kontrollere den kemiske sammensætning, for at være en levedygtig tilgang til at skabe materialer med hidtil usete kombinationer af styrke og duktilitet.

Med fremkomsten af høj-entropi lergeringer er beregningsmetoder inden for materialeteknik afgørende for at designe potentielt lovende sammensætninger inden for det store område af legeringssammensætninger. Derfor har den beregningsmæssige bestemmelse af stablingsfejlenergi, typisk ved hjælp af

tæthedsfunktionalteori, fået betydelig interesse. Mens eksperimentelle og tæthedsfunktionalteoribaserede beregninger generelt er enige om værdier for stablingsfejlsenergi for stabile kubisk fladecentreret materialer, er der uoverensstemmelser for metastabile kubisk fladecentreret materialer. Tæthedsfunktionalteoriberegninger forudsiger negative værdier for stablingsfejlsenergi, mens eksperimentelle værdier forbliver positive.

Denne uoverensstemmelse opstår, fordi tæthedsfunktionalteorien behandler stablingsfejlenergien som en termodynamisk størrelse, der ikke påvirkes af kinetiske effekter som bevægelsen af Shockley partielle dislokationer. I modsætning hertil er de eksperimentelle værdier for stablingsfejlsenergien påvirket af modstanden mod bevægelsen af Shockley partielle dislokationer. For at forene de eksperimentelle og teoretiske værdier for stablingsfejlsenergien foreslås det at trække modstanden mod bevægelsen af Shockley partielle dislokationer fra de eksperimentelle værdier. Denne korrektion forudsætter, at den kritiske opløste forskydningsspænding for Shockley partielle dislokationer omtrent svarer til den kritiske opløste forskydningsspænding for tvillings dannelse. Ved at overveje korrelationen med den kritiske opløste forskydningsspænding for tvillings dannelse, kan korrektionen også forklare den kornstørrelsesafhængighed, der er observeret i eksperimentelle stablingsfejlenergiværdier. Som følge heraf bliver de korrigerede eksperimentelle værdier for metastabile kubisk fladecentreret materialer negative og stemmer godt overens med værdierne for stablingsfejlenergien opnået fra beregninger med tæthedsfunktionalteori.

Desuden er denne foreslåede korrektion blevet testet på stabile kubisk fladecentreret legeringer og rene metaller, hvilket for første gang har givet konsistente og kvantitativt sammenlignelige resultater mellem eksperimentelle og teoretiske stablingsfejlenergiværdier.

List of Articles

Peer-reviewed articles included in this thesis

[1] **Werner, K. V.**, Niessen, F., Villa, M., Somers, M. A. J., "Experimental validation of negative stacking fault energies in metastable face-centered cubic materials", Appl. Phys. Lett. 119, 141902 (2021) https://doi.org/10.1063/5.0063761 **(Published)**

[2] **Werner, K. V.**, Niessen, F., Li, W., Lu, S., Vitos, L., Villa, M., Somers, M. A. J., "Reconciling experimental and theoretical stacking fault energies in face-centered cubic materials with the experimental twinning stress", Materialia, Vol. 27, 2023, https://doi.org/10.1016/j.mtla.2023.101708 **(Published)**

[3] **Werner, K. V.**, Muhammad, N., Niessen, F., Zhu, L., Villa, M., Wang, X.-L., Somers, M. A. J., "Experimental and computational assessment of the temperature dependency of the stacking fault energy in face-centered cubic high-entropy alloy", **(Ready for submission)**

Peer-reviewed articles not included in this thesis

[1] Niessen, F., Li, W., **Werner, K. V.**, Lu, S., Vitos, L., Villa, M., Somers, M. A. J., "Ab initio study of the effect of interstitial alloying on the intrinsic stacking fault energy of paramagnetic γ-Fe and austenitic stainless steel", Acta Materialia, Vol. 253, 2023, https://doi.org/10.1016/j.actamat.2023.118967 **(Published)**

[2] Wang, B., **Werner, K. V.**, Villa, M., Christiansen, T. L., Somers, M. A. J., "Phase stability and deformation modes in functionally graded metastable austenitic stainless steel; a novel approach to evaluate the role of nitrogen", Metall. Mater. Trans. A, 54, pp. 590–604 (2023), https://doi.org/10.1007/s11661-022-06904-x **(Published)**

[3] **Werner, K. V.**, Che, H. L., Lei, M. K., Christiansen, T. L., Somers, M. A. J., "Low Temperature Carburizing of Stainless Steels and the Development of Carbon Expanded Austenite", HTM Journal of Heat Treatment and Materials, Vol. 77, no. 1, 2022, pp. 3-15. https://doi.org/10.1515/htm-2022-0001 **(Published)**

Acknowledgement

First, I would like to express my deepest appreciation and gratitude to my main supervisor Professor Marcel A. J. Somers for his support, experience and knowledge, as well as for instilling trust in my knowledge and capabilities as well as myself when I was wavering. Thank you for all the five-minute long discussion that took often much longer, giving me the freedom to follow my own ideas, the constructive criticism when I wandered into your office with my ideas and your assistance in articulating my ideas and concepts in a manner that could be understood by others.

Secondly, I would like to extend my gratitude to my co-supervisor, Matteo Villa, for the stimulating scientific discussions we had during our regular coffee breaks, regardless of whether they were related to the SFETailor project or not. I am thankful for your exemplary dedication to pushing scientific boundaries and his ability to challenge conventional thinking.

A special thank you goes to Frank Niessen for all the support, feedback, and advice when I had the need to talk to someone else than my supervisors. I would especially like to acknowledge your thorough feedback on manuscripts, which has been instrumental in improving their quality.

I am grateful to the Independent Research Fund Denmark for providing the funding for the SFETailor project (Grant No. 9041- 00145B) and giving me the opportunity to pursue my Ph.D. in this fascinating field of research.

I would also like to thank Professor Wolfgang Pantleon for the discussions on dislocation theory and the feedback regarding my ideas.

A heartfelt thank you goes to the technical staff at the Section of Materials and Surface Engineering: Flemming B. Grumsen, Steffen S. Munch, Niklas B. Gammeltoft-Hansen, Peter Westermann, and Lars Pedersen. Their dedicated support and valuable input throughout the project have been immensely valuable.

I want to extend a special thank you to Azdiar Gazder for facilitating my stay at the University of Wollongong and generously sharing his knowledge on EBSD with me. I am also grateful to all the helpful individuals at the Centre for Electron Microscopy at the University of Wollongong.

My sincere gratitude is extended to my colleagues and friends at the Section of Materials and Surface Engineering, including Chiara, Saber, Cecilie, Magnus, Felix, Kleanny, Nikolaj, Bjarke, Basit, Ibrahim, Emilie, and many others. Your presence has created an incredible work environment, and I am thankful for your willingness to lend a helping hand or a supportive ear whenever needed.

Finally, my sincerest gratitude goes to Sandra, my parents, my sister, and my (work) friends in Copenhagen Jakob, Elisabeth, Felix, Kleanny, Nikolaj, Cecilie and Magnus as well as my friends in Malmö Virginia, Jack, Monica, Giuseppe, Hanna, Lukas, Veronika, Giulio, and Dima. Thank you for giving me a place that feels like home, have the feeling that I can be myself and that it is all right that I am the person I am. Thank you for all the dinners, nights out, cabin trips, crab dances, discussions, just being awesome and for being so excited about ice cream (You know who I mean). I could not have done it without you and hope that there are plenty of nice occasions ahead of us.

Abbreviations and Symbols

Note that this section covers only abbreviations and symbols in the main body of the Ph.D. thesis and does not cover the appended papers, where different symbols might have been used.

Abbreviations

- BCC — Body-Centered Cubic
- BCT — Body-Centered Tetragonal
- BF — Bright Field
- CMWP — Convolutional Multiple Whole Profile
- CPA — Coherent Potential Approximation
- DFT — Density Functional Theory
- DIM — Deformation Induced Martensite
- EMTO — Exact Muffin-Tin Orbital
- FCC — Face-Centered-Cubic
- FIB — Focused Ion Beam
- FM — Ferromagnetic
- GB — Grain Boundary
- GP — Guinier-Preston
- GSFE — Generalized Stacking Fault Energy
- HCP — Hexagonal Close-Packed
- HEA — High-Entropy Alloy
- HRTEM — High-Resolution Transmission Electron Microscopy
- MEA — Medium-Entropy Alloy

- ND — Neutron Diffraction
- NM — Nonmagnetic
- OR — Orientation Relationship
- PAW — Projector-Augmented Wave
- SEM — Scanning Electron Microscope
- SF — Stacking Fault
- SFE — Stacking Fault Energy
- SFP — Stacking Fault Probability
- SGTE — Scientific Group Thermodata Europe
- SRO — Short Range Order
- STEM — Scanning Transmission Electron Microscopy
- TEM — Transmission Electron Microscope
- TMT — Transformation Mediated Twinning
- TRIP — Transformation Induced Plasticity
- TWIP — Twinning Induced Plasticity
- UTS — Ultimate Tensile Strength
- VASP — Vienna Ab Initio Simulation Package
- WBDF — Weak Beam Dark Field
- WHR — Work Hardening Rate

Symbols

Latin symbols

- a — Lattice parameter
- a_0 — Strain free lattice parameter

- A Actual cross section
- A_0 Initial cross section
- A_{SF} Area of a stacking fault
- A_Z Zener anisotropy
- A_{hkl}^D Fourier transform of the contribution of size broadening
- A_{hkl}^S Fourier transform of the contribution of strain broadening
- A_{hkl}^{Pl} Fourier transform of the contribution of planar faults
- A^{Phys} Fourier transform of the physical line profile
- $\vec{b}$ Burgers vector
- b Magnitude of $\vec{b}$
- $\vec{b}_p$ Burgers vector of Shockley partial dislocation
- b_p Magnitude of $\vec{b}_p$
- $\vec{b}_L$ Burgers vector of leading Shockley partial
- b_R Broadened reflections
- $\vec{b}_T$ Burgers vector of trailing Shockley partial
- B Parameter depending on single crystalline constants
- c Concentration of solute atoms
- c_i Concentration of i^{th} element
- C Parameter depending on single crystalline constants
- $\bar{C}_{hkl}$ Average dislocation contrast factor
- d_{SF} Distance between two Shockley partial dislocations/width of a stacking fault
- d_0^{hkl} Unstrained interplanar spacing of hkl lattice planes

- $d_{\perp}^{hkl}$ Strained lattice plane spacing of hkl lattice planes perpendicular to the loading direction
- D Grain size
- E Young's modulus
- E_{el} Elastic energy of a dislocation per unit length
- E^{str} Strain energy
- f Wilkens function
- F Applied/uniaxial force
- $\vec{F}_{el}$ Elastic repulsion between two Shockley partial dislocations
- F_{el} Magnitude of $\vec{F}_{el}$
- $\vec{F}_{f}$ Friction force experienced by Shockley partial dislocations
- F_{f} Magnitude of $\vec{F}_{f}$
- F_{fcc} Helmholtz energy of austenite
- F_{hcp} Helmholtz energy of ε –martensite
- $\vec{F}_{L}$ Resulting force on leading Shockley partial dislocation
- F_{L} Magnitude of $\vec{F}_{L}$
- F_{max} Maximum force exerted by a solute atom on a dislocation
- $\vec{F}_{PK,L}$ Peach-Köhler force acting on leading Shockley partial
- $F_{PK,L}$ Magnitude of $\vec{F}_{PK,L}$
- $\vec{F}_{PK,T}$ Peach-Köhler force acting on trailing Shockley partial
- $F_{PK,T}$ Magnitude of $\vec{F}_{PK,T}$
- $\vec{F}_{T}$ Resulting force on trailing Shockley partial dislocation
- F_{T} Magnitude of $\vec{F}_{T}$

- $\vec{g}$ Diffraction vector
- g Magnitude of $\vec{g}$
- ΔG_{ex} Difference in Gibbs energy associated with grain size
- $\Delta G_{chem}^{\gamma \rightarrow \varepsilon}$ Gibbs energy associated with the transformation $\gamma \rightarrow \varepsilon$ related to the chemical compositon
- $\Delta G_{mag}^{\gamma \rightarrow \varepsilon}$ Gibbs energy associated with the transformation $\gamma \rightarrow \varepsilon$ related to the effect of magnetism
- $\Delta G^{\gamma \rightarrow \varepsilon/\alpha'}$ Gibbs energy associated with the transformation $\gamma \rightarrow \varepsilon/\alpha'$
- $\Delta G_{Crit}^{\gamma \rightarrow \varepsilon/\alpha'}$ Critical Gibbs energy associated with the transformation $\gamma \rightarrow \varepsilon/\alpha'$
- h, k, l Miller indices
- ΔH_{mix} Enthalpy of mixing
- I_{hkl} Measure diffraction peak profile
- I_{hkl}^{D} Contribution of size broadening to I_{hkl}
- I_{hkl}^{S} Contribution of strain broadening to I_{hkl}
- I_{hkl}^{Pl} Contribution of planar faults to I_{hkl}
- I_{hkl}^{Instr} Contribution of instrumental broadening to I_{hkl}
- I^{Backgr} Contribution of background to I_{hkl}
- I^{Phys} Physical line profile
- K_{HP} Hall-Petch coefficient
- $K_{111}\omega_0$ Positive proportionality constant of value 6.6
- L Length under applied load
- L_f Fourier length
- L_i Initial length

- L_T Length of twin embryo
- m Schmid factor
- M Taylor factor
- M_s Martensite start temperature
- M_d Temperature above which plastic deformation induces no longer martensite
- n Thickness of martensite plates in numbers of close-packed planes
- N Number of components/elements
- p Pressure
- $\bar{r}$ Average atomic radius
- r_i Atomic radius of ith element
- r_{SF} Radius of curvature of dislocation nodes
- R Ideal gas constant
- R_e Effective outer dislocation cut-off radius
- S_1^{hkl} X-ray elastic constant for a set of lattice planes
- T Temperature
- T_N Neel temperature
- T_0 Equilibrium temperature
- u_R Unbroadened reflections
- U Mechanical driving force
- VEC Valence electron concentration
- V_γ Atomic volume of austenite
- V_ε Atomic volume of ε –martensite

- $\Delta V_{\gamma-\varepsilon}$ Difference in atomic volumes

Greek symbols

- α Factor close to unity
- β Dislocation character angle
- γ_{isf} A material's actual intrinsic SFE
- γ_{isf}^{DFT} A material's SFE determined by DFT
- γ_{isf}^{Exp} A material's SFE determined by experiments
- γ_0 Shear strain
- Γ Dislocation line tension
- δ Atomic size misfit
- δ_L Sign parameter for movement of leading Shockley partial dislocations
- δ_T Sign parameter for movement of trailing Shockley partial dislocations
- ε Engineering strain
- ε_{true} True strain
- ε_0 Normal strain
- $\langle \varepsilon_{111,L_f}^2 \rangle$ Mean square strain
- θ Diffraction angle
- λ Angle between slip direction & loading direction
- μ Shear modulus
- ν Poisson ratio
- $\vec{\xi}$ Dislocation line vector

- ρ Dislocation density
- ρ_A Molar density per unit area of atoms in closed-packed planes
- σ Applied/engineering stress normal stress
- σ_{true} True stress
- σ^{surf} Surface energy of epsilon matrensite
- Σ Stress tensor
- τ Shear stress
- τ_{CRSS} Critical resolved shear stress
- τ_{GB} Contribution to the flow stress from grain boundaries
- τ_{PN} Peierls-Nabarro Stress
- τ_{PR} Contribution to the flow stress from precipitates
- τ_{Twin} Critical resolved shear stress for twinning
- τ_{RSS} Resolved shear stress
- τ_{SS} Contribution to the flow stress from solid solution hardening
- τ_y Flow stress
- τ_{yo}^{F} The zero temperature flow stress according to Fleischer
- τ_{yo}^{L} The zero temperature flow stress according to Labusch
- τ_{WH} Contribution to the flow stress from work hardening
- τ_0 Friction stress
- φ Angle between slip plane normal & loading direction
- χ_i Electronegativity of i^{th} element

- $\Delta\chi$ Electronegativity difference
- ω Parameter describing the interaction of solutes with dislocations

Contents

1 Introduction

1.1 Research framework and hypothesis

The strength-ductility trade-off is a fundamental concept in materials engineering that refers to the inverse relationship between a material's yield strength and its ability to deform without breaking (ductility), i.e. high strength and ductility mutually exclude each other [1–3].

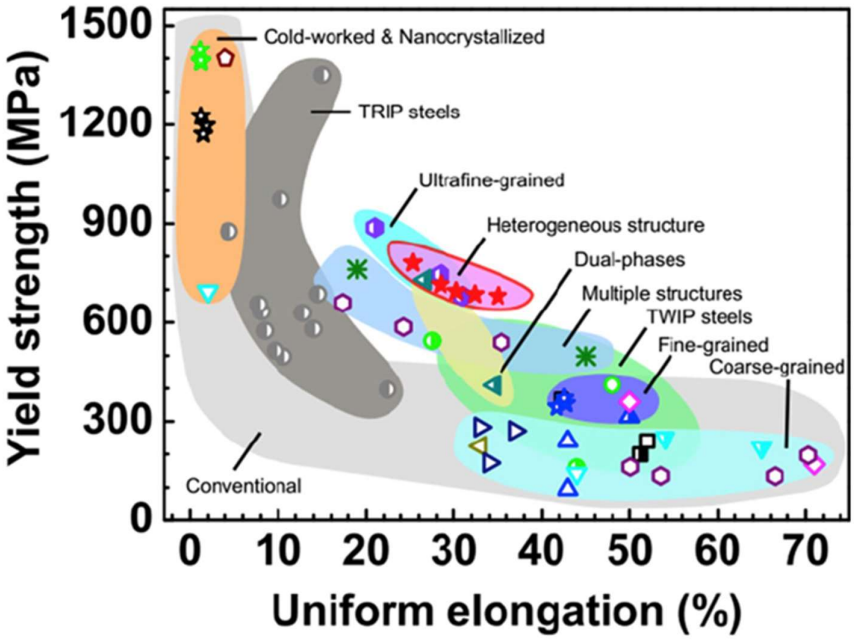

Figure 1.1: Plot of yield strength over uniform elongation showcasing the inverse relationship between these two parameters, i.e. the strength-ductility trade-off. Reproduced with permission from Elsevier from Ref. [4].

The yield strength plays a crucial role in the design of load bearing components, especially when the component's weight and size are important design criteria.

While the yield strength is crucial in minimizing weight and dimensions, materials must additionally exhibit a sufficient degree of ductility to avoid catastrophic failures. As such, structural applications require materials that can withstand high stresses and strains without failure. For example, the automotive industry relies heavily on materials with high strength and ductility to ensure the safety of vehicles in the event of a crash. A further advantage of strong and ductile materials over those that are strong but brittle is the wider applicable range of manufacturing processes, such as cold-forming processes.

Light but safe components are important to reduce greenhouse gas emissions in a variety of sectors. As a result, the last years have seen an increase in research interest regarding understanding and overcoming the strength-ductility trade-off. Since the mechanical properties of materials are determined by the so-called processing-structure-properties relationship, a variety of approaches are investigated with respect to designing materials with improved combinations of strength and ductility [4–15]. Of particular interest is tailoring of the so-called stacking fault energy, which is the energy associated with the presence of a stacking fault that forms in a face-centered cubic matrix and is terminated by a pair of Shockley partial dislocations [7,16–21]. The stacking fault energy governs, whether a material deforms by the movement of perfect dislocations (slip), or deformation twining and martensitic phase transformations [15,21–24]. High stacking fault energy favors slip, while intermediate stacking fault energy values are associated with the prevalence of deformation twinning and alloys with a low stacking fault energy tend to form martensite upon deformation [15,21–24]. Martensite formation and deformation twinning result in significant strain hardening and are commonly referred to as the TRansformation Induced Plasticity (TRIP) and

TWinning Induced Plasticity (TWIP) effect, respectively [7,25]. Materials relying on the TRIP/TWIP effect are currently the best performing [1,5]. Therefore, the stacking fault energy is considered an important factor for tailoring the strength and ductility of face-centered cubic alloys [1,3].

Interstitial elements such as carbon and nitrogen are the most cost-efficient solid solution strengtheners. Furthermore, C and N stabilize austenite and can replace austenite stabilizers such as Ni in austenitic (stainless) steels [26–28]. Hence, designing high-C or high-N alloys that exhibit TWIP and/or TRIP is promising both due to their potential good mechanical properties as well the economic incentives [7,10,13,21,29–31]. In the past, new structural materials were developed through a trial and error method, which is a time-consuming and resource intensive process. Given the vast compositional space of interstitial containing (high-entropy) alloys, it has become even more crucial to use a combination of experimental and computational methods to understand the deformation and strengthening mechanisms of materials, and to accelerate the development of new alloys [2,16]. However, the effect of N and C on the SFE in face-centered cubic alloys is still debated [21,32–43] and it is hence difficult to accurately predict their influence on a material's propensity for TWIP and TRIP.

1.2 Project motivation

The present Ph.D. project is part of the SFETailor project (Grant No. 9041-00145B) funded by the Independent Research Fund. SFETailor comprises an experimental as well as a theoretical part. The original goal of this project was to rethink the development of alloys by using a combination of ab initio and experimental approaches to obtain physical and mechanical data that can be used

to design new alloys intelligently by computational materials engineering methods. As such, the validation of theoretical stacking fault energies obtained by computational materials engineering methods by experiments was of primary interest. After realizing that theoretical and experimental values do currently not coincide, the primary objective of the Ph.D. projected pivoted towards reconciling experimental and theoretical stacking fault energy values to enable validation of computational materials engineering methods

1.3 Outline

This Ph.D. thesis consists of nine distinct chapters. Chapter 1 introduces the research framework and project motivation. Chapter 2 explores the theoretical background of deformation and strengthening mechanisms in face-centered cubic materials. It also discusses the experimental and theoretical methods used to assess the stacking fault energy and explains its impact on the mechanical properties of face-centered cubic materials. The chapter concludes by highlighting the need to revisit the experimental assessment of stacking fault energy in order to reconcile the disparities between experimental and theoretical values. Chapter 4 provides a summary of the main research findings presented in the subsequent results chapters. Chapters 5-7 take the form of manuscripts, providing detailed descriptions and comprehensive discussions of the experimental results. Chapter 8 contains the conclusions of the Ph.D. thesis, while Chapter 9 offers insights into potential future research directions.

2 Theoretical background

This chapter introduces the concept of plastic deformation and strengthening mechanisms in metallic materials. Of particular interest is the relevance of the so-called stacking fault energy on the prevalence of deformation mechanisms and how deformation mechanisms can be altered by tailoring the stacking fault energy. As such, this chapter describes how the stacking fault energy can be assessed experimentally as well as theoretically and how it can be tailored, e.g. by alloying and grain size control.

2.1 High-entropy alloys

High-entropy alloys (HEAs) have attracted considerable research interest in the last decade due to their promising combination of high strength and ductility [44]. Yeh et al. [45,46], who proposed that mixing multiple elements in near-equiatomic concentrations results in a sufficient increase in the configurational entropy of mixing to overcome the tendency to form intermetallics, coined, as a result, the term high-entropy alloy. According to Yeh et al. [45] first definition, HEAs comprise at least five or more elements with concentrations between 5 and 35 wt%. Later on, Yeh et al. [46] extended the previous definition such that HEAs must exhibit a configurational entropy of at least 1.5 times the gas constant R (8.31 J/K·mol). Yeh and coworkers [46,47] continued to stipulate two further effects in addition to the two aforementioned ones, which are of importance to HEAs. Together these four effects are commonly considered as the “four core effects”:

I. The high entropy effect proposes that the high configurational entropy promotes the formation of solid solutions in favor of intermetallic compounds.

II. The lattice distortion effect originates from the high concentration in elements with different atomic radii.

III. The sluggish diffusion effect states that diffusion kinetics in HEAs are intrinsically slower than those in conventional alloys due to locally varying bonding conditions.

IV. The cocktail effect is not a hypothesis regarding physical properties, but describes that the alloy properties may emerge from a “cocktail” of multicomponent alloying with an unexpected, synergistic response in a possibly non-linear manner.

2.1.1 High entropy effect

The high entropy effect is the most essential of the four core effects. It assumes that the increase in configurational entropy in HEAs outweighs the tendency for formation of intermetallic compounds and thus favors formation of solid solutions [45–47]. According to Senkov & Miracle [48], classifying materials according to their entropy is solely qualitative and neglects contributions from vibrational, magnetic and electronic entropies. It was shown that contributions from the vibrational entropy outweigh those of the configurational entropy [48].

Results by Otto et al. [49] confirm the reasoning by Senkov & Miracle [48] that configurational entropy has a limited influence on the phase stability of HEAs. Starting from the CoCrFeMnNi equiatmomic HEA, Otto et al. [49] substituted elements of the HEA with elements of comparable size, electronegativity and same

crystal structure to comply with the Hume-Rothery rules [50] for substitutional solid solutions, e.g. Ni was replaced by Cu. Even though the configurational entropy remained unchanged, the thus created HEAs exhibited a tendency to form multiphase alloys. The results by Otto et al. [49] are in conjunction with work by others [51–53], demonstrating that the influence of configurational entropy on phase stability of HEAs is limited. Indeed, the majority of HEAs tends to decompose into two or multiple phases upon (long-term) annealing [54–59]. Instead of being thermodynamically stabilized, e.g. due to a high configurational entropy, these results indicate that most single phase HEAs are kinetically stabilized [59,60].

2.1.2 Severe lattice distortion

In contrast to dilute solid solutions, HEAs cannot be described by a host matrix in which solute atoms are incorporated [61]. Instead, in HEAs each atom is embedded in a matrix consisting of different solute atoms [62]. The difference in atomic radii (r_i) of the solute atoms results in a displacement from the mean lattice positions [61,63]. In comparison to dilute solid solutions, this displacement is claimed to be larger in HEAs due to an increase in the average atomic size misfit. Several theoretical models have been developed based on the severe lattice distortion effect that accurately predict solid solution strengthening in HEAs [61,63,64]. However, experimental confirmation of an increased lattice distortion in HEAs compared to other materials is challenging [65].

2.1.3 Sluggish diffusion

Yeh [66] proposed that diffusion in HEAs is “sluggish”, i.e. diffusion kinetics are significantly slower than in other materials. According to Yeh [66], the reason for sluggish diffusion is due to the variation in bonding conditions in HEAs experienced by diffusing elements, which is strongly linked to the severe lattice distortion effect. Tsai et al. [67] findings support the reasoning by Yeh [66] and conclude that diffusing elements may be trapped at energetically favorable locations. However, the conclusion by Tsai et al. [67] was recently criticized and the analysis and interpretation were considered faulty [68–70]. In fact, a correlation between number of alloying elements and decreased diffusion kinetics was so far not proven [71,72]. Rather, the diffusivity depends on the combination of alloying elements and the resulting energy barriers for diffusion [71,72].

2.1.4 Cocktail effect

The cocktail effect is not a theory, but a concept proposed by Yeh et al. [45] that the properties of HEAs are the result from a “cocktail” of the multiple components, which may result in synergistic effects augmenting the physical properties in unforeseen ways.

2.1.5 Phase formation rules

In contrast to Yeh et al. [45] hypothesis regarding the importance of configurational entropy, a variety of studies aimed at establishing empirical models to relate phase formation and stability in HEAs with the atomic size misfit (δ), electronegativity, valence electron concentration (VEC), and enthalpy of mixing (ΔH_{mix}) [73–76].

Zhang et al. [73], reasoned that the phase formation in HEAs is dominated by $\Delta H_{mix}$and δ

$$\delta = \sqrt{\sum_{i=1}^{N} c_i \left(1 - \frac{r_i}{\bar{r}}\right)^2}, \tag{2.1}$$

where c_i is the i^{th} element's concentration, N the total number of components, and $\bar{r}$ the average atomic radius ($\bar{r} = \sum_{i=1}^{N} c_i r_i$). Plotting ΔH_{mix} over δ (cf. Figure 2.1), reveals that solid solutions form for $\delta < 6\%$ and $-15 < \Delta H_{mix} < 5$ kJ/mol.

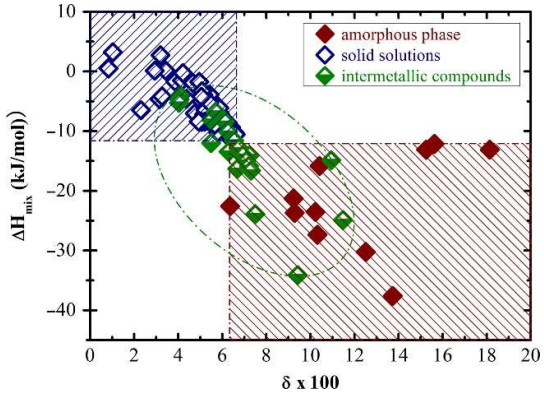

Figure 2.1: Plot of ΔH_{mix} over δ delineating the ranges for solid solution formation according to Ref. [77]. Reproduced with permission from Taylor & Francis Online.

Even though the method by Zhang et al. [73] predicts, whether a HEA will form a solid solution or not, it cannot predict, whether it will form an *fcc* or *bcc* crystal structure. Guo & Liu [74] suggested to further include the electronegativity difference ($\Delta\chi$) and the VEC to predict which phases form

$$\Delta\chi = \sqrt{\sum_{i=1}^{N} c_i \, (\chi_i - \bar{\chi})^2}, \tag{2.2}$$

where $\bar{\chi} = \sum_{i=1}^{N} c_i \chi_i$, and χ_i is the i^{th} element's electronegativity. The VEC is calculated according to Eq. (2.3).

$$VEC = \sum_{i=1}^{N} c_i \, (VEC)_i \tag{2.3}$$

According to the analysis by Guo & Liu [74] *bcc* alloys form for ($VEC \leq 6.87$) and *fcc* alloys ($VEC \geq 8.0$), cf. Figure 2.2.

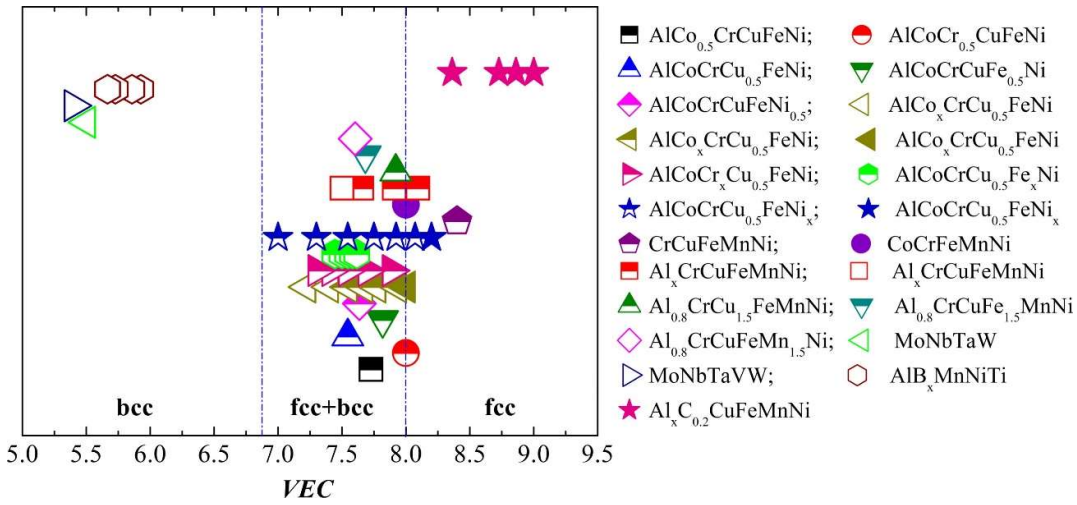

Figure 2.2: Plot of phase stability as a function of VEC according to Ref. [77]. Reproduced with permission from Taylor & Francis Online.

Nevertheless, the VEC –phase formulation rules do not indicate, whether the formed solid solutions are ordered or random [75]. Furthermore, the formation of two *fcc* solid solutions upon exchanging Ni for Cu in the CoCrFeMnNi HEA by Otto et al. [49] cannot be explained and the relation between processing conditions and phase formation is not considered [75].

2.2 Plastic deformation in face-centered cubic materials

Plastic deformation is a material's permanent change in shape as a response to an externally applied force. The most fundamental case of plastic deformation is a

uniaxial force (F) applied to a material with initial cross section (A_0) and initial length (L_i). The applied force results in a stress $\sigma = F/A_0$, the so-called engineering stress. The associated engineering strain (ε) resulting from σ is given by

$$\varepsilon = \frac{L - L_i}{L_i} = \frac{\Delta L}{L_i}, \tag{2.4}$$

where L is the material's length under the applied force. If the applied stress is lower than the material's yield strength (σ_y), the resulting deformation is elastic, i.e. reversible upon unloading, and can be described by Hooke's law, cf. Figure 2.3,

$$\sigma = \varepsilon E, \tag{2.5}$$

where E is the Young's modulus. Upon surpassing σ_y, the resulting deformation is elasto-plastic, i.e. partly non-reversible upon unloading. In case that σ_y is not straightforward to determine, yielding is considered to occur upon surpassing the proof stress, which corresponds to the stress at 0.1 % or 0.2 % of plastic deformation.

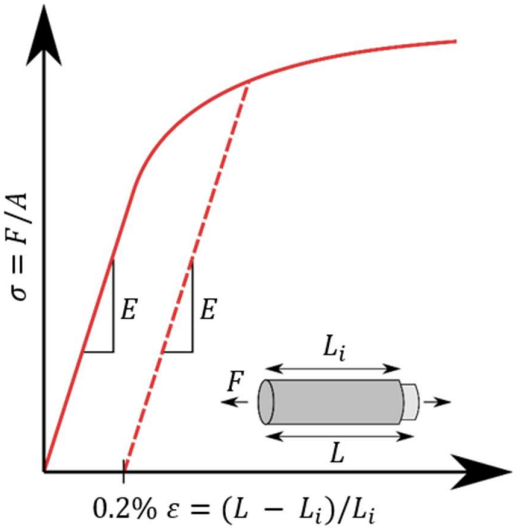

Figure 2.3: Schematic stress-strain curve.

As a result of volume conservation, the actual cross section (A) changes during deformation. Dividing the applied force by A, gives the true stress ($\sigma_{true} = F/A$). True stress and engineering stress (neglecting the change in cross section), as well as true strain (ε_{true}) and engineering strain are related as follows.

$$\sigma_{true} = \sigma\,(1 + \varepsilon) \tag{2.6}$$

$$\varepsilon_{true} = \ln(1 + \varepsilon) \tag{2.7}$$

To accommodate the plastic shape change, atomic planes in a crystalline material need to move relative to each other, without introducing a change in the crystal structure. Instead of moving entire planes with respect to each other, plastic deformation in crystalline materials is accomplished by the movement (glide) of dislocations. Dislocations are one dimensional crystal defects that are defined by their line vector ($\vec{\xi}$) and their Burgers vector ($\vec{b}$). For the part of a dislocation where $\vec{b}$ and $\vec{\xi}$ are parallel, the dislocation has screw character (cf. Figure 2.4), while for the edge character of dislocations $\vec{b}$ and $\vec{\xi}$ are orthogonal to each other. For cases where $\vec{b}$ and $\vec{\xi}$ are neither parallel, nor orthogonal the dislocation has a mixed character.

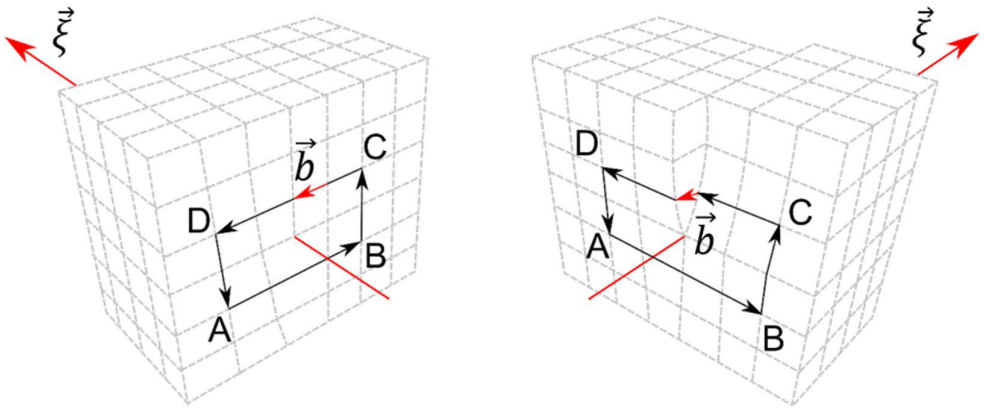

Figure 2.4: Schematic of edge and screw dislocations. Martin Fleck, CC BY-SA 4.0.

The length (magnitude) of the Burgers vector is given by

$$\left|\vec{b}\right| = \frac{a}{2}\sqrt{h^2 + k^2 + l^2}, \tag{2.8}$$

where a is the lattice parameter and h, k, and l are the Miller indices. The stress necessary to move dislocations in metallic materials is orders of magnitude smaller than the theoretical yield strength necessary to shear whole crystallographic planes at once.

2.2.1 Dislocation glide in face-centered cubic materials

Dislocations glide predominantly on close-packed planes along the close-packed direction. For *fcc* crystals, dislocations glide on $\{111\}$ planes in the $\langle 1\bar{1}0\rangle$ direction, i.e. the Burgers vector. Slip plane and Burgers vector constitute a slip system, which there are 12 unique combinations of in *fcc* crystals and if forward and backward glide is considered, *fcc* crystals have 24 slip systems. To classify as a slip system, the Burgers vector must lay within the slip plane, i.e. plane normal ($\vec{n}$) and Burgers vector are orthogonal. The operable slip systems in an *fcc* crystal as well as the possible dislocation reactions are given by the Thompson tetrahedra (cf. Figure 2.5).

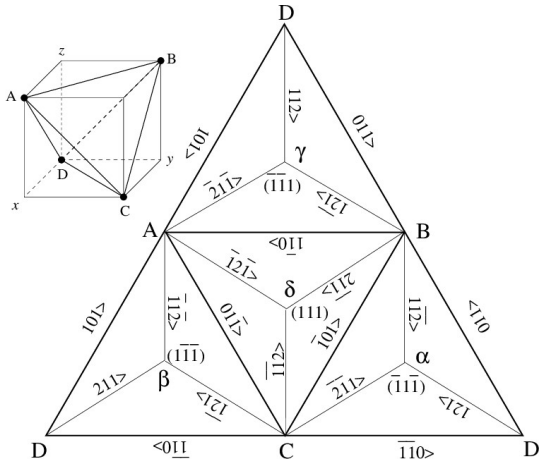

Figure 2.5: Thompson tetrahedra showing possible slip systems and dislocation reactions in face-centered cubic materials. Reproduced with permission from Elsevier from Ref. [78].

For a dislocation to glide, the resolved shear (τ_{RSS}) in the slip plane and along its Burgers vector must be larger than the critical resolved shear stress (τ_{CRSS}). For the case of uniaxial deformation, the relation between τ_{RSS} and the applied load is given by

$$\tau_{RSS} = \frac{F}{A}\cos\varphi\cos\lambda, \tag{2.9}$$

where φ is the angle between slip plane normal and loading direction, while λ is the angle between slip direction and loading direction, cf. Figure 2.6a. The quantity $\cos\varphi\cos\lambda$ is known as the Schmid factor (m). The Schmid factor's orientation dependence for full dislocations in the case of uniaxial tension is given in Figure 2.6b.

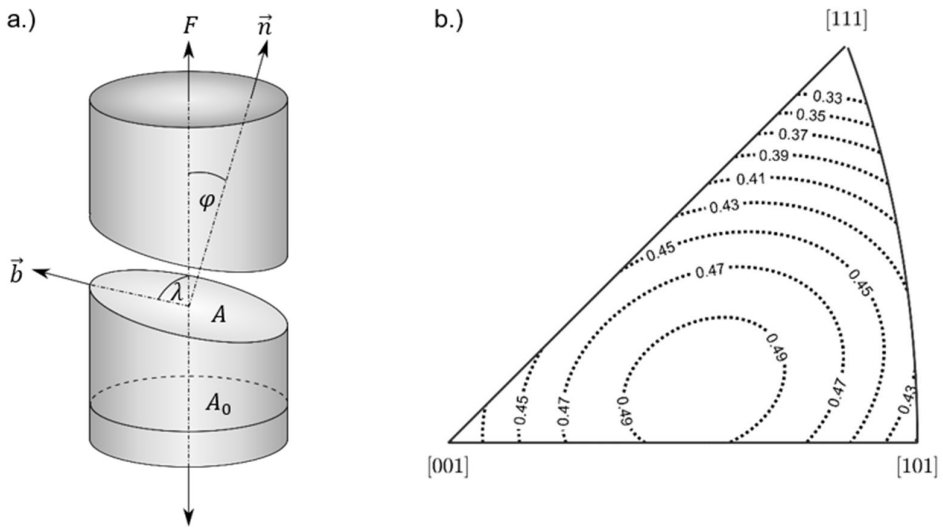

Figure 2.6: a.) Definition of the Schmid factor, b.) Schmid factor for perfect dislocations in case of uniaxial tension.

For polycrystalline materials, τ_{CRSS} and the macroscopic yield strength are related to each other by the Taylor factor (M).

$$\sigma_y = M\tau_{CRSS} \tag{2.10}$$

For a polycrystalline *fcc* material with fully random texture, $M = 3.06$. In uniaxial tension, necking starts when the so-called considère criterion is reached, i.e. the true stress is equal to the work hardening rate (WHR) (WHR $= \frac{d\sigma_{true}}{d\varepsilon_{true}}$). Eventually, when necking starts the material will fail.

2.3 Strengthening mechanisms in metallic materials

As discussed in the previous section, a material's yield strength is the measure of its ability to resist plastic deformation under an applied load, i.e. the resistance against dislocation movement. Strengthening of crystalline alloys is achieved by introducing barriers to dislocation movement, which augment the necessary stress

for dislocations to move. Such barriers can be either foreign atoms, grain or phase boundaries, high dislocation density, or precipitates with small interparticle spacing. A material's flow stress (τ_y) is considered as the sum of the different strengthening contributions as well as the Peierls-Nabarro stress (τ_{PN})

$$\tau_y = \tau_{PN} + +\tau_{SS} + \tau_{WH} + \tau_{GB} + \tau_{PR}, \quad (2.11)$$

where τ_{SS} is the solid solution strengthening, τ_{WH} is the contribution to the flow stress related to the dislocation density, τ_{GB} is the strengthening associated with grain and phase boundaries, and τ_{PR} is the strengthening arising from precipitates.

2.3.1 Solid solution strengthening

Solid solution strengthening is based on the effect of introducing atoms (the alloying element) to the crystal lattice of a base material. The effect of solid solution strengthening is related to the difference in atomic size between alloying and base element, which results in a stress field around the position of the introduced atoms. This stress field interacts with dislocations and eventually increases the necessary stress for dislocations to move through the crystal lattice. Depending on the atomic size of the alloying element, atoms can be either incorporated on lattice positions of the base material where they substitute atoms of the base material, i.e. they form a substitutional solid solution, or occupy interstitial sites in the crystalline lattice, forming an interstitial solid solution. Solubility limits and whether two elements form a substitutional or an interstitial solid solution are governed by the Hume-Rothery rules [50]. The solid solution strengthening associated with the addition of an alloying element scales with its concentration. The two most applied theories describing solid solution strengthening as a function of the concentration

of solute atoms (c) are those developed by Fleischer [79] and Labusch [80], which are both based on the interaction of dislocations with the stress field arising from the solute atoms. The zero temperature flow stress (τ_{yo}^{F}) according to the Fleischer model is given by

$$\tau_{yo}^{F} = \left(\frac{F_{max}}{2\Gamma}\right)^{\frac{3}{2}} \left(\frac{2\Gamma}{b^2}\right) c^{\frac{1}{2}}, \tag{2.12}$$

where Γ is the dislocation line tension, b as the dislocation's Burgers vector, and F_{max} as the maximum force exerted by the solute atom on a dislocation. According to Labusch, the zero temperature flow stress (τ_{yo}^{L}) is

$$\tau_{yo}^{L} = \left(\frac{F_{max}^{4}\omega}{4\Gamma b^7}\right)^{1/3} c^{\frac{2}{3}}, \tag{2.13}$$

where ω is a parameter describing the spatial interaction of solute atoms with dislocations. The Fleischer model [79] considers solute atoms as individual pinning sites/obstacles that each interact with a respective dislocation separately. In contrast, the Labusch model [80] takes into account the combined effect of solute atoms on the glide plane. Consequently, the Labusch model is more suitable for analyzing solid solutions with high concentrations, while the Fleischer model is only relevant for dilute solid solutions (c < 1 at. %). As such, the Fleischer model is commonly use to describe the effect of interstitials on the yield strength, while the Labusch model is used to describe the effect of substitutional elements on the yield strength. However, the Labusch model departs from the assumption that solid solutions comprise one base element, i.e. the solvent, and finite amounts of one or more solutes. Clearly, this is not applicable for highly concentrated solid solutions, such as high-entropy alloys, and eventually breaks down in case of equiatmomic alloys.

Several models were suggested to describe the effect of solid solution strengthening in HEAs [61–63,81]. Varvenne et al. [62] proposed e.g. a solid solution hardening model based on the ideas by Labusch, which is suitable to predict the yield strength of random *fcc* HEAs. The model considers HEAs as a matrix consisting of a single type of atom with average properties. Each element is considered a solute that is incorporated into this matrix, causing local fluctuations in concentration with respect to the overall composition. Following the Labusch model [80], the alloy's strength arises from the interaction of dislocations with the randomly distributed solutes embedded in the average matrix. Dislocations are attracted by solute fluctuations resulting in favorable stress fields and repelled by those resulting in unfavorable ones. This results in bending of the dislocation line, which adopts a wavy low-energy configuration. To glide through the matrix, the dislocation must overcome the energy barrier associated with moving from a favorable to an unfavorable state.

2.3.2 Work hardening

The relation between dislocation density (ρ) and τ_y given in Eq.(2.14) was first proposed by Taylor [82] and describes the increase in flow stress with increasing dislocation density upon deformation

$$\tau_y = \tau_0 + \alpha\mu b\rho^{\frac{1}{2}}, \tag{2.14}$$

where μ is the shear modulus, α is a factor of close to unity, and b is the Burgers vector. The friction stress τ_0 is commonly regarded as the sum of τ_{PN}, τ_{SS}, τ_{GB}, and τ_{PR}.

2.3.3 Grain boundary strengthening

The Hall-Petch relation is used to describe the strengthening arising from grain boundaries in polycrystalline materials and was first proposed independently by Hall [83] and Petch [84] as an empiric model describing the flow stress dependency on grain size

$$\tau_y = \tau_0 + K_{HP} D^{-\frac{1}{2}}, \tag{2.15}$$

where K_{HP} is the Hall-Petch constant and D is the grain size. Both pure metals and alloys comply with the Hall-Petch relation over a large range of grain sizes, i.e. from millimeters down to approx. 1 – 0.01 micron [85–87]. A further reduction in grain size was reported to result in softening instead of strengthening [86,87]. This change is considered to arise from an increase in grain boundary sliding [88] and supposedly altered interactions of grain boundaries with dislocations [89–91].

To rationalize the experimentally observed Hall-Petch effect, different models were suggested, such as pile-up models as well as dislocation density models:

2.3.3.1 Pile-up models

One of the earliest attempts to rationalize the Hall-Petch effect is based on work by Hall [83], which was further extended by Petch [84]. The basic underlying concept is the pile-up model proposed by Eshelby et al. [92]. Herein, it is assumed that grain boundaries constitute a barrier to dislocation motion at which dislocations pile up. The pile-up results in a stress concentration, which eventually triggers dislocation generation and movement in neighboring grains upon surpassing of the critical resolved shear stress.

2.3.3.2 Work hardening

Work hardening models rationalizing the Hall-Petch relation, are mostly based on the work by Ashby [93], which is based on the Taylor equation, cf. Eq. (2.14). Following the reasoning by Ashby [93], the dislocation density is proportional to the inverse of the grain size. Hence, the inverse square root dependence of the Hall-Petch relation follows as a result from the $\rho^{1/2}$ in the Taylor equation.

2.3.3.3 Criticism

Even though the Hall-Petch relation is widely applied and fits reasonably well to the yield strength's grain size dependence for a wide range of pure metals and alloys, it is often criticized for a lack of conclusive experimental validation [94,95]. The spread in experimental data in literature may as well fit to exponents different from -½, such as a simple inverse relationship [94,95]. Li et al. [94] reason that for an inverse relation, K_{HP} becomes a constant for all materials and the sole difference between different materials is their value for τ_0. Furthermore, an inverse relation between yield strength and grain size has a sound physical foundation and agrees with size effects observed in micromechanical testing [94].

2.3.4 Precipitation strengthening

The interaction of precipitates with a dislocation is similar to the one between a solute atom and dislocation. In fact, theories applied to solute solution strengthening were derived from those for precipitation strengthening. Dislocations can bypass precipitates either by shearing through them, bowing out between them (Orowan mechanism), or by cross slip and climb. The latter mechanism is mainly of importance at higher temperatures. The competition between shearing and the

Orowan mechanism is a function of the average precipitate size, which can be explained at the example of $Al_xCoCrFeNi$ HEAs [96–100]. For short aging times, so-called $L1_2$ precipitates (Ni_3Al-type) form with an face-centered cubic crystal structure, similar to Guinier-Preston zones in Cu-Al alloys, which are fully coherent with the HEA matrix [100]. The movement of dislocations at this stage is impeded by the coherency strains necessary to accommodate the difference in atomic size, but eventually dislocations will shear through the $L1_2$ precipitates. Further aging at elevated temperatures, results in growth and eventually to the formation of incoherent body-centered cubic B2 (NiAl-type) precipitates [101]. Due to loss of coherency, dislocations need to bow around B2 precipitates and the associated strengthening is controlled by the Orowan mechanism.

2.4 Stacking faults and stacking fault energy

The elastic energy of a dislocation per unit length (E_{el}) is approximately [102].

$$E_{el} = \alpha \mu b^2 \tag{2.16}$$

According to Frank's rule [102], it is energetically favorable for a dislocation to split up into two partial dislocations, a leading and a trailing one, if

$$\vec{b}^2 > \vec{b}_L^2 + \vec{b}_T^2, \tag{2.17}$$

where $\vec{b}_L$ and $\vec{b}_T$ are the Burgers vector of the leading and trailing partial dislocation, respectively. For *fcc* crystals, Frank's rule is fulfilled if a perfect dislocation ($\vec{b} = \frac{a}{2}\langle 110 \rangle$) splits up into two Shockley partial dislocations.

$$\frac{a}{2}[110] = \frac{a}{6}[21\bar{1}] + \frac{a}{6}[121] \tag{2.18}$$

As for perfect dislocations, there are 12 unique Shockley partial slip systems in *fcc* crystals (24 when considering forward and backward glide), cf. Thompson's tetrahedron in Figure 2.5. The stacking sequence of close-packed $\{111\}$ planes in *fcc* is $ABCABCAB$ … (cf. Figure 2.7a). The Burgers vector of perfect dislocations is a translational vector. Hence, glide of perfect dislocations does not affect the stacking sequence in *fcc* crystals. In contrast, the Burgers vector of Shockley partial dislocations is not a translational vector. As a result, the area between two Shockley partial dislocations exhibits a change in stacking sequence, i.e. a so-called intrinsic stacking fault (SF) (cf. Figure 2.7b).

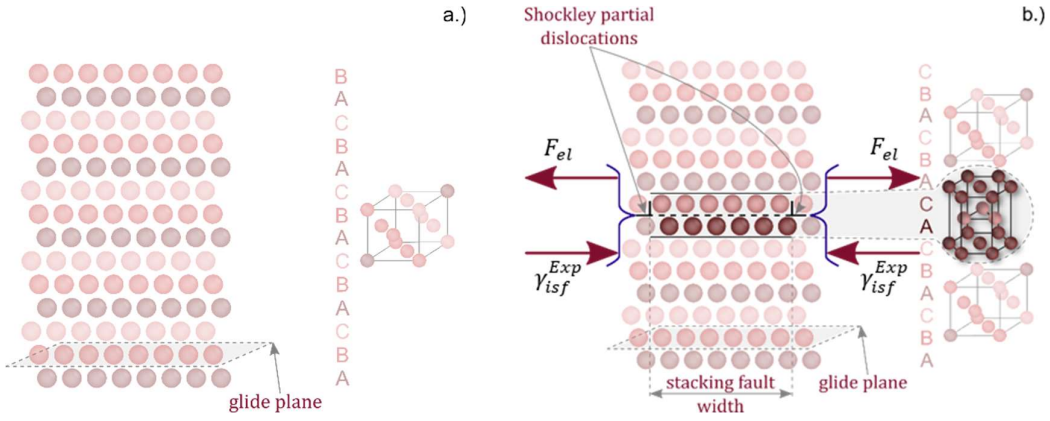

Figure 2.7: a.) Stacking sequence of close-packed planes in face-centered cubic lattice, b.) Force balance over an intrinsic stacking fault.

The two Shockley partial dislocations interact elastically with each other. According to Aerts et al. [103], the resulting Force (F_{el}) is given by

$$F_{el} = \frac{\mu b_p^2}{4\pi d_{SF}} \left(\frac{2-\nu}{1-\nu}\right) \left(1 - \frac{2\nu \cos(2\beta)}{2-\nu}\right), \tag{2.19}$$

where, ν is the Poisson ratio, β is the angle between the Shockley partial dislocations' Burgers vector and the dislocation line vector, and d_{SF} the distance between the partials, i.e. the stacking fault width. The formation of a SF is

associated with an energy, i.e. the stacking fault energy (SFE). The current opinion is that the SFE is an intrinsic materials parameter, even though early research on SFs and SFE in *fcc* materials indicates that experimental SFE values are influenced by a material's microstructure and should be regarded as apparent values [104,105]. Nevertheless, these findings never received much recognition for their scientific significance in challenging the opinion that the experimental SFE is an intrinsic materials parameter. In the following, it is therefore differentiated between the experimental SFE (γ_{isf}^{Exp}), a material's actual intrinsic SFE (γ_{isf}), and theoretical determined SFE values (γ_{isf}^{DFT}).

Due to F_{el}, SFs widen until the energy gain arising from the expansion is equal in magnitude to the SFE, cf. Figure 2.7b. Hence, it applies

$$\gamma_{isf}^{Exp} = F_{el} \tag{2.20}$$

$$\gamma_{isf}^{Exp} = \frac{\mu b_p^2}{4\pi d_{SF}} \left(\frac{2-\nu}{1-\nu}\right) \left(1 - \frac{2\nu \cos(2\beta)}{2-\nu}\right) \tag{2.21}$$

Notably, this force balance departs from the assumption that the Shockley partial dislocations can glide freely on their glide plane and any resistance against dislocation movement is neglected. Furthermore, Eq. (2.21) implies that γ_{isf}^{Exp} can attain exclusively positive values.

2.4.1 Correlation of SFE and deformation mechanisms in face-centered cubic materials

The experimental SFE and the activation of deformation mechanisms are considered closely related in *fcc* materials. In general, high SFE materials (e.g.

nickel, gold, aluminum, and copper) tend to deform by dislocation slip. In these materials, the SFE creates a higher energy barrier for the dissociation of dislocations and formation of wide stacking faults [102]. The narrow width of SFs in these materials decreases the necessary energy to form constrictions and therefore increases the likelihood for cross-slip and in conjunction dislocation annihilation during plastic deformation [18,102]. As a result, materials with a higher SFE tend to exhibit lower work hardening rates than low-SFE materials [18,106–108]. With decreasing SFE, the formation of wide SFs becomes energetically more favorable, leading to an increased density of stacking faults [109–114], i.e. the stacking fault probability (SFP). With increasing SFP, the likelihood for SFs to overlap and potentially form on consecutive {111} planes increases [109,114], which leads to deformation twinning (cf. Section 2.4.2). A further decrease in SFE changes the prevalent deformation mechanism from twinning to deformation-induced martensite [21,36,115,116]. Both, twinning as well as deformation induced martensite result in increased work hardening rates and therefore promote a high ductility. The reason for the increase in WHR is considered to be related to the continuous refinement of a material's microstructure due to twin and martensite formation. Twin boundaries and martensite/austenite phase boundaries constitute obstacles for dislocation movement and a continuous refinement leads to an increase in the flow stress, i.e. the dynamic Hall-Petch effect [117–120]. Thus, SFE-tailoring is considered a viable option to optimize mechanical properties in *fcc* materials [1,15,16,121,122]. For *fcc* steels, several empirical relations were suggested to link a material's SFE to the prevalence of dislocation slip, twinning, and martensite formation [21,22,24], cf. Figure 2.8.

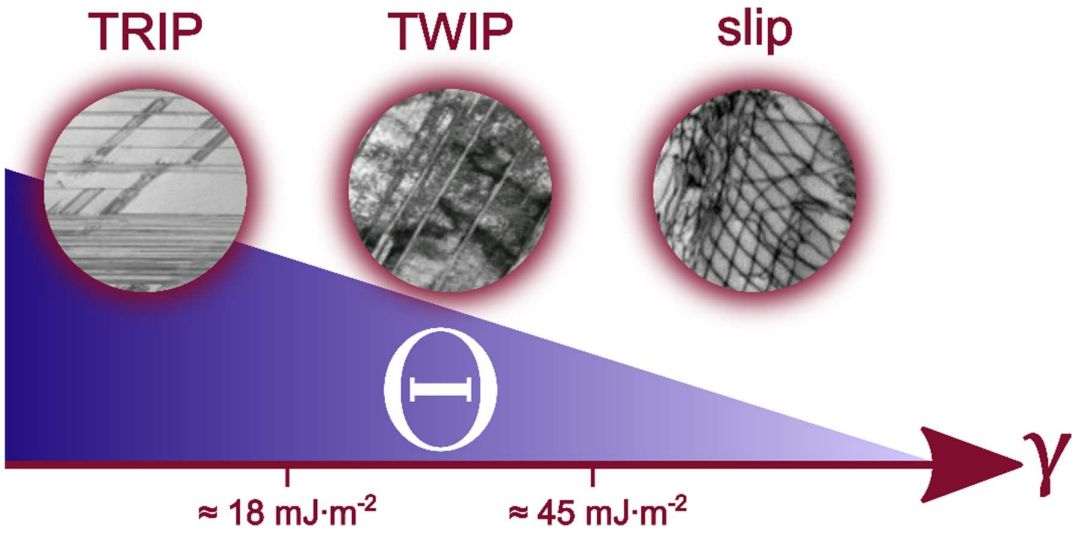

Figure 2.8: Correlation between the prevalence of stacking fault energy and the prevalence of martensite formation (TRIP), deformation twinning (TWIP), and dislocation glide [21,22,24]. Further, the correlation between TRIP, TWIP, slip and the work hardening rate is given. Microstructural representations were reproduced from Ref. [21] with permission from Elsevier.

Even though based on data for steels, the suggested correlations of active deformation mechanisms and SFE are often applied to describe the occurrence of twinning and martensite formation in HEAs .

2.4.2 Deformation twinning

Fontaine [123] suggested that deformation twins form from overlapping stacking faults and grow by subsequent passage of Shockley partial dislocations on adjacent {111} planes. The stacking sequence of the fcc lattice remains unchanged, but with a mirrored sequence when comparing regions above and below the twin boundary (cf. Figure 2.9).

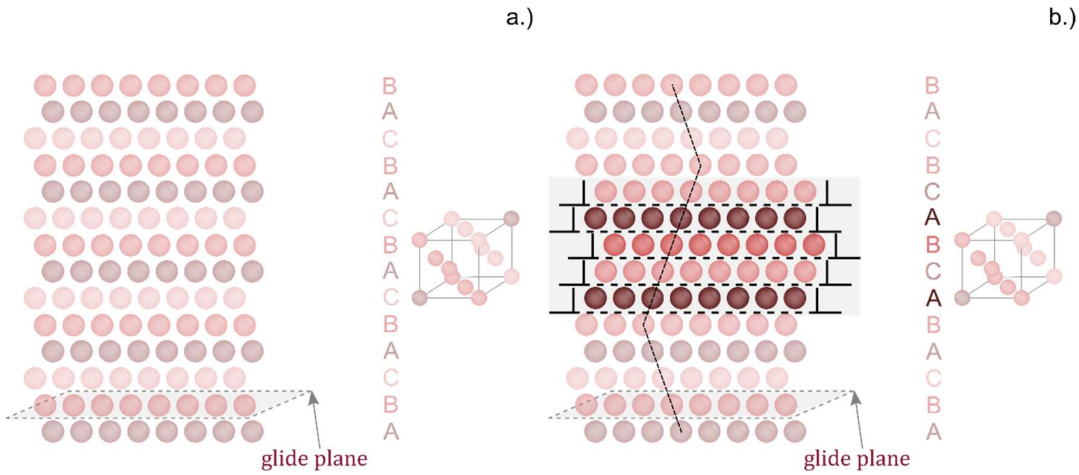

Figure 2.9: a.) Stacking sequence of close-packed planes in face-centered cubic lattice, b.) stacking sequence of close-packed planes in face-centered cubic lattice including a twin.

Based on the work by Fontaine [123], several models have been proposed to explain the necessary dislocation reactions for twin formation, such as the Venables pole mechanism [124], the Cohen-Weertman Frank cross-slip mechanism [125], the Mahajan-Chin extrinsic fault mechanism [126], and the Copley-Kear-Byun partial dislocation breakaway mechanism [127,128].

Despite assuming different dislocation reactions, the models have in common that twinning is first initiated after a certain amount of plastic deformation and upon surpassing the critical resolved shear stress for twinning [129]. Based on the empiric relation between the SFE and the occurrence of twinning (cf. Figure 2.8), several groups tried to link twinning stress and SFE with each other.

- Narita & Takamura [130] $$\tau_{twin} = \frac{\gamma_{isf}^{Exp}}{2b_p} \quad (2.22)$$

- Byun [128] $$\tau_{twin} = \frac{2\gamma_{isf}^{Exp}}{b_p} \quad (2.23)$$

- Suzuki & Barett [131] $$\tau_{twin} \frac{\gamma_{isf}^{Exp}}{2b_p} + \frac{\mu b_p}{L_T} \quad (2.24)$$

- Mahato et al. [132] $$\tau_{twin} = \frac{\gamma_{isf}^{Exp}}{b_p} + \frac{\mu b_p}{L_T} \quad (2.25)$$

- Meyers et al. [133] $$\tau_{twin} = \frac{\gamma_{isf}^{Exp}}{b_p} + \frac{K_{HP}}{\sqrt{D}} \quad (2.26)$$

- Urrutia et al. [134] $$\tau_{twin} = \frac{\gamma_{isf}^{Exp}}{b_p} + \frac{\mu b_p}{D} \quad (2.27)$$

- Steinmetz et al. [135] $$\tau_{twin} = \frac{\gamma_{isf}^{Exp}}{3b_p} + \frac{3\mu b_p}{L_T} \quad (2.28)$$

Where L_T is the length of a twin embryo. It is noted that the equations above are commonly validated only for a single alloy system and have limited predictability for other alloying systems. Furthermore, the fact that that $\tau_{twin} \propto \gamma_{isf}^{Exp}$ leads to erroneous predictions of the trend for τ_{twin} in HEAs [136].

2.4.3 Martensitic transformation

The martensitic transformation is a diffusionless phase transformation in the solid state, where the parent phase (austenite) is transformed by a sequence of shear and volume expansions into the martensitic child phase. Martensitic

transformations are considered to be athermal, i.e. the transformation will not progress at constant temperature and the amount of martensite formed depends directly on the temperature [137]. Although, recent research by Villa & Somers [138,139] challenged this assumption and demonstrated that thermally activated martensite formation is the rule rather than the exception.

Athermal martensite starts to form spontaneously once the driving force ($\Delta G^{\gamma\rightarrow\varepsilon/\alpha'} = \Delta G_{chem}^{\gamma\rightarrow\varepsilon/\alpha'} + \Delta G_{mag}^{\gamma\rightarrow\varepsilon/\alpha'}$) is equal to the critical driving force ($\Delta G_{Crit}^{\gamma\rightarrow\varepsilon/\alpha'}$), which is satisfied at the martensite start temperature (M_s) [140], cf. Figure 2.10. M_s is lower than the equilibrium temperature (T_0), for which $\Delta G^{\gamma\rightarrow\varepsilon/\alpha'} = 0$.

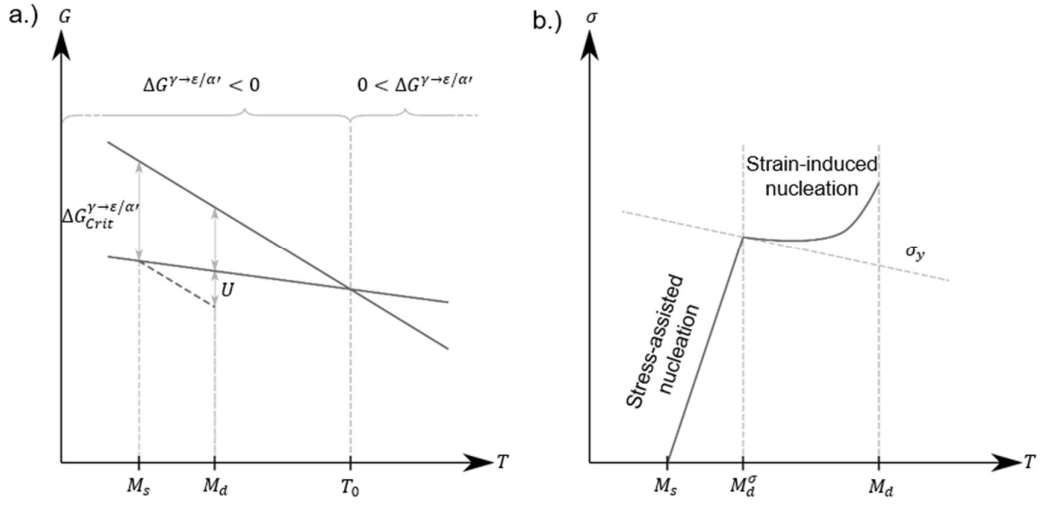

Figure 2.10: a.) Gibbs energy curves of austenite and ε/α' –martensite as a function of temperature delineating stable and metastable regions of austenite, b.) Effect of applied stress on stress-assited and strain-induced martensite formation as a function of temperature according to [140].

For temperatures $M_s < T < T_0$, $\Delta G^{\gamma\rightarrow\varepsilon/\alpha'}$ is not sufficient to initiate martensite formation. Although, according to Patel & Cohen [141] an applied stress provides additional mechanical driving force (U)

$$U = \tau\gamma_0 + \sigma\varepsilon_0, \tag{2.29}$$

where γ_0 and ε_0 are the shear and normal strain, respectively. While, τ and σ are the respective shear and normal stress.The additional mechanical driving force can be sufficient to trigger martensite formation above M_s [140] up to a certain temperature (M_d) above a further temperature increase U is no longer sufficient to form martensite. If the applied stress is below the materials yield strength, Olson & Cohen [140] consider the formed martensite as stress-assisted (cf. Figure 2.10b), whereas applied stresses higher than the yield strength result in strain-induced martensite formation.

For *fcc* steels and HEAs, austenite transforms either into hexagonal-close packed (*hcp*) ε −martensite or *bcc*/body-centered tetragonal (*bct*) α' −martensite [137]. Due to the coordinated movement of atoms, lattice planes and directions in austenite and the respectively formed martensite, exhibit a so-called orientation relationship (OR), i.e. certain crystallographic planes and directions in austenite and martensite are parallel [137].

2.4.3.1 The transformation γ − austenite → ε − martensite

As discussed in Section 2.4, an intrinsic SF constitutes a two-layer high ε − martensite embryo. If, in contrast to deformation twinning, further SFs form on every other $\{111\}$ plane and not on consecutive $\{111\}$ planes the ε − martensite plate thickens. Lateral growth is accomplished by widening of the SFs, and/or coalescence of SFs that have formed on the same close-packed plane. For the transformation $\gamma \rightarrow \varepsilon$ − martensite, the commonly observed OR in *fcc* steels and HEAs complies with the Shoji-Nishiyama OR [137]:

$\{111\}_\gamma \| \{001\}_\varepsilon$ & $\langle 011\rangle_\gamma \| \langle 11\bar{2}\rangle_\varepsilon$ Shoji-Nishiyama

2.4.3.2 α' – martensite

α' – martensite can form either directly from austenite ($\gamma \rightarrow \alpha'$), or via intermediary ε – martensite ($\gamma \rightarrow \varepsilon \rightarrow \alpha'$), that is consumed by ongoing formation of α' – martensite. Reported nucleation sites for α' – martensite formation range from intersections of shear bands and ε – martensite plates with each other, to intersections of shear band with twin and grain boundaries [23,85,142,143]. Although, the delineation between, shear band, single SFs, and ε – martensite is often ambiguous as pointed out by Talonen et al. [144]. The first description of the crystallographic mechanism behind the direct transformation from austenite to α' – martensite was suggested by Bogers & Burgers [145]. As shown in Figure 2.11, α' – martensite forms at the intersection of two shear operations ($\frac{T_\gamma}{2}$) and ($\frac{T_\gamma}{3}$). It was later shown by Olson & Cohen [140] that the shear operations suggested by Bogers & Burgers correspond to a single SF averaged over two $\{111\}$ planes ($\frac{T_\gamma}{2}$) and a SF averaged over three $\{111\}$ planes ($\frac{T_\gamma}{3}$). Notably, $\frac{T_\gamma}{2}$ corresponds to the formation of ε – martensite. The model suggested by Schumann [146] to rationalize the formation of α' – martensite at the intersection of two ε – martensite plates is similar to the Borgers & Burgers model [145].

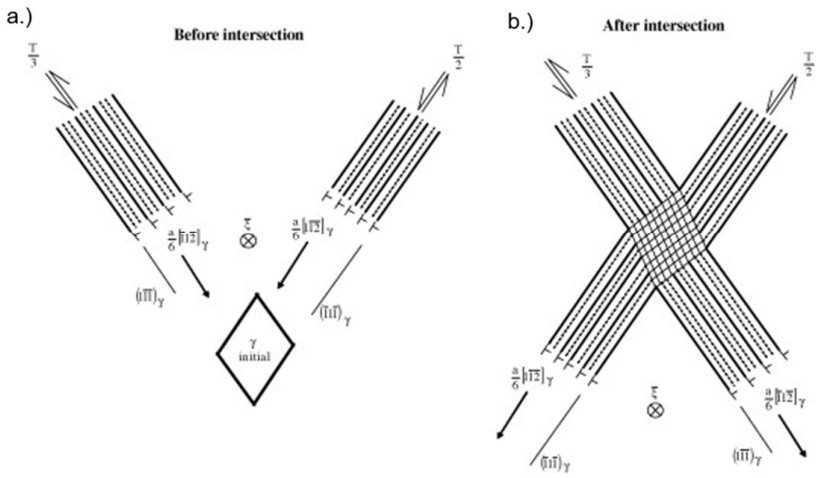

Figure 2.11: Shear operations to form α' – martensite from austenite according to Bogers & Burgers [145], a.) before intersecting, and b.) after intersecting. Reproduced with permission of Elsevier from Ref. [147].

Irrespective of α' – martensite formation directly from austenite or via intermediary ε – martensite, it exhibits most commonly either the Kurdjumov-Sachs [148], or the Nishiyama-Wassermann OR [149] with respect to austenite:

$$\{111\}_\gamma \| \{011\}_{\alpha'} \;\&\; \langle 011\rangle_\gamma \| \langle 111\rangle_{\alpha'} \quad \text{Kurdjumov-Sachs}$$

$$\{111\}_\gamma \| \{011\}_{\alpha'} \;\&\; \langle 112\rangle_\gamma \| \langle 110\rangle_{\alpha'} \quad \text{Nishiyama-Wassermann}$$

2.4.4 Experimental assessment of the stacking fault energy

Irrespective of the applied technique, measuring the SFE departs from Eq. (2.19), i.e. the only components considered in the force balance over a SF are the SFE itself and the elastic interaction between the two Shockley partial dislocations. Since both μ and b_p can be measured and/or calculated, the two only unknown variables in Eq. (2.19) are γ_{isf}^{Exp} and d_{SF}. Hence, by determining d_{SF} the SFE can be calculated based on Eq. (2.19).

2.4.4.1 Transmission electron microscopy

Transmission electron microscopy (TEM) enables the measurement of d_{SF}. Hence, assessing γ_{isf}^{Exp} by TEM is considered a direct method. Apart from determining d_{SF}, γ_{isf}^{Exp} can be further calculated from the radius of extended dislocation nodes (r_{SF}), as suggested by Whelan [150]. However as discussed by Gallagher [151], the determination of r_{SF} is difficult and to a certain degree subjective. Cockayne et al. [152,153] suggested instead to measure d_{SF} by weak beam dark field imaging (WBDF). WBDF has the advantage that the positions of partial dislocations can be determined more accurately as e.g. by regular bright field imaging [153]. Measuring d_{SF} and plotting it against β, enables to fit the experimental SF-widths with Eq. (2.19) and determine γ_{isf}^{Exp} accordingly, as shown exemplary in Figure 2.12 by Laplanche et al. [154].

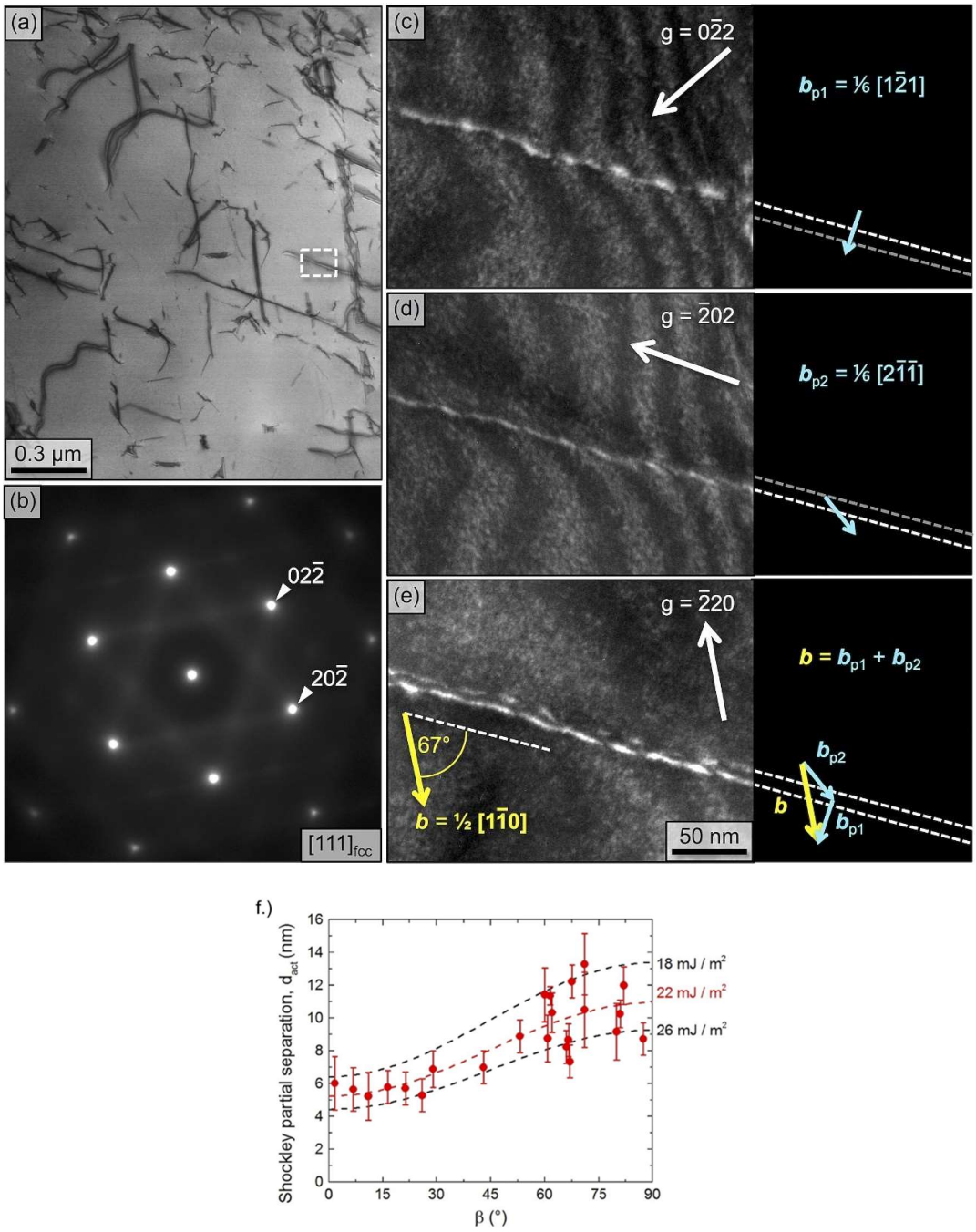

Figure 2.12: Analysis of dislocation occurrence following compression at 293 K up to a true strain of 4% was conducted. (a) An image captured using STEM and utilizing the diffraction condition depicted in (b) reveals the presence of elongated dislocations located within the (111) plane, exhibiting a near-parallel alignment with the TEM foil. (b) The diffraction pattern illustrates that the [111] zone-axis aligns closely with the incident beam. (c) Micrographs of weak beam g(3g) were obtained from the specific region marked by a white dashed rectangle in (a). f.) The spacing between Shockley partial dislocations was examined as a function of the angle formed between the dislocation line and the Burgers vector of the full dislocation. Reproduced from Ref. [154] with permission from Elsevier.

In contrast to bright field imaging, WBDF has the advantage to determine the position of Shockley partials more accurately, thus enabling the measurement of narrow SFs (< 80 Å) [155]. However as discussed by Cockayne & Vitek [155], for narrow SFs the core structure of the Shockley partial dislocations is no longer negligible. Hence, measurements of γ_{isf}^{Exp} for high SFE materials, i.e. materials exhibiting narrow SFs, should be assessed with care [155,156].

2.4.4.2 X-ray and neutron diffraction

On the other hand, X-ray (XRD) and neutron diffraction (ND) cannot measure d_{SF} or r_{SF}. Instead, Reed & Schramm [157] suggested a method that enables to determine γ_{isf}^{Exp} based on peak broadening and peak shifts induced by dislocations and SFs. However, this approach relies on calibration with SFE values determined by TEM (cf. Paragraph 2.4.4.1) and is hence considered an indirect method.

The determination of the SFE via XRD and ND is based on the shift and broadening of the Bragg peak induced by dislocations and the formation of stacking faults. The method suggested by Reed & Schramm [157] is inspired by Otte [158] and Adler & Otte [159]. It adopts the relation between stacking fault probability (SFP), dislocation density (ρ) and the experimental SFE (γ_{isf}^{Exp}) as proposed by Smallmann & Westmacott [160]

$$\gamma_{isf}^{Exp} = \frac{K_{111}\omega_0\mu_{111}a_0}{\sqrt{3}\pi} {A_Z}^{-0.37} \frac{\langle\varepsilon_{111,L_f}^2\rangle}{SFP}, \tag{2.30}$$

where a_0 is the strain free lattice parameter, $\langle\varepsilon_{111,L_f}^2\rangle$ is the mean-square strain, $K_{111}\omega_0$ is a *positive* proportionality constant with value 6.6, A_Z is the Zener anisotropy ($A_Z = 2c_{44}/(c_{11} - c_{12})$), and L_f is the Fourier length. To calculate γ_{isf}^{Exp}

according to Eq. (2.30) from XRD or ND diffraction patterns, both SFP as well as $\langle \varepsilon^2_{111,L_f} \rangle$ have to be determined from peak shift and broadening, respectively.

According to Warren [161], the presence of SFs results in a peak shift. The magnitude of the peak shift is proportional to the amount of SFs in the probed material volume and therefore also proportional to SFP. Following Warren [161]

$$\Delta(2\theta) = \frac{90\sqrt{3}SFP \tan\theta}{\pi^2} \frac{\sum_b(\pm)L_0}{h_0^2(u_R+b_R)}, \tag{2.31}$$

where θ is the diffraction angle, $h_0^2 = h^2 + k^2 + l^2$, while u and b are the unbroadened and broadened reflections. Further, $L_0 = 3N + 1$ for reflections affected by broadening and $L_0 = 3N$ for reflections not affected by broadening. The values for $\frac{\sum_b(\pm)L_0}{h_0^2(u_R+b_R)}$ for the *fcc* crystal structure are given in Table 2.1.

Table 2.1: Values for $\frac{\sum_b(\pm)L_0}{h_0^2(u_R+b_R)}$ describing the peak shift of lattice planes due to the presence of stacking faults according to Warren [161].

	$\frac{\sum_b(\pm)L_0}{h_0^2(u_R+b_R)}$				
hkl	111	200	220	311	222
	+1/4	-1/2	+1/4	-1/11	-1/8

In addition to the peak shift associated with the presence of SFs, peak positions are affected by long range residual/applied stresses. Hence, if γ_{isf}^{Exp} is determined from in-situ XRD or ND experiments, the effective peak shift has to be considered as a superposition of the effects of SFs and elastic strains. For a given set of lattice planes with their plane normal ($\vec{n}$) perpendicular to the loading direction, it follows:

$$\varepsilon_{\perp}^{hkl} = \frac{d_{\perp}^{hkl} - d_0^{hkl}}{d_0^{hkl}} = S_1^{hkl}\sigma - \frac{\sqrt{3}}{4\pi} SFP \frac{\sum_b(\pm)L_0}{h_0^2(u_R + b_R)}, \tag{2.32}$$

where S_1^{hkl} is the X-ray diffraction elastic constant for a set of lattice planes. It is common practice to determine the SFP not from absolute peak positions, but from relative differences in peak positions of two sets of lattice planes, i.e. $\{111\}$ and $\{222\}$. This reduces the effects of uncertainties in the determination of absolute peak positions. Since $S_1^{111} = S_1^{222}$, it follows

$$\varepsilon_{\perp}^{222} - \varepsilon_{\perp}^{111} = \left(S_1^{222}\sigma - \frac{\sqrt{3}}{4\pi} SFP \frac{\sum_b(\pm)L_0}{h_0^2(u_R + b_R)}\right) - \left(S_1^{111}\sigma - \frac{\sqrt{3}}{4\pi} SFP \frac{\sum_b(\pm)L_0}{h_0^2(u_R + b_R)}\right), \tag{2.33}$$

with $S_1^{111} = S_1^{222}$, it follows

$$\varepsilon_{\perp}^{222} - \varepsilon_{\perp}^{111} = \left(-\frac{\sqrt{3}}{4\pi} SFP \frac{\sum_b(\pm)L_0}{h_0^2(u_R + b_R)}\right) - \left(-\frac{\sqrt{3}}{4\pi} SFP \frac{\sum_b(\pm)L_0}{h_0^2(u_R + b_R)}\right). \tag{2.34}$$

With the tabulated values from Table 2.1, the differences in lattice strains for the $\{111\}$ and $\{222\}$ sets of lattice planes are relate to SFP as follows

$$\varepsilon_{\perp}^{222} - \varepsilon_{\perp}^{111} = \frac{3\sqrt{3}}{32\pi} SFP. \tag{2.35}$$

Diffraction peak profiles (I_{hkl}) are the sum of the convolution of size (I_{hkl}^{D}), strain (I_{hkl}^{S}), planar fault (I_{hkl}^{Pl}), instrumental (I_{hkl}^{Instr}) broadening and the background (I^{Backgr})

$$I_{hkl} = I_{hkl}^{D} * I_{hkl}^{S} * I_{hkl}^{Pl} * I_{hkl}^{Instr} + I^{Backgr}. \tag{2.36}$$

To determine $\langle \varepsilon_{111,L_f}^2 \rangle$, I_{hkl} has to be deconvoluted into the respective contributions. Several methods have been suggested for this purpose, such as the (modified) Williamson-Hall method [162,163], (modified) Warren-Averbach method

[163,164], and approaches based on whole profile fitting, such as Convolutional Multiple Whole Profile (CMWP) fitting [165]. The different approaches have in common that before determining the contributions of I_{hkl}^{D}, I_{hkl}^{S}, and I_{hkl}^{Pl}, the instrumental broadening has to be accounted for, such that only the physical line profile is considered during further analysis ($I^{Phys} = I_{hkl}^{D} * I_{hk}^{S} * I_{hkl}^{Pl}$). The Fourier transform of I^{Phys} is

$$A^{Phys} = A_{hkl}^{D} A_{hkl}^{S} A_{hkl}^{Pl}, \tag{2.37}$$

where A_{hkl}^{S} is

$$A_{hkl}^{S} = e^{-2\pi^2 g^2 {L_f}^2 \langle \varepsilon_{g,L_f}^2 \rangle}. \tag{2.38}$$

The mean square strain can be calculated according to Wilkens [166] as

$$\langle \varepsilon_{g,L_f}^2 \rangle = \frac{\rho \bar{C}_{hkl} b^2}{4\pi} f\left(\frac{L_f}{R_e}\right), \tag{2.39}$$

where f is the Wilkens function, R_e is the effective outer dislocation cut-off radius, $\bar{C}_{hkl}$ is the average dislocation contrast factor [167], which is calculated as

$$\bar{C}_{hkl} = \bar{C}_{h00}(1 - qH^2), \tag{2.40}$$

where $H = \frac{h^2k^2 + h^2l^2 + {}^2k^2l^2}{(h^2 + k^2 + l^2)^2}$, $\bar{C}_{h0} = B$, and $q = -C/B$. Both B and C are a function of the single crystalline constants and the dislocation character [167]. For the determination of $\langle \varepsilon_{g,L_f}^2 \rangle$ by the (modified) Williamson-Hall method and the (modified) Warren-Averbach method the reader is referred to Refs. [162–164,168].

2.4.5 Theoretical Assessment

As shown in Figure 2.7b, a single intrinsic stacking fault changes the stacking sequence locally from (*ABCABCABCAB…*) to (*ABABABABABA…*), which corresponds to a two layer high ε −martensite embryo. Based on this insight, Olson & Cohen [140] suggested that the SFE is linked to the chemical Gibbs energy for ε −martensite formation ($\Delta G_{chem}^{\gamma\to\varepsilon}$), the strain energy ($E^{str}$), and a surface energy ($\sigma^{surf}(n)$)

$$\gamma_{isf} = n\rho_A\left((\Delta G_{chem}^{\gamma\to\varepsilon} + E^{str}\right) + 2\sigma^{surf}(n), \tag{2.41}$$

where n is the thickness in plates of the ε −martensite embryo, for an intrinsic SF $n = 2$, and ρ_A is the molar density per unit area of atoms in the close-packed $\{111\}$ planes. According to Olson & Cohen [140], E^{str} is negligible due to the interface being coherent, which is in agreement with conclusions from Li et al. [169]. Since σ^{surf} cannot be measured, Olson & Cohen [140] suggest to determine it by subtracting $\rho_A\left((\Delta G_{chem}^{\gamma\to\varepsilon} + E^{str}\right)$ from γ_{isf}^{Exp}. Accordingly determined values for σ^{surf} vary significantly, as shown e.g. by Pierce et al. [170] for the Fe-Mn(-Si-Al-C) system.

2.4.5.1 Thermodynamic modelling of Gibbs energy

While Olson & Cohen [140] considered solely $\Delta G_{chem}^{\gamma\to\varepsilon}$ to contribute to γ_{isf}, it was later shown that the contribution of magnetism ($\Delta G_{mag}^{\gamma\to\varepsilon}$) has to be taken into account [171,172]. Hence, Eq. (2.41) becomes

$$\gamma_{isf} = n\rho_A\left((\Delta G_{chem}^{\gamma\to\varepsilon} + \Delta G_{mag}^{\gamma\to\varepsilon} + E^{str}\right) + 2\sigma^{surf}(n). \tag{2.42}$$

The term $\Delta G_{mag}^{\gamma\to\varepsilon}$ arises from antiferromagnetic ordering, which occurs for temperatures below the Néel temperature (T_N) [170,172]. Antiferromagnetism affects the Gibbs energy of austenite and ε –martensite to different extents and thus influences γ_{isf} [170,172]. Furthermore, for interstitial solid solutions it is debated, whether interstitials segregate at SFs [173], i.e. the Suzuki effect, effectively altering $\Delta G_{chem}^{\gamma\to\varepsilon}$ on a local scale [174].

Based on Eqs. (2.41) and (2.42), it is apparent that the determination of γ_{isf} by thermodynamic modelling depends on databases for $\Delta G_{chem}^{\gamma\to\varepsilon}$ and $\Delta G_{mag}^{\gamma\to\varepsilon}$, e.g. as implemented in ThermoCalc [175] or the SGTE database [176]. The issue associated with these databases is that they only contain limited data for low temperatures, rendering them unreliable at e.g. room temperature and below [177,178].

2.4.5.2 Density functional theory

Apart from thermodynamic modelling and experimental investigations, a material's SFE can be further calculated using density functional theory (DFT) calculations. The most widely applied methods to calculate the SFE by DFT are the projector-augmented wave (PAW) method as implemented in the Vienna ab initio simulation package (VASP) [179,180] as well as the coherent potential approximation (CPA) [181,182] as implemented in the exact muffin-tin orbital (EMTO) package [182,183]. The advantages and disadvantages of the respective methods are summarized in Table 2.2, cf. Ref. [156].

Table 2.2: Comparison of capabilities of the Vienna ab initio simulation package (VASP) with those of the exact muffin-tin orbital (EMTO) package in calculating stacking fault energies according to Ref. [156]. NM, FM, and PM stand for nonmagnetic, ferromagnetic, and paramagnetic, respectively.

	EMTO	**VASP**
Chemical complexity	Approximated	Explicit
Atomic relaxations	No	Yes
Magnetism	NM, PM, FM	NM, FM
Finite temperature effects	Yes	Yes
SRO	No	Yes

Both VASP as well EMTO offer the opportunity to calculate SFE values based on a supercell approach [184], or the so-called axial-interaction model [185,186]. In the supercell approach, the SFE is determined by comparing the total energies of two chemically identical supercells, one corresponding to a perfect *fcc* lattice, while the other supercell contains a SF. In contrast, the axial-interaction model is based on calculating the SFE from the Helmholtz energies of the hcp (F_{hcp}) and *fcc* (F_{fcc}) crystal structure

$$\gamma_{isf}^{DFT} = \frac{2\left(F_{fcc}-F_{hcp}\right)}{A_{SF}}, \tag{2.43}$$

where A_{SF} is the stacking fault area. It is noted that γ_{isf}^{DFT} neglects strain energies, while these are contained in experimental SFE values.

2.5 Influencing factors on the stacking fault energy

Recalling the definition of the SFE by Olson & Cohen, it is apparent that γ_{isf} depends on a material's chemical composition [171,187–189] as well as on temperature [104,105,108,190–194] and pressure [195,196], since $\Delta G^{\gamma\rightarrow\varepsilon} f(p,T)$. In addition to the aforementioned influencing factors, the austenite grain size is further reported to affect γ_{isf} [197–202].

2.5.1 Chemical composition

The chemical composition has a direct influence on $\Delta G_{chem}^{\gamma\rightarrow\varepsilon}$ and therefore γ_{isf}, which is confirmed by experimental as well as theoretical investigations. However, whether an alloying element increases or decreases γ_{isf} and to what extent is especially for interstitial alloying elements of ongoing debate. The following section focuses on the effect of certain alloying elements on γ_{isf} in iron-based *fcc* steels as well as *fcc* high-entropy alloys. For other alloying systems, the effect of these alloying elements might be significantly different.

The addition of **Ni** results in an increases in γ_{isf}, which has been proven both by experiments [188,190,203] and simulations [190,204]. The exact extent by which Ni increases γ_{isf} varies, nevertheless γ_{isf} increases linearly with the Ni-content [188,190,203,204]. Contrary, **Cr**-addition is reported to lead to a slight decrease in γ_{isf} [205]. **Co** is reported to significantly reduce γ_{isf} [121,206–208], as e.g. in the case of CrCrFeNiMn HEAs [121,206] . Experiments indicate that the effect of **Mn** on the SFE is non-linear [209]. For Mn-contents < 22 wt.%, alloying with Mn leads to a decrease in γ_{isf}, while for contents exceeding 22 wt. % further Mn-addition is

reported to increase the SFE [209]. Although, DFT predicts a linear increase in SFE with increasing Mn-content [172]. In line with the effect of Co, the addition of **Si** is reported to lead to a reduction in SFE [171,210–214]. In contrast, **Al**-alloying leads to an increase in SFE [212,213]. While the effect of substitutional alloying on the SFE is mostly consistent in literature, the reported effect of interstitial elements, such as C and N, on the SFE is inconsistent. In case of **N**, both a decrease [34,39], an increase [21,35,41,42], as well as non-linear [33,37,40,43] effects have been reported for N-alloying. While for **C**, increases in SFE [21,32,36,38,39], no or little effect [37], or non-linear trends [215,216] have been reported. However, given the strong austenite stabilizing effect of N and C [21,217], it is considered likely that N- and/or C-alloying should result in an increase in the SFE. Consistently, recent DFT calculations do confirm this [218].

2.5.2 Temperature

In comparison to the influence of the chemical composition, few experimental studies investigated the effect of temperature on γ_{isf}. However, experimentel as well as theoretical findings indicate that the effect of temperature on γ_{isf} depends on the material/chemical composition [191]. While for pure *fcc* metals an increase in temperature leads to a decrease in γ_{isf} [191,193], the SFE of *fcc* steels and HEAs is reported to increase with increasing temperature [108,113,190,192].

2.5.3 Pressure

The effect of the pressure on a material's SFE is proportional to the difference in atomic volume ($\Delta V_{\gamma-\varepsilon} = V_\gamma - V_\varepsilon$) between austenite and ε −martensite, which follows from the total differential of the Gibbs energy. For $\Delta V_{\gamma-\varepsilon} < 0$, an increase in

pressure will lead to an increase in SFE, while for $\Delta V_{\gamma-\varepsilon} > 0$ increasing pressures will reduce the SFE. Most studies on the effect of pressure on SFE are theoretical [195,196], although high-pressure experiments using diamond anvil cells reporting allotropism in HEAs (ε −martensite formation) support theoretical findings that indicate a reduction in SFE for HEAs [219].

2.5.4 Grain size

The grain size has a significant influence on the stability of austenite, i.e. smaller grain sizes result in a decrease in the martensite start temperature. Lee & Choi [201] concluded that grain refinement leads to an excess free energy term (ΔG_{ex}) for the transformation

$$\Delta G_{ex} = 170.06\ exp\left(\frac{D}{18.55}\right), \tag{2.44}$$

where D is the grain size. According to Lee & Choi [201], the equation by Olson & Cohen for γ_{isf} has to also include ΔG_{ex}. It follows from Eq. (2.44) and Eq. (2.45)

$$\gamma_{isf} = n\rho_A\left((\Delta G_{chem}^{\gamma\to\varepsilon} + \Delta G_{mag}^{\gamma\to\varepsilon} + \Delta G_{ex} + E^{str}\right) + 2\sigma^{surf}(n). \tag{2.45}$$

Experimental evidence of D having an effect on the SFE is rare, although it was demonstrated that a decrease in D results in higher SFE values [199,200]. This is in agreement with studies reporting a decrease in martensite and twin formation upon deformation for smaller grain sizes [12,134,198,220–224].

2.6 The principle of alloy design by stacking fault energy engineering

Synthesizing alloys with high strength and ductility to overcome the strength-ductility trade-off is the holy grail in designing structural materials [1–3]. For materials deforming solely by dislocation glide, the introduction of obstacles to dislocation motion results inevitably in a reduction in ductility. On the contrary, TRIP and TWIP cause higher work hardening, which delays the occurrence of necking in uniaxial tension. Hence, why not design materials that either have a small grain size, contain precipitates, or exhibit a high degree of solid solution hardening and still deform by TRIP or TWIP? Certainly, these materials should exhibit advantageous combinations of strength and ductility.

HEAs and MEAs, such as CoCrFeMnNi and CoCrNi, are examples of alloys that exhibit high intrinsic strength due to solid solution hardening and can deform through TWIP or TRIP, depending on the deformation temperature [109,119,120,154]. These alloys demonstrate superior combinations of strength and ductility compared to materials that deform primarily by dislocation glide. Additionally, by alloying TRIP/TWIP materials with interstitial elements, further improvements in their mechanical properties can be achieved while maintaining a high ductility [29,225].

Schneider & Laplanche [119] argued that the effect of TWIP/TRIP on the WHR and, consequently, the delay of necking depends significantly on when twinning or martensite formation occurs. If twins or martensite form before the onset of cross-slip, they can lead to a significant increase in WHR and a higher ductility [119,120]. On the other hand, if twinning or martensite formation occurs after the onset of

cross-slip, the effect on WHR is lower, and the associated increase in ductility is less pronounced [120]. Hence, it is essential to not only control whether a material forms twins or martensite upon plastic deformation, but also the onset of the TRIP/TWIP effect.

As discussed above, the SFE controls the prevalence of dislocation glide, TWIP and/or TRIP. Furthermore, at least for twinning the critical resolved shear stress to form twins appears to depend on the SFE. Hence, by tailoring the SFE to a level where TWIP/TRIP is favored, while maximizing i.e. solid solution hardening by interstitial alloying, materials with favorable combinations of strength and ductility can be synthesized. However, this requires that the effect of alloying on the SFE, especially with the advent of HEAs, can be accurately described.

2.7 Differences in experimental and theoretical assessments of the stacking fault energy

As discussed above, the SFE can be assessed both by theoretical/computational and experimental methods. For pure *fcc* metals theoretical and experimental SFE values and their dependence on temperature are in relatively good agreement. However the situation changes for metastable *fcc* materials ($\Delta G^{\gamma \rightarrow \varepsilon} < 0$) [206]. For Ni-Co alloys, the theoretical SFE decreases with increasing Co-content and eventually becomes negative [206,207], while experimental SFE values remain positive [208]. Similar observations apply to the Cu-Al [169] and Cu-Zn [169] system and were recently shown to apply also in case of HEAs [226], MEAs [226], as well as austenitic steels of the Fe-Mn-C-(Al-Si) and Fe-Cr-Ni-(Mn) alloy systems [170]. Sun et al. [206] reason that the discrepancy between positive experimental

and negative theoretical SFE values cannot arise solely from an inappropriate treatment of the temperature effect in ab initio calculations. Instead, Sun et al. [206] suggest that experimental SFE values are affected by lattice friction which retards the movement of Shockley partial dislocations and keeps the SFs in metastable *fcc* alloys from attaining infinite widths. Similar conclusions were presented by Wei & Tasan [227] as well as Shih et al. [228]. Accordingly, if experimental SFE values are affected by lattice friction, experimentally determined SFE values are not reliable and cannot be used to verify results obtained by computational methods. This implies that alloy design by tailoring the SFE based on computational methods remains a trial-and-error approach.

3 Reassessing the experimental determination of the stacking fault energy

As discussed in Section 2.4, the current experimental assessment of SFE values departs from the assumption that Shockley partial dislocations can glide freely in their glide plane. This assumption is supported by the work from Byun [128], who concludes that resistance against Shockley partial dislocation movement is negligible. However, as pointed out by Baudouin et al. [229], Byun assumes that the dislocation line vector is fixed and that the Burgers vector rotates in the slip plane. This causes a rotation of the Burgers vector with respect to the applied stress tensor. Baudouin et al. [229] reason that Byun's assumption is flawed due to the following reasons:

i. The direction of the Burgers vector has to correspond to a close-packed direction and can therefore not rotate freely
ii. The Burgers vector must be constant along a dislocation loop, while the dislocation line vector changes

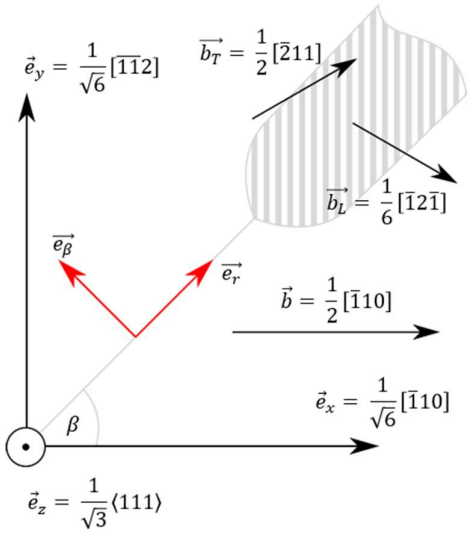

Figure 3.1: Geometric description of the dissociation of Shockley partial dislocations and the effect of applied stresses. Reproduced from Ref. [229] with permission from Elsevier.

The dissociation of a perfect dislocation into two Shockley partial dislocations is shown in Figure 3.1. The glide plane is defined as the x-y plane, with the Burgers vectors of the perfect $\vec{b} = \frac{1}{2}[\bar{1}10]$, leading $\vec{b}_L = \frac{1}{6}[\bar{1}2\bar{1}]$, and trailing Shockley partial $\vec{b}_T = \frac{1}{6}[\bar{2}11]$, respectively. While an applied stress acting on the dislocations is described by the stress tensor (Σ) in the defined Cartesian coordinate system

$$\sum \begin{pmatrix} \sigma_{xx} & \tau_{xy} & \tau_{xz} \\ \tau_{yx} & \sigma_{yy} & \tau_{yz} \\ \tau_{zx} & \tau_{zy} & \sigma_{zz} \end{pmatrix}. \tag{3.1}$$

The force balance of the leading Shockley partial dislocation in is given by

$$\vec{F}_L = \vec{F}_{el} - \gamma_{isf}\vec{e}_\beta + \vec{F}_{PK,L} + \delta_L \vec{F}_f \vec{e}_\beta, \tag{3.2}$$

where $\vec{F}_{el}$ is the elastic interaction between the two Shockley partials, $\gamma_{isf}\vec{e}_\beta$ the force exerted from the SFE on the leading Shockley partial dislocation, $\vec{F}_{PK,L}$ the Peach-Köhler force exerted on the leading partial due to Σ, $\vec{F}_f$ the friction force

acting against the movement of the leading Shockley partial dislocation, and δ_L is a sign parameter that depends on the direction of movement of the partial dislocation. It follows for the trailing Shockley partial dislocation

$$\vec{F}_T = \vec{F}_{el} - \gamma_{isf}\vec{e}_\beta + \vec{F}_{PK,T} + \delta_T \vec{F}_f \vec{e}_\beta. \tag{3.3}$$

Note that it is assumed that the friction forces acting on the trailing and leading Shockley partial dislocations are equal in magnitude [229]. Projecting $\vec{F}_L$ and $\vec{F}_T$ on $\vec{e}_\beta$ gives, for the leading Shockley partial

$$F_L = \vec{F}_L \vec{e}_\beta = F_{el} - \gamma_{isf} + F_{PK,L} + \delta_L F_f, \tag{3.4}$$

and for the trailing partial

$$F_T = \vec{F}_T \vec{e}_\beta = -F_{el} + \gamma_{isf} + F_{PK,T} + \delta_T F_f, \tag{3.5}$$

with the Peach-Köhler forces for the leading

$$F_{PK,L} = \frac{a\sqrt{2}}{4}\tau_{xz} + \frac{a\sqrt{6}}{12}\tau_{yz} \tag{3.6}$$

and trailing partial dislocations

$$F_{PK,T} = \frac{a\sqrt{2}}{4}\tau_{xz} - \frac{a\sqrt{6}}{12}\tau_{yz}, \tag{3.7}$$

respectively. As expected, the only stress components affecting the stacking fault width are those parallel to components of the respective Burgers vector. In the case of no externally applied stress, the stacking fault width is determined by the force balance over the stacking fault neglecting with $F_{PK,L} = F_{PK,T} = 0$. It follows

$$F_L - F_T = 0. \tag{3.8}$$

Inserting Eqs. (3.4) and (3.5) into Eq. (3.8)

$$F_{el} - \gamma_{isf} + \delta_L F_f - \left(-F_{el} + \gamma_{isf} + \delta_T F_f\right) = 0 \tag{3.9}$$

and simplifying Eq. (3.9) results in

$$2F_{el} - 2\gamma_{isf} + \delta_L F_f - \delta_T F_f = 0. \tag{3.10}$$

If the Shockley partial dislocations move away from each other to reach their equilibrium distance, $\delta_L = -1$ and $\delta_T = +1$. Therefore, Eq. (3.10) becomes

$$2F_{el} - 2\gamma_{isf} + 2F_f = 0, \tag{3.11}$$

with $F_{el} = \frac{\mu b_p^2}{4\pi d_{SF}}\left(\frac{2-\nu}{1-\nu}\right)\left(1 - \frac{2\nu\cos(2\beta)}{2-\nu}\right)$ (Eq. (2.19)) it follows

$$\gamma_{isf} + F_f = \frac{\mu b_p^2}{4\pi d_{SF}}\left(\frac{2-\nu}{1-\nu}\right)\left(1 - \frac{2\nu\cos(2\beta)}{2-\nu}\right). \tag{3.12}$$

If we now consider that F_f corresponds to the Peach-Köhler due to critical resolved shear stress for Shockley partial dislocations ($F_f = \tau_p b_p$), Eq. (3.12) becomes

$$\gamma_{isf} + \tau_p b_p = \frac{\mu b_p^2}{4\pi d_{SF}}\left(\frac{2-\nu}{1-\nu}\right)\left(1 - \frac{2\nu\cos(2\beta)}{2-\nu}\right). \tag{3.13}$$

Hence, experimentally determined values for the SFE are the sum of a material's actual intrinsic SFE and $\tau_p b_p$

$$\gamma_{isf}^{Exp} = \gamma_{isf} + \tau_p b_p. \tag{3.14}$$

If it is assumed that the SFE determined by DFT corresponds to a material's actual intrinsic SFE. ($\gamma_{isf} = \gamma_{isf}^{DFT}$), Eq. (3.14) implies that experimental and theoretical SFE values can only be compared to each other, if the contribution of $\tau_p b_p$to γ_{isf}^{Exp} is taken into account.

4 Summary of results

This chapter provides a brief overview of the main results of this Ph.D. project. For more detailed information the reader is referred to the individual manuscripts in Chapters 5 – 7.

4.1 Manuscript I

Experimental validation of negative stacking fault energies in metastable face-centered cubic materials

This study aimed to address the disparity between positive experimental stacking fault energy (SFE) values and negative SFE values obtained from density functional theory (DFT) calculations in metastable face-centered cubic alloys. In summary, the study suggests that that DFT treats the stacking fault energy as a variable of state and assumes that Shockley partial dislocations can glide freely on their glide plane, while the resistance against movement of Shockley partial dislocations affects experimental SFE values. Therefore, experimental SFE data should be considered as apparent values, which differ from the theoretically determined SFEs. The apparent SFEs comprise the intrinsic SFE of the material and an excess SFE resulting from the critical resolved shear stress for twinning. As a result, experimental SFE values are always positive and dependent on grain size in a manner similar to the Hall-Petch effect. By correcting the experimental SFEs accordingly, the study achieves intrinsic SFE values that align remarkably well with DFT predictions for metastable systems with negative stacking fault energies.

4.2 Manuscript II

Reconciling experimental and theoretical stacking fault energies in face-centered cubic materials with the experimental twinning stress

The primary objective of this study was to expand upon the proposed correction method for experimental stacking fault energy (SFE) values in metastable face-centered cubic materials, as described in Manuscript I. The aim was to apply this correction to stable alloys and pure metals and to demonstrate the mismatch of previously suggested models linking the critical resolved shear stress for twinning and experimental SFE values with experimental observations. There is a widely accepted belief that stacking fault energy and twinning stress are closely related. Existing models all predict a decrease in twinning stress as stacking fault energy decreases, assuming that the intrinsic stacking fault energy possesses a positive value. However, contrary to these predictions, it has been observed that twinning stress increases with decreasing SFE in medium- and high-entropy alloys. Furthermore, while first principles methods predict negative intrinsic stacking fault energy values for metastable materials, experimental measurements consistently yield positive values. In this study, it is proposed that scaling the twinning stress by the Burgers vector can bridge the gap between intrinsic and experimentally measured stacking fault energy. This hypothesis was tested on Cu-Al alloys, pure metals, and medium- and high-entropy alloys, providing a consistent and quantifiable interpretation of data for alloys exhibiting both positive and negative stacking fault energy for the first time.

4.3 Manuscript III

Experimental and computational assessment of the temperature dependency of the stacking fault energy in face-centered cubic high-entropy alloy

The stacking fault energy is considered and important design criterion in synthesizing strong and ductile materials. Experimentally determined stacking fault energy values are considered an inherent materials property and are exclusively positive. Nevertheless, this assumption is challenged by results obtained from first principle methods, which show that the intrinsic stacking fault energy of metastable face-centered cubic is negative. The hypothesis presented in Manuscripts I and II appears to reconcile experimental and theoretical stacking fault energies. Although, the assessment of the critical stress for twinning, which is commonly done by transmission electron microscopy, is laborious. Instead, the work in this manuscript explores the opportunity to reconcile experiments and theory based on single in-situ neutron diffraction experiments, by determining the critical resolved shear stress for Shockley partial dislocations from stacking fault probability versus true stress curves in line with the experimental determination of the stacking fault energy. The presented results showcase that in-situ neutron diffraction offers the opportunity to determine both these values and thus reconcile theory and experiments.

5 Manuscript I:

Experimental validation of negative stacking fault energies in metastable face-centered cubic materials[1]

Konstantin V. Werner*, Frank Niessen, Matteo Villa, Marcel A. J. Somers

*Correpsonding author. E-mail address: kviwe@mek.dtu.dk

Department of Mechanical Engineering, Technical University of Denmark,

Produktionstorvet, Building 425, 2800 Kongens Lyngby, Denmark

Keywords: Metastable alloy, Stacking fault energy, Twinning, High-entropy alloy

5.1 Abstract

Stacking fault energy (SFE) is considered an important parameter to predict the prevalent plastic deformation mechanism in face-centered cubic (*fcc*) alloys. Experimental methods for determining SFE presuppose that SFE is positive. Density functional theory (DFT) is a promising tool to predict alloy compositions with low SFEs and desirable mechanical properties. For *metastable fcc* alloys, DFT predicts negative SFE values, which cannot be validated by the existing experimental procedures. In this contribution, it is demonstrated that experimental procedures to assess SFE values only provide an *apparent* value that needs correction. The suggested correction relies on the critical resolved shear stress for

[1] Published work: Werner, K. V., Niessen, F., Villa, M., Somers, M. A. J., “Experimental validation of negative stacking fault energies in metastable face-centered cubic materials”, Appl. Phys. Lett. 119, 141902 (2021) https://doi.org/10.1063/5.0063761 [248]. The format of the published article has been adapted to fit the format of the Ph.D. thesis.

twinning, which is grain size-dependent, just like the apparent SFE. The correction provides SFE values that are independent of grain size. Accordingly, negative SFEs predicted by DFT can be experimentally validated.

5.2 Introduction

Metastable face-centered cubic (*fcc*) metals and alloys, such as Fe-Cr-Ni and Fe-Mn-C austenitic steels, high-entropy alloys (HEAs) and medium-entropy alloys (MEAs), are characterized by an *fcc* structure that is not in thermodynamic equilibrium at room temperature. Under the influence of externally applied forces these metastable alloys can develop deformation-induced martensite and deformation-induced twins. These deformation mechanisms are commonly referred to as transformation-induced plasticity (TRIP) and twinning-induced plasticity (TWIP), respectively. Deformation-induced martensite and deformation-induced twins can provide additional ductility and strength. As compared to classical dislocation slip, deformation-induced martensite and deformation-induced twins play a pivotal role in attempting to overcome the well-known strength-ductility trade-off in structural materials [1,3].

The current paradigm for tailoring the (combination of) deformation mechanism in *fcc* metals is tailoring the intrinsic stacking fault energy (SFE) [15,23], which is the excess energy associated with a stacking fault suspended between the leading and trailing Shockley partial dislocations that result from the dissociation of a full dislocation. The SFE depends on the materials' chemical composition at given temperature and pressure [39,187,188,196]. It is considered common knowledge that, with increasing SFE, the prevalent deformation mechanism changes from TRIP to TWIP to slip [21,23,117]. For example, austenitic steels with an

experimental SFE $< 20\ \mathrm{mJ} \cdot \mathrm{m}^{-2}$ are expected to transform into either hexagonal-close packed (hcp) ε-, or body-centered cubic (*bcc*) α'-martensite (TRIP) [21,22]. For experimental SFEs in the range $\sim 20 - 45\ \mathrm{mJ} \cdot \mathrm{m}^{-2}$, deformation twinning (TWIP) is preferred [21]. For SFEs $> 45\ \mathrm{mJ} \cdot \mathrm{m}^{-2}$, austenitic steels are expected to deform by slip [22].

Density functional theory (DFT) is a popular tool to map uncharted composition spaces and identify the composition range of materials with superior properties [20]. For thermodynamically *stable fcc* metals and alloys, DFT calculations can provide values for the SFE that are in good agreement with experimentally determined values, without the use of fitting parameters [169,193]. Conversely, for *metastable fcc* materials, Sun et al. recently pointed out a severe discrepancy between experimentally determined and DFT-predicted SFE values [206]. They identified an incomplete definition of SFE in the currently applied experimental approaches as the origin of the discrepancy. Specifically, experimental methods for SFE determination presuppose positive SFE values, while DFT provides negative SFE values for metastable alloys, consistent with the thermodynamic definition of a metastable system [206]. Sun et al.´s work implies that theoretical SFE values for metastable materials cannot be validated and reconciled with the present consensus on experimental SFE determination [206]. Furthermore, their work would suggest that tailoring the deformation mechanisms in metastable *fcc* materials by compositionally adjusting the experimental SFE, i.e. alloy optimization by tailoring of the experimental SFE, is a questionable scientific paradigm.

In addition to the invalidating implications of Sun et al.´s work, it is noted that tailoring the deformation mechanism via the composition-dependent SFE appears an incomplete concept, because the microstructural features, in particular the grain

size, are well known to influence a material's propensity for TRIP and TWIP [12,134,221]. Fine-grained materials exhibit less pronounced TRIP or TWIP than coarse-grained materials with identical chemical composition [198,220,223]. Moreover, grain refinement was demonstrated to possibly fully suppress deformation-induced twinning [222].

In the present communication, the shortcomings of experimental SFE determination are addressed and a route for experimental evaluation of positive *and* negative SFE values is proposed. This method can also account for the effect of grain size on the observed deformation mechanism. It is demonstrated that experimentally determined SFE values are apparent values that are not only determined by the composition, but also by the material's microstructure.

5.3 Methods

Currently, experimental stacking fault energies are assessed by transmission electron microscopy (TEM) or by X-ray (XRD) and neutron diffraction (ND). In TEM, the intrinsic SFE, hereby labelled apparent/experimental (γ_{isf}^{app}), is determined from the separation distance (d) of isolated corresponding pairs of leading and trailing partial dislocations. The approach assumes a balance of the excess energy stored in the stacking fault and the elastic strain energy responsible for mutual repulsion of leading and trailing partials [230–232]:

$$\gamma_{isf}^{app} = \frac{\mu b_p^2}{8\pi d}\frac{2-\nu}{1-\nu}\left(1-\frac{2\nu\cos 2\beta}{2-\nu}\right) \tag{5.1}$$

where b_p is the Burgers vector of the partial dislocation, μ is the shear modulus, ν is Poisson's ratio and β is the angle between the direction of the full dislocation

and its Burgers vector. It is essential to point out that this approach implicitly assumes that the partial dislocations can glide freely in their glide plane and that the only force counteracting the mutual repulsion of the partial dislocations is the obtained SFE value. SFE determination by XRD and ND is based on the shift and broadening of the Bragg peak and commonly employs the method by Reed & Schramm [39,157], which is based on work by Otte et al. and Adler & Otte [158,159,233] and adopts the relation between stacking fault probability (α), dislocation density (ρ) and γ_{isf}^{app} as identified by Smallmann & Westmacott [160]:

$$\gamma_{isf}^{app} = \frac{K_{111}\omega_0\mu_{111}a_0}{\sqrt{3}\pi} A^{-0.37} \frac{\langle\varepsilon_{111}^2\rangle}{\alpha} \tag{5.2}$$

where $\langle\varepsilon_{hk}^2\rangle$ is the mean-square microstrain, $K_{hkl}\omega_0$ is a ***positive*** proportionality constant with value 6.6 and A is the Zener anisotropy ($A = 2c_{44}/(c_{11} - c_{22})$). Additionally, Rafaja et al. [234] recently presented a method, based on the work by Byun [128], which assesses the SFE by determining the critical resolved shear stress required to create stacking faults (SFs) with an infinitely large separation distance between the leading and trailing partial dislocations. Despite being essentially different, both experimental approaches have in common that they presuppose a positive SFE value (cf. Eqs. (5.1 and (5.2).

A single SF is commonly modelled as an inclusion of ε-martensite (***hcp***) with a thickness of two dense-packed atomic planes [206,235]:

$$\gamma_{isf} = 2\rho_A(\Delta G^{\gamma\rightarrow\varepsilon} + E_{str}) + 2\sigma^{\gamma/\varepsilon} \tag{5.3}$$

where ρ_A is the molar electron density in the close packed $\{111\}$ planes, $\Delta G^{\gamma\rightarrow\varepsilon}$ is the chemical driving force of the γ to ε transformation, E_{str} is the strain energy and $\sigma^{\gamma/\varepsilon}$ is the energy associated with a coherent interface between austenite and ε-

martensite. E_{str} accounts for the lattice mismatch, i.e. coherency strains, between *fcc* and *hcp* and has a magnitude in the range $1 - 4\ \mathrm{mJ} \cdot \mathrm{m}^{-2}$ [235]. The interfacial energy cannot be directly assessed experimentally and is generally determined by subtracting $2\rho_A \Delta G^{\gamma \to \varepsilon}$ from the measured SFE and dividing by a factor two, as suggested by Olson & Cohen [235]. The interfacial energies thus determined are typically in the range $\sim 10 - 15\ \mathrm{mJ} \cdot \mathrm{m}^{-2}$ for common austenitic steels [170,236]. Sun et al. highlighted that the term $2\rho_A \Delta G^{\gamma \to \varepsilon}$ in Eq. (5.3) is equivalent to the intrinsic SFE from DFT, which is defined as the energy difference between two *fcc* supercells with and without a stacking fault [206], respectively. It is apparent that, for an increasingly negative chemical driving force, $\Delta G^{\gamma \to \varepsilon}$, (as for metastable *fcc* materials) Eq. (5.3) can yield a negative SFE value, even when strain and interfacial energies give a positive contribution. This, in turn, is synonymous with the fact that, in metastable *fcc* materials, Shockley partial dislocations must experience an additional excess force (F^* in Figure 5.1) that restrains their free movement within the glide plane to prevent the spontaneous transformation of metastable austenite into ε-martensite. Refs. [206,227] refer to this term as “friction force” and state that it must counterbalance the repulsive character of the elastic interaction between the two partial dislocations (F_{int}) and the SFE itself. Otherwise, experimental observations of SFs with *finite* widths in metastable materials cannot be reconciled with negative SFEs values.

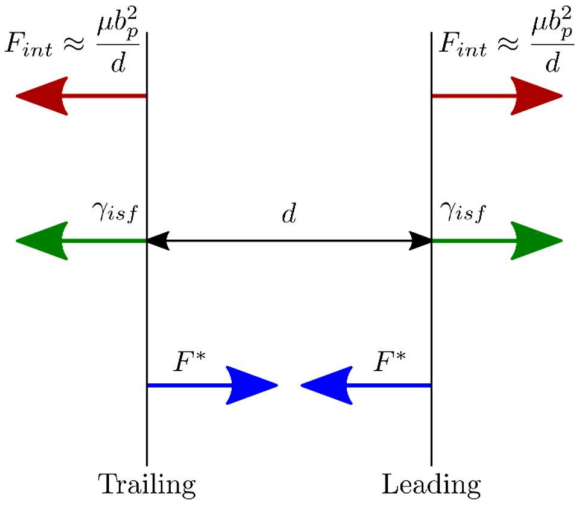

Figure 5.1: Schematic illustration of the force balance of a metastable fcc material with negative SFE. An additional excess force (F^*) balances the repulsive character of the elastic interaction of the two partial dislocations and the force experienced by the negative SFE to yield a finite separation distance d.

In contrast, DFT and thermodynamic modelling both treat the SFE as an energy difference between two equilibrium states, mainly characterized by $\Delta G^{\gamma \to \varepsilon}$. These equations of state accurately describe the change in energy associated with the formation of a stacking fault, γ_{isf}, but do not account for the effect of the resistance against the movement of partial dislocations, i.e. F^* in Figure 5.1. As this resistance to stacking fault formation in metastable materials is inevitably contained in experimentally determined SFE values, they cannot be directly compared with SFE values from equations of state.

5.4 Results and Discussion

In an attempt to reconcile positive and negative stacking fault energies with experimental observations of finite Shockley partial separation, it is proposed that

the experimentally determined, apparent, SFE (γ_{isf}^{app}), is the sum of the intrinsic SFE (γ_{isf}) and an excess SFE (γ^*):

$$\gamma_{isf}^{app} = \gamma_{isf} + \gamma^* \tag{5.4}$$

where Eq. (5.4) eventually links Eqs. (5.1) and (5.2) to Eq. (5.3). The excess SFE stems from the resistance against the movement of partial dislocations, which is experienced by the moving partial dislocations upon the full dislocation's dissociation. Similar to the critical resolved shear stress for slip, this resistance should be the sum of a grain size-independent term, i.e. the lattice friction associated with the Peierls potential and solid solution hardening, and a grain size-dependent term due to the back stress imposed onto the moving partial dislocations as a consequence of the finite dimensions of their glide plane, as for example constituted by grain boundaries. Apart from the aforementioned factors, the interaction of expanding SFs with Shockley partials that bound short SFs as well as other microstructural features [234] will influence γ_{isf}^{app}. A detailed derivation will be supplied in a future full-length paper. Moreover, it is well established that deformation twinning in *fcc* materials is closely related to the dissociation of dislocations and the formation of multi-layered stacking faults [126]. In addition, results by Lu et al. indicate that the effective energy barriers for twinning and the formation of a stacking fault are similar in magnitude (cf. Fig. 1c in Ref. [19]). While measuring the resistance against the movement of Shockley partial dislocations itself would be the ideal measure for the excess SFE, this quantity cannot be straightforwardly measured. The excess SFE is therefore approximated by the product of the critical resolved shear stress for twinning (τ_{twin}) and the Burgers vector of the Shockley partials ($\gamma^* = b_p \tau_{twin}$). Hence:

$$\gamma_{isf} = \gamma_{isf}^{app} - b_p \left(\tau_{0,twin} + \frac{K_{twin}^{HP}}{\sqrt{D}} \right) \quad (5.5)$$

where $\tau_{0,twin}$ is the critical resolved shear stress for twinning of a single crystalline material due to lattice friction and solid solution hardening, K_{twin}^{HP} is the critical resolved shear stress' Hall-Petch slope for twinning and D is the grain size. Eq. (5.5) allows both positive and negative values of γ_{isf} while γ_{isf}^{app} remains positive.

It has been demonstrated that the prevailing deformation mechanism in *fcc* metals may depend on the materials' microstructure, specifically on the grain size [200,237]. Given the empirical relation between experimentally determined SFE and deformation mechanism [21–24], apparent SFE values would similarly depend on the grain size. The proposed correction for experimentally determined SFEs in Eq. (5.5) implies a Hall-Petch-like dependence of γ_{isf}^{app} on the grain size. Unfortunately, only limited data is available to validate this implication. The SFE data determined as a function of the grain size for a Fe-24Mn-4Cr-0.5C TWIP [237] steel is presented in Figure 5.2a. Evidently, γ_{isf}^{app} indeed obeys a Hall-Petch-like dependence on the grain size. According to the interpretation of SFE measurements suggested above, this would imply easier TWIP for a larger grain size by an effective reduction in τ_{twin} (see Eq. (5.5)).

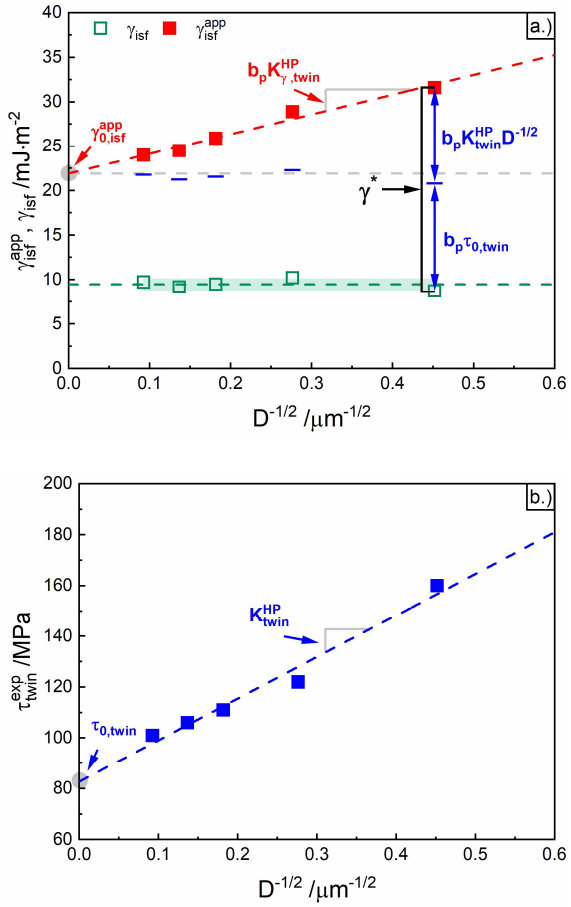

Figure 5.2: a.) γ_{isf}^{app} and γ_{isf} for a Fe-24Mn-4Cr-0.5C TWIP steel in dependence of D. γ_{isf}^{app} and the normal twinning stress were taken from Table 2 and Fig. 14 in Ref. [237]. b.) τ_{twin}^{exp} used for the correction was calculated from the reported normal twinning stress assuming a Taylor factor of 3.06.

The intercept of the linear fit (red dashed line) with the γ_{isf}^{app} axis represents the apparent SFE of single crystalline material (infinite grain size), while the slope of the line yields the Hall-Petch slope for the critical resolved shear stress for twinning (determined from γ_{isf}^{app}) $\mathrm{K}_{\gamma,\mathrm{twin}}^{\mathrm{HP}}$. The linear fit yields $\gamma_{0,isf}^{app} = 21.9\ \mathrm{mJ \cdot m^{-2}}$ for the infinitely large single crystal and $\mathrm{K}_{\gamma,\mathrm{twin}}^{\mathrm{HP}} = 152\ \mathrm{MPa \cdot \mu m^{1/2}}$ for the Hall-Petch slope. Lee et al. also determined the twinning stress experimentally (τ_{twin}^{exp}) as a function of D for the Fe-24Mn-4Cr-0.5C TWIP steel [237] as shown in Figure 5.2b. The

twinning stress can be used to evaluate the Hall-Petch slope (K_{twin}^{HP}) independently from the SFE data and can in principle be used to correct experimentally determined SFE values for γ^* (see Eq. (5.5)). Subtracting $b_p\tau_{twin}^{exp}$ from the experimental γ_{isf}^{app} values in Figure 5.2a yields the corrected SFE values (green squares in Figure 5.2a) that are independent of grain size (indicated by the light green band corresponding to the 95% confidence interval), as required by the definition of SFE. This indicates that the Hall-Petch slope for twinning ($K_{twin}^{HP} = 163\ \mathrm{MPa} \cdot \mu\mathrm{m}^{1/2}$) determined from τ_{twin}^{exp} is equal to the Hall-Petch slope ($K_{\gamma,twin}^{HP} = 152\ \mathrm{MPa} \cdot \mu\mathrm{m}^{1/2}$) determined from the apparent SFEs. Within this framework, the blue lines in Figure 5.2a correspond to the grain size-dependent ($b_p K_{twin}^{HP} D^{-1/2}$) and grain size-independent ($b_p\tau_{0,twin}$) contributions to γ^*, respectively. This validates Eq. (5.5), at least qualitatively. Quantitatively, the absolute value of γ_{isf} is expected to be offset by a value that corresponds to the difference between the interfacial energy as assumed by Lee et al. [237] ($\sigma^{\gamma/\varepsilon} = 9\ \mathrm{mJ} \cdot \mathrm{m}^{-2}$) and the actual interfacial energy.

Clearly, the question arises, whether a similar correction could be applied to other systems. In line with the observations made for the TWIP steel, the experimentally determined SFE data for a Fe-18Mn-3Si-0.6C TRIP steel shown in Figure 5.3 convincingly exhibit a Hall-Petch like dependence on D. Nevertheless, and in contrast to the data presented for the TWIP steel in Figure 5.2a, $\tau_{twin}^{exp}$was not determined. Hence, $\tau_{0,twin}$ is unknown and the overall γ^* term remains unrevealed for this material. It is therefore uncertain, whether the critical resolved shear stress for twinning is an adequate approximation of the resistance against the movement of partial dislocations in metastable *fcc* materials that deform by TRIP.

Nevertheless, the need for a correction for this resistance against the movement of partial dislocations in line with Eq. (5.5) is eminent from the SFE values [200] shown in Figure 5.3.

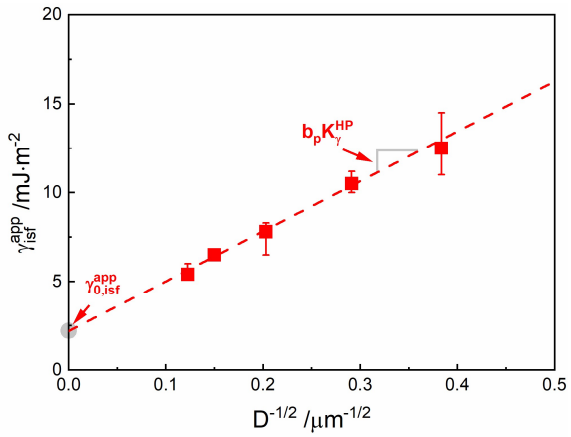

Figure 5.3: γ_{isf}^{app} plotted as a function of D for a Fe-18Mn-3Si-0.6C TRIP steel. Data extracted from Fig. 8b in Ref. [200].

Evidently, the validation of Eq. (5.5) requires very specific experimental data that is available only for a limited set of materials. Nevertheless, in several cases of metastable *fcc* materials that deform by TWIP, part of such data is available and can be used for an approximate evaluation of this quantity. Experimentally determined SFEs for selected MEAs and HEAs are given in Figure 5.4 (full symbols) and compared with SFEs predicted by DFT along the horizontal axis. Clearly, the values for γ_{isf}^{app} deviate significantly from those predicted by DFT: experimental values are positive, while the DFT values are negative. It was attempted to correct the experimental values in accordance with Eq. (5.5). The values shown in Figure 5.4 and used for the correction are collected in Table 5.1. The Hall-Petch slope for twinning could not be determined for any of the materials included in Figure 5.4, because data is lacking. Consequently, the exact grain-size-

dependent term of the excess SFE remains undetermined. Nevertheless, as conceivable from Figure 5.2a, the excess SFE is dominated by a grain-size independent term, provided that the grain size is not excessively small. The data, which was determined on polycrystalline specimens with different grain sizes, was corrected with twinning shear stresses experimentally determined on polycrystalline materials (see Table 5.1). The corrected SFE values γ_{isf} are indeed negative and in excellent agreement with the DFT results, despite the unknown grain size dependence. Consequently, the corrected SFEs may be off by some $\mathrm{mJ} \cdot \mathrm{m}^{-2}$ from the actual values.

The agreement between corrected experimental SFEs and predicted DFT SFEs is most encouraging. Note that γ_{isf}^{DFT} was calculated at $T = 300\ \mathrm{K}$ [206], which is in accordance with the temperature for the experimental SFEs, i.e. $T = 293\ \mathrm{K}$ [113,154,238–240].

Table 5.1: γ_{isf}^{app}, γ_{isf}^{DFT} and for τ_{twin}^{exp} corrected γ_{isf} of MEAs and HEAs. Theoretically predicted twinning stresses (τ_{twin}^{calc}) given as comparison to τ_{twin}^{exp}. D given in µm for polycrystalline materials if known, unknown grain size denoted by unk. Single crystalline materials are denoted by sx.

Alloy	$\boldsymbol{\gamma_{isf}^{DFT}}$	$\boldsymbol{\gamma_{isf}^{app}}$	$\boldsymbol{\gamma_{isf}}$	**a**	$\boldsymbol{\tau_{twin}^{exp}}$	$\boldsymbol{\tau_{twin}^{calc}}$	$\boldsymbol{D}$
at%	mJ·m^{-2}	mJ·m^{-2}	mJ·m^{-2}	Å	N·mm^{-2}	N·mm^{-2}	µm
CoCrNi	-21 [206]	18 ± 4 [238]	-19.5 ± 4	3.529 [238]	~260 [154]	291 [241]	unk.
		22 ± 4 [154]	-15.8 ± 4	3.567 [154]			16 [154]
CoCrFeNi	-1 [206]	32.5 [113]	-2.5	3.604 [113]	~238 [113]	274 [241]	35 [113]
		27 ± 4 [238]	-7.6 ± 4	3.565 [238]			unk.

CoCrFeMnNi	-5 [206]	30 ± 5 [239] 26.5 ± 4 [238]	-4.3 ± 5 -7.8 ± 4	3.576 [238]	~235 [120]	236 [241]	unk. unk.
$Fe_{40}Mn_{40}Co_{10}Cr_{10}$	-3 [206]	13 ± 4 [240]	-4.1 ± 4	3.610 [240]	~116 [242]	-	sx. [240]

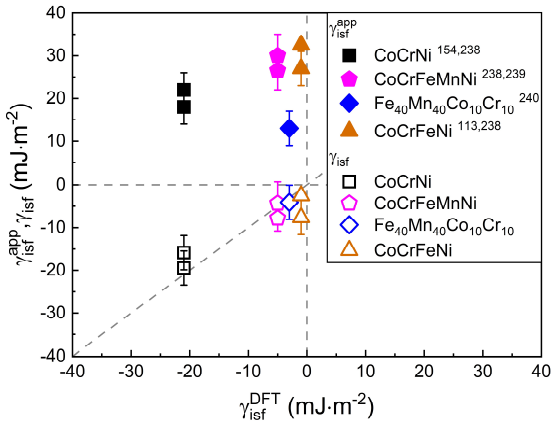

Figure 5.4: γ_{isf}^{app} and γ_{isf} of HEAs and MEAs [113,154,238–240] corrected via Eq. (5.5) versus γ_{isf}^{DFT} [206].

Furthermore, the SFE and the twinning shear stress for $Fe_{40}Mn_{40}Co_{10}Cr_{10}$ were determined on single crystals [240,242]. The experimentally determined SFE is hence independent of grain size and the corrected γ_{isf} of the $Fe_{40}Mn_{40}Co_{10}Cr_{10}$ requires no further correction for the effect of the grain size and can be regarded as the "actual" experimental SFE for an "infinitely" large crystal. Certainly, for this alloy excellent correspondence is obtained between the corrected experimental SFE and the DFT-predicted SFE.

Owing to the limited availability of room temperature SFE values predicted by DFT, it remains to be verified, whether the critical resolved shear stress for twining can adequately describe the resistance against movement of partial dislocations for *fcc*

materials that deform by TRIP and slip. Nevertheless, since γ_{isf}^{app} is the sum of γ_{isf} and a grain-size dependent γ^*, it is recommended that reviews [243] on the influence of alloying elements on the SFE of alloys are carefully reevaluated. It needs to be ascertained that the reported influences of alloying elements on the SFE are indeed related to the chemical composition and do not originate from grain-size dependent variations in γ^*.

The present findings suggest that a concerted approach of adjusting SFE and grain size appears necessary rather than tailoring the (combination of) deformation mechanism(s) in *fcc* materials merely by adjusting the composition. Moreover, thermodynamics represents only a part of the chemical composition's influence on the apparent SFE of a material, and information on the influence of the alloying elements on the grain size independent excess energy should be included to arrive at reliable tailoring of the (combination of) deformation mechanism(s).

5.5 Conclusions

Summarizing, experimental SFE data should be regarded as apparent SFE values, which deviates from theoretically determined SFEs. Apparent SFEs are the sum of a material's intrinsic SFE and an excess SFE that appears to arise from the critical resolved shear stress for twinning, which is always positive and depends on grain size according to a Hall-Petch like dependence. Correcting experimental SFEs accordingly, yields intrinsic SFEs that are in excellent agreement with DFT-predictions also for metastable systems with negative stacking fault energies.

5.6 Acknowledgements

This work was funded by the Independent Research Fund Denmark as part of the project SFETailor (grant-number: 9041-00145B). The authors would like to thank Grethe Winther and Wolfgang Pantleon from the Technical University of Denmark (DTU), Department of Mechanical Engineering, as well as Song Lu from the Royal Institute of Technolgy (KTH), Department of Materials Science and Engineering, for valuable scientific discussions.

6 Manuscript II:

Reconciling experimental and theoretical stacking fault energies in *face-centered cubic* materials with the experimental twinning stress[2]

Konstantin V. Werner[1]*, Frank Niessen[1], Wei Li[2,3], Song Lu[2], Levente Vitos[2,3,4], Matteo Villa[1], Marcel A. J. Somers[1]

*Corresponding author. E-mail address: kviwe@mek.dtu.dk

[1]Department of Civil and Mechanical Engineering, Technical University of Denmark, Produktionstorvet, Building 425, 2800 Kongens Lyngby, Denmark

[2]Applied Materials Physics, Department of Materials Science and Engineering, Royal Institute of Technology, Stockholm SE-100 44, Sweden

[3]Department of Physics and Astronomy, Division of Materials Theory, Uppsala University, P.O. Box 516, SE-75121 Uppsala, Sweden

[4]Research Institute for Solid State Physics and Optics, Wigner Research Center for Physics, P.O. Box 49, H-1525 Budapest, Hungary

6.1 Abstract

Stacking fault energy and twinning stress are thought to be closely correlated. All currently available models predict a monotonous decrease in twinning stress with decreasing stacking fault energy and depart from the assumption that the intrinsic

[2] Published work: Werner, K. V., Niessen, F., Li, W., Lu, S., Vitos, L., Villa, M., Somers, M. A. J., "Reconciling experimental and theoretical stacking fault energies in face-centered cubic materials with the experimental twinning stress", Materialia, Vol. 27, 2023, https://doi.org/10.1016/j.mtla.2023.101708 [301]. The format of the published article has been adapted to fit the format of the Ph.D. thesis.

stacking fault energy has a positive value. Opposite to this prediction, for medium- and high-entropy alloys the twinning stress was shown to increase with decreasing SFE. Additionally, for metastable materials, first principles methods predict negative intrinsic stacking fault energy values, whilst experimentally determined values are always positive. In the present communication, it is postulated that the twinning stress scaled by the Burgers vector bridges the difference between intrinsic and experimentally measured stacking fault energy. The assumption is tested for Cu-Al alloys, for pure metals and for medium- and high-entropy alloys and, for the first time, provides a consistent quantitative interpretation of data for both alloys with positive and negative stacking fault energy.

Keywords: Metastable phases, Stacking fault energy, Twinning, Density functional theory

6.2 Introduction

The stacking fault energy (SFE) is the energy associated with a stacking fault (SF) bounded by a leading and a trailing Shockley partial dislocation, that result from the dissociation of a full dislocation. In face-centered cubic (*fcc*) alloys, SFE is assumed to determine the predominant plastic deformation mechanism. In dependence on temperature and pressure, the SFE of alloys can be tailored by changing the chemical composition [39,187,188,196]. For increasing SFE, the prevalent deformation mechanism changes from martensite formation to deformation twinning to, exclusively, dislocation slip [21,23,117].

Experimentally, SFE values are assessed from transmission electron microscopy (TEM) observations of Shockley partial dislocation configurations, e.g. in extended

dislocation nodes [150], SF tetrahedra [244], and from the separation between two Shockley partial dislocations, i.e. the SF width, by strong beam [245] and weak beam dark-field imaging (WBDF) [152]. Occasionally, high-resolution transmission electron microscopy (HRTEM) is applied [246]. Other frequently applied methods, e.g. X-ray and neutron diffraction do not enable direct assessment of SFE values [157], but are calibrated relying on TEM results.

Following the correlation of SFE and prevalent deformation mechanisms in *fcc* materials, Eqs. (6.1 – (6.4 in Table 6.1 were proposed to interrelate experimentally determined SFE values and the experimentally determined critical resolved shear stress for twinning (τ_{Twin}). Models proposed by Narita & Takamura [130] and Byun [128] conceive the experimentally determined SFE as an intrinsic materials property and predict a monotonous decrease of τ_{Twin} with decreasing SFE. The tendency of a material to undergo deformation twinning is also influenced by the microstructure. Smaller grains require a higher critical resolved shear stress to form deformation twins [198,220], while in ultra-fine grains twinning is fully suppressed [222]. Accordingly, Gutierrez-Urrutia et al. [134] and Meyers et al. [133] extended Byun´s work to include the influence of grain size (Eqs. (6.3 and (6.4 in Table 6.1).

Table 6.1: Models describing the relation of the critical resolved shear stress for twinning with the SFE obtained via experiments

Reference	Critical resolved shear stress for twinning, τ_{Twin}	
	Grain size independent models	
Narita & Takamura [130]	$\tau_{Twin} = \frac{\gamma_{isf}^{exp}}{2b_p}$	(6.1)

Byun [128]	$\tau_{Twin} = \frac{2\gamma_{isf}^{exp}}{b_p}$	(6.2)
	Grain size dependent models	
Gutierrez-Urrutia et al. [134]	$\tau_{Twin} = \frac{\gamma_{isf}^{exp}}{b_p} + \frac{\mu b_p}{D}$	(6.3)
Meyers et al. [133]	$\tau_{Twin} = \frac{\gamma_{isf}^{exp}}{b_p} + \frac{K_{Twin}^{HP}}{\sqrt{D}}$	(6.4)

Saka et al. and Lee & Choi pointed out previously that experimentally determined SFE values should be considered “apparent” as they may be affected by other factors than chemical composition [104,105,201]. Müllner & Ferreira [247] ascribed the differences between experimentally determined and intrinsic (as modelled based on composition) SFE values to strain energy from a difference in specific volume between *fcc* and the double-layer *hcp, a*ccounting to 1–4 mJ·m^{-2}. However, results by Pierce et al. [170] show that strain energy alone cannot account for the observed discrepancy. Also Sun et al. [206] observed that the strain energy contribution is negligible compared to the observed discrepancies and suggested that these originate from a frictional force experienced by moving Shockley partial dislocations, thereby effectively altering the force balance over the stacking fault during its formation. Molecular dynamics simulations by Shih et al. [228] confirmed that solute-dislocation interactions result in a frictional force that is contained in experimental SFE values but is not accounted for in SFE values determined by applying Density Functional Theory (DFT).

We recently demonstrated for metastable *fcc* alloys, that satisfactory consistency is obtained between theoretical intrinsic and experimentally determined SFE

values after proper correction [248]. *Experimental* SFE values do not represent an intrinsic materials property, as presupposed by the models in Table 1; the established theories thus need re-evaluation. In the present communication, it is postulated that the difference between experimental SFE values, γ_{isf}^{exp}, and SFE values predicted with DFT, γ_{isf}^{DFT}, is proportional to τ_{Twin}. Accordingly, the resistance experienced by moving Shockley partials that is omitted in a theoretical evaluation, is pragmatically accounted for.

6.3 Methodology

SFE values for *fcc* metals and $Cu_{100-x}Al_x$ binary alloys were calculated at room temperature with DFT [249,250] using the coherent potential approximation [181,182] as implemented in the exact muffin-tin orbitals package [182,251]. The *fcc* lattice was modelled using nine (111) layers containing one atom each and stacked in the standard sequence *ABCABCABC*. The lattice vectors of the *fcc* cell were $a_1 = a_0\langle 101\rangle/2$, $a_2 = a_0\langle 011\rangle/2$ and $a_3 = a_0\sqrt{3}\langle 111\rangle/3$, where a_0 is the *fcc* lattice parameter. Shifting a_3 by $a_0\langle 11\bar{2}\rangle/6$ introduced an intrinsic stacking fault via the periodic boundary condition, resulting in the new stacking sequence *ABCABCABC* | *BCABC …* [189]. The interplanar distance at the stacking fault interface was relaxed along a_3. The stacking fault energy was obtained by:

$$\gamma_{isf}^{DFT} = \left(F_{SF} - F_{fcc}\right)/A \tag{6.5}$$

where F_{fcc} and F_{SF} are the Helmholtz energies of the supercells before and after introducing an SF of area *A*. The Helmholtz energies at room temperature were approximated by the total energies from first-principles calculations for atomic volumes derived from the experimental lattice parameters at room temperature.

Unit cell volumes of the $Cu_{100-x}Al_x$ binary alloys were determined using Végard's law [252]. For Ni, spin-polarized calculations were performed [253]. The exchange-correlation functional was approximated using the Perdew, Burke, and Ernzerhof generalized gradient approximation [254]. The resolution of the k-point mesh was tested for energy convergence and consisted of 10556 uniformly distributed points with an error of < 0.1 mJ·m^{-2} in SFE. DFT does not account for the strain fields associated with the Shockley partials.

6.4 Results and Discussion

SFE values for pure Ag, Au, Cu, Al, and Ni at 293 K as calculated with DFT (γ_{isf}^{DFT}) are given in Table 6.2 and are compared to calculated values reported in literature [169,193,255–258]. Only for Ni, a significant variation is observed among the calculated values, depending on how (well) ferromagnetism is accounted for.

Table 6.2: DFT calculated SFE values for pure Ag, Au, Cu, Al and Ni in comparison with calculated literature values [169,193,255–258].

Reference	$\boldsymbol{\gamma_{isf}^{DFT}}$ mJ·m^{-2}				
	Ag	**Au**	**Cu**	**Al**	**Ni**
This work	25.0	40.0	48.8	116.5	155.7
Li et al. [255]	17.3	32.7	47.5	117.5	153.6
Zhang et al. [193]	-	-	38	110	110
Li et al. [169]	17	31	47	107	153
Kibey et al. [256]	18	33	41	130	110
Liu et al. [257]	-	-	38	134	120
Jin et al. [258]	16	25	36	112	133

Mean value	18.7 ± 3.6	32.3 ± 5.4	42.3 ± 5.3	118.1 ± 10.2	133.6 ± 20.7

Figure 6.1 shows that experimentally determined SFE values, (γ_{isf}^{exp}) [151,153,231,244–246,259–274] are systematically higher than DFT predicted values, with exception of the values determined by WBDF imaging for Cu [153] and Ni [231]. In these cases, good agreement is observed, despite the dependence of γ_{isf}^{exp} values derived from WBDF images on the description of the dislocation core [153]. In particular for high-SFE materials such as Cu and Ni, where the separation distance between the two Shockley partial dislocations is small, SFE values derived from WBDF images are subject to systematic errors [153,155,275,276]. The results in Figure 6.1 suggest that the applicability of WBDF imaging for SFE determination, is sensitive to the materials SFE itself.

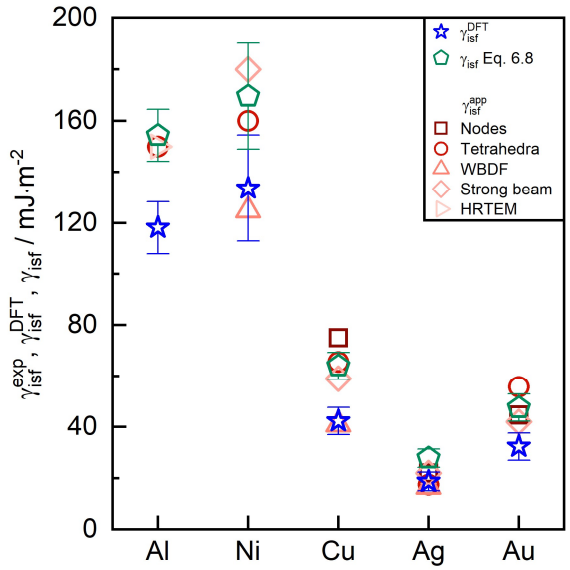

Figure 6.1: Experimental SFE values, γ_{isf}^{exp} averaged over the respective techniques for pure Ag [151,153,245,259–262,271–274], Au [244,245,260,274] Cu [153,245,260,263,264,274,277], Al [246,274], Ni [245,269,270], in comparison with the mean DFT based SFE values [169,193,255–258], γ_{isf}^{DFT}, and the SFE values, γ_{isf}, calculated according to Eq. (6.8). Presentation in order of atomic number.

The difference between DFT and experimental SFE values was previously addressed for *metastable fcc* materials and ascribed to an incomplete definition of the force balance over a SF, as it assumes that Shockley partial dislocations can move freely in their glide plane [206,227,248]. The results presented in Figure 6.1 suggest that the incomplete definition of the force balance also applies for *stable fcc* materials.

Experimental SFE values, γ_{isf}^{exp}, for a series of Cu-Al alloys are collected in Figure 6.2a. For the compositional range considered, the alloy stability ranges from *stable* to *metastable*. Up to approximately 8 at.% Al, γ_{isf}^{exp} decreases almost linearly with Al-content and, eventually, asymptotically approaches 5 mJ·m^{-2}. For relatively low Al-contents, SFE values from WBDF are systematically lower than experimental SFE values from other techniques, analogous to pure metals. For higher Al-contents, experimental SFE values determined with WBDF coincide with SFE values determined from SF nodes and tetrahedra.

The critical resolved shear stress for twinning, τ_{Twin}, was calculated in dependence of the Al-content with the models in Eq. (6.1) and Eq. (6.2) and is compared with experimental values from Refs. [278–281] in Figure 2b[3]. Neither Eq. (6.1) nor Eq.

[3] Note that the reported values for τ_{Twin} in Fig. 7.2b differ from the values reported by Venables (cf. Table 1 in Ref. [278]) due to the following reasons. At first, Venables established the observation of twins in TEM micrographs as a criterion to determine the twinning stress and calculated τ_{Twin} as the average of the lowest stress at which twins could be observed and the highest stress at which twins were still absent. For the Cu-Al alloy with 4,7 at. % Venables calculated τ_{Twin} as the average of data point showing small amounts of twins and twinning with load drops, whereas for alloys with 8.9 and 14.9 at. % Al Venables calculated τ_{Twin} as the average stress of the lowest stress at which stacking faults could be observed and the highest stress at which no stacking faults were observed. However, Tian et al. [280] have shown that in a Cu-15Al alloy stacking faults could already be observed at a plastic strain of 2 %, while twins were first discernable in TEM micrographs at significantly higher strains/stresses. This illustrates that at least in the case of Cu-Al alloys of low SFE, the twinning stress should not be determined based on the observation of stacking faults. Instead, as done in this work, the actual necessary shear stress for the formation of twins should be approximated by taking the mean value of the lowest stress values in Figure 3 in Ref. [278] for which twinning is observed. Accordingly determined twinning stresses coincide with results from Szczerba & Szczerba [279] and Mori et al. [281] (cf. Figure 3).

(6.2) can accurately describe the dependence of experimental τ_{Twin} data on Al-content, indicating that γ_{isf}^{exp} alone is insufficient to describe the critical resolved shear stress for twinning τ_{Twin}.

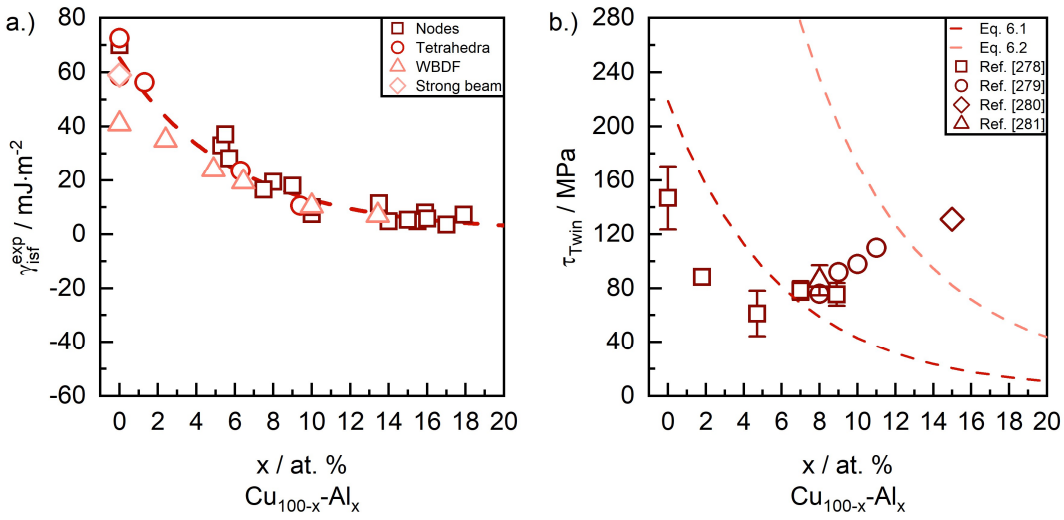

Figure 6.2: a.) Experimental SFE values as a function of the Al-content in Cu-Al alloys determined from nodes [264,265,277,282–285], tetrahedra [244,260,274], WBDF [152,231] and strong beam [245] imaging, b.) Experimental critical resolved shear stresses for twinning [278–281] compared with τ_{Twin} predicted by the models by Narita & Takamura (Eq. (6.1)) and Byun (Eq. (6.2)). Note that the experimental τ_{Twin} values are, apart from the value by Tian et al. [280], determined on single crystalline alloys.

As recently demonstrated, experimentally determined SFE values consist of a material's intrinsic SFE, γ_{isf}, and an excess term, γ^*, which accounts for the resistance experienced by moving Shockley partials in their common glide plane [248]:

$$\gamma_{isf}^{exp} = \gamma_{isf} + \gamma^* \tag{6.6}$$

γ^* was previously introduced by Sun et al. [206] to represent the discrepancy between the SFE determined by DFT, γ_{isf}^{DFT}, and γ_{isf}^{exp}, suggesting that γ_{isf} directly corresponds to γ_{isf}^{DFT} within computational accuracy. Including γ^* in the energy

balance over a SF reconciles experimental SFE values, γ_{isf}^{exp}, for *metastable* alloys with negative SFE values from DFT [248]. Recognizing that a Shockley partial in *fcc* is equivalent to a coherent twin boundary, the resistance experienced by moving Shockley partial dislocations was pragmatically postulated to be proportional to the critical resolved shear stress for twinning, τ_{Twin} [248]:

$$\gamma^* = b_p \tau_{Twin} \tag{6.7}$$

with b_p the length of the Burgers vector of the partial dislocations. Rearranging Eqs. (6.6 and (6.7, τ_{Twin} relates to the SFE as:

$$\tau_{Twin} = \frac{\gamma^*}{b_p} = \frac{\gamma_{isf}^{exp} - \gamma_{isf}}{b_p} \tag{6.8}$$

Evidently, instead of proportional to γ_{isf}^{exp} as in Eqs. (6.1–(6.4 in Table 6.1, it is argued that τ_{Twin} is proportional to the excess term γ^*, which also accounts for grain size dependence [19]. Experimental SFE values of Cu-Al alloys (Figure 6.2a) are compared with DFT values in Figure 6.3a. Instead of the asymptotic approach to 5 mJ.m^{-2} observed for the experimental values, DFT predicts a continuous reduction in SFE with Al-content, from a positive to a negative value, in agreement with Ref. [169]. Accordingly, the observed asymptotic behavior of γ_{isf}^{exp} is interpreted as caused by the bias that experimental SFE values are always positive, owing to an incomplete definition of the energy balance over a SF [206,227,248]. Applying Eq. (6.8) and assuming $\gamma_{isf} = \gamma_{isf}^{DFT}$, the difference between the fitted (dashed) lines, as marked by the shaded area in Figure 6.3a, divided by the Burgers vector $b_p = 0.149\ \mathrm{nm}$ yields τ_{Twin} in dependence of Al-content. The critical resolved shear stress for twinning calculated with Eq. (6.8) is compared with experimental data for the twinning shear stress in Figure 6.3b.

Evidently, the calculated values for τ_{Twin} describe the dependence of independent experimental values for τ_{Twin} on Al-content with unprecedented quantitative accuracy. The systematic underestimate of τ_{Twin} could be as a result of a slight overestimation of γ_{isf}^{DFT} in this work. In this respect, it is noted that γ_{isf}^{DFT} values for Cu-Al alloys reported by Li et al. [169] are systematically 3-5 mJ·m^{-2} lower, which corresponds, according to Eq. (6.8), to a difference of 20-30 MPa in the twinning stress. The calculated γ_{isf}^{DFT} values in Figure 6.3a provide an explanation as to why Eq. (6.1) provides reasonable τ_{Twin} values for Al-contents in the range 8-10 at.% (see Figure 6.2b). For $\gamma_{isf} \approx 0$ mJ·m^{-2}, the experimental SFE value γ_{isf}^{exp} becomes equal to γ^* (see Eq. (6.7)). Accordingly, for materials with a small, positive or negative γ_{isf} it may appear that τ_{Twin} correlates with γ_{isf}^{exp}.

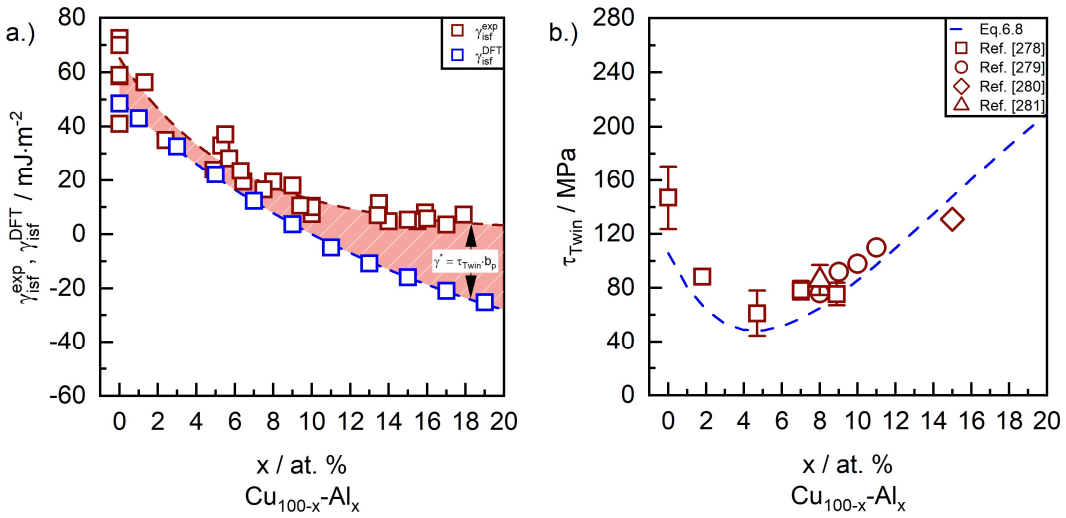

Figure 6.3: a.) Experimental SFE values (γ_{isf}^{exp}) [152,231,244,245,260,264,265,274,277,282–285], and SFE values predicted by DFT (γ_{isf}^{DFT}) as a function of the Al-content in Cu-Al alloys, b.) Experimentally determined critical resolved shear stresses for twinning [278–281] and the predicted trend of τ_{Twin} in Cu-Al alloys according to Eq. (6.8). Note that the experimental τ_{Twin} values are, apart from the value by Tian et al. [280], determined on single crystalline alloys.

The trends in Figure 6.3b are confirmed by the results of Tranchant et al. [286], who reported that the dependence of τ_{Twin} on Al-content can be divided into two subranges: i) for $\gamma_{isf}^{exp} > 17$ mJ·m^{-2}, i.e. < 9 at. % Al, τ_{Twin} decreases with decreasing γ_{isf}^{exp}; ii) for $\gamma_{isf}^{exp} > 17$ mJ·m^{-2}, i.e. > 9 at. % Al, τ_{Twin} increases with decreasing SFE. The non-monotonic dependence of τ_{Twin} on γ_{isf}^{exp} is explained from the transition from nucleation-controlled twinning for $\gamma_{isf}^{exp} > 17$ mJ·m^{-2} to propagation controlled twinning for $\gamma_{isf}^{exp} < 17$ mJ·m^{-2}. Twinning controlled by nucleation and growth/propagation is consistent with the current opinion on deformation twinning [133,287]. In the Cu-Al system the transition coincides with a change from positive to negative γ_{isf}^{DFT} values, i.e. transition from *stable* to *metastable fcc*. From a thermodynamics point of view the transition is logical. For a positive SFE, additional driving force by mechanical work must be introduced to nucleate twins in the *stable fcc* matrix. Once formed, these twins can easily extend by the propagation of Shockley partial dislocations. For negative SFE, the nucleation of SFs and twins in the *metastable fcc* matrix is thermodynamically favorable. Nevertheless, twins and wide SFs are first observed above τ_{Twin}, indicating that the propagation of Shockley partial dislocations is hindered. If twinning or SF formation would be nucleation-controlled, *metastable fcc* materials would readily twin or transform into martensite and thus be *unstable*, which, inherent to their *metastability*, is not observed.

In Figure 6.4, Eq. (6.8) is applied to various *stable* and *metastable fcc* alloys to test general applicability. Convincingly, a linear relationship between τ_{Twin} and excess SFE γ^* is obtained over a wide range of τ_{Twin} values, consistent with Eq. (6.8). Li et al. [288] previously observed that the established models in Table 6.1 cannot be

used to predict the trend of τ_{Twin} for *fcc* medium- (MEAs) and high-entropy alloys (HEAs). Notably, Eq. (6.8) consistently predicts that τ_{Twin} decreases in the order CoCrNi, CoCrFeNi to CoCrFeMnNi with increasing γ_{isf}^{exp}, whilst Eqs. (6.1)–(6.4) predict the opposite order.

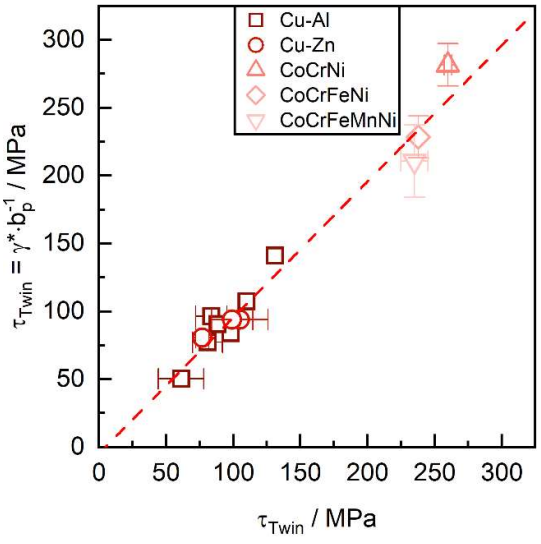

Figure 6.4: Twinning stress values calculated according to Eq. (6.8) from apparent SFE values and SFE values predicted by DFT for Cu-Al (inferred from Fig. 3a), Cu-Zn [169,277], CoCrNi [154,206,238], CoCrFeNi [113,206,238] and CoCrFeMnNi [206,238,239] alloys as a function of the experimental twinning stress (τ_{Twin}) Cu-Al [278–281], Cu-Zn [289,290], CoCrNi [154], CoCrFeNi [113] and CoCrFeMnNi [120].

In the presented framework, Eq. (6.8) enables calculation of the twinning stress from γ^* which requires that values for $\gamma_{\mathrm{isf}}^{\mathrm{exp}}$ and $\gamma_{\mathrm{isf}}^{\mathrm{DFT}}$ are available. Alternatively, the experimental SFE value can be calculated if τ_{Twin} and $\gamma_{\mathrm{isf}}^{\mathrm{DFT}}$ are known. Thus, based on the average $\gamma_{\mathrm{isf}}^{\mathrm{DFT}}$ values in Table 6.1 and the twinning stress values in Table 6.3, the “experimental” SFE values of pure metals were calculated with Eq. (6.8) and are given in Table 6.3. These predicted SFE values are also given in Figure 6.1 and are in excellent agreement with the average experimentally

determined $\gamma_{\mathrm{isf}}^{\mathrm{exp}}$ data. The consistency between predicted and experimental $\gamma_{\mathrm{isf}}^{\mathrm{exp}}$ values strongly supports the applicability of the postulate formulated in Eq. (6.8).

Table 6.3: Twinning stress τ_{Twin} of pure Ag, Au, Cu, Al and Ni together with apparent experimental SFE values predicted based on the average Daft values in Table 6.1 according to Eq. (6.8).

	Metal				
	Ag	**Au**	**Cu**	**Al**	**Ni**
τ_{Twin} [MPa]	54.5 ± 16.5 [131]	92.5 ± 7.5 [131]	147 ± 23.5 [278]	220 [256]	250 [256]
γ_{isf}^{exp} [mJ $\cdot$ m^{-2}]	27.8 ± 3.6	47.6 ± 5.4	64.0 ± 5.3	154.4 ± 10.2	169.6± 20.7

Finally, for most alloy systems, γ_{isf}^{exp} is reported to be temperature-dependent and decreases with decreasing temperature [108,191]. Consequently, Eqs. (6.1)–(6.4) would predict that τ_{Twin} decreases with decreasing temperature [119], which is in disagreement with experimental observations of a nearly temperature-independent τ_{Twin} [119,120,130,131,133,154]. Neding et al. [190] demonstrated that γ_{isf}^{exp} and γ_{isf}^{DFT} have the same temperature dependence within experimental and computational accuracy. Hence, the difference between experimental and theoretical SFE values, γ^*, is in this case constant. Thus, τ_{Twin} calculated according to Eq. (6.8) is temperature independent, in agreement with experimental observations.

Recently, a systematic discrepancy of ≈42 mJ·m^{-2} ($\gamma_{isf}^{exp} = 35 \pm 7$ mJ·m^{-2} and $\gamma_{isf}^{DFT} = -7$ mJ·m^{-2}) was reported between the experimental and DFT assessed SFE values for the equiatomic CrMnFeCoNi HEA [156]. Applying Eq. (6.8), using $\tau_{Twin} = 235 \pm 20$ MPa [120] and $b_p = 1.47$ nm [156], shows that $\gamma^* \approx 35 \pm 2$

mJ·m^{-2}. Following the sum rule of uncertainties, Eq. (6.8) yields $\gamma_{isf} = 0 \pm 9$ mJ·m^{-2}, exemplifying that experimental and DFT assessed SFE values can be reconciled within experimental and computational accuracy. Further improvement of the agreement between experimental and theoretical SFE values could be achieved if, as suggested by Wagner et al. [156] (i) vibrational, electronic, and magnetic excitations; (ii) atomic relaxations, were included in the calculations. Nevertheless, the discrepancy between experimental and theoretical SFE values appears to be largely bridged by the resistance experienced by moving Shockley partial dislocations $\gamma^* = b_p \tau_{Twin}$.

6.5 Conclusions

The discrepancy between DFT and experimental SFE values for pure metals as well as *stable* and *metastable fcc* alloys is reconciled by accounting for the critical resolved shear stress for twinning:

$$\gamma_{isf}^{exp} = \gamma_{isf}^{DFT} + b_p \tau_{Twin}$$

The equation expresses that experimentally determined SFE values are not an intrinsic materials property but depend on the path followed to introduce the stacking fault before observation. This path involves the movement of partial dislocations under the influence of a resolved shear stress and adds to the thermodynamically defined intrinsic stacking fault energy as calculated with DFT.

Applying the postulated equation to calculate the twinning stress for *fcc* metals as well as for stable and metastable *fcc* alloy systems from experimental and DFT SFE values, unprecedented quantitative agreement with experimentally determined twinning stresses is obtained. Furthermore, the calculated twinning

stress is independent of temperature, consistent with experimental twinning stresses.

6.6 Declaration of Competing Interest

The authors declare that they have no known competing financial interests or personal relationships that could have appeared to influence the work reported in this paper.

6.7 Acknowledgements

This work was supported by the Independent Research Fund Denmark as part of the project SFETailor (Grant No. 9041-00145B). The authors would like to thank Francesco Maresca (University of Groningen) for the valuable scientific discussions.

7 Manuscript III:

Experimental and computational assessment of the temperature dependency of the stacking fault energy in face-centered cubic high-entropy alloy

Konstantin V. Werner[1]*, Muhammad Naeem[2*], Frank Niessen[1], Li Zhu[2], Matteo Villa[1], Xun-Li Wang[2], Marcel A. J. Somers[1],

*Corresponding authors. E-mail address: kviwe@mek.dtu.dk, mnaeem2@cityu.edu.hk

[1]Department of Civil and Mechanical Engineering, Technical University of Denmark, Produktionstorvet, Building 425, 2800 Kongens Lyngby, Denmark

[2] Department of Physics and Center for Neutron Scattering, City University of Hong Kong, Kowloon, Hong Kong

7.1 Abstract

The stacking fault energy and deformation mechanisms in face-centered cubic materials are considered closely related. Experimentally determined stacking fault energy values are exclusively positive. However, recent results obtained by first principle methods predict that the intrinsic stacking fault energy of metastable face-centered cubic is negative. This implies that deformation twinning and martensite formation, which rely on the formation of stacking faults, are not only influenced by the SFE, but also depend on the resolved shear stress for Shockley partial dislocations. It was previously shown that SFE values from first principle methods and experiments can be reconciled, when taking the resolved shear stress for

Shockley partial dislocations into account. Nevertheless, the determination of the resolved shear stress for Shockley partial dislocations is experimentally challenging and reconciling experimental and theoretical SFE values is thus laborious. In the present communication, the possibility to determine the critical resolved shear stress for Shockley partial dislocations based on in-situ neutron diffraction experiments is evaluated. The determined values enable the reconciliation of experimental and theoretical SFE values based on a single experiment. Accordingly, the experimental effort to validate stacking fault energies from first principle methods is reduced significantly.

Keywords: Stacking fault energy, Twinning, Density functional theory, Deformation mode

7.2 Introduction

High- and medium-entropy alloys, HEAs and MEAs, respectively, have attracted considerable research interest due to their promising combination of strength and ductility, even at cryogenic temperatures [154,291–294]. The high intrinsic strength of HEAs and MEAs results from an increase in average atomic misfit and associated lattice strains of the 3rd kind, as compared to traditional structural materials such as e.g. steels [81,295], and is not, as initially thought, related to a relatively high configurational entropy [291,296]. In contrast, the high ductility of HEAs and MEAs is associated with twinning induced plasticity (TWIP) and transformation induced plasticity (TRIP) effects [120,293,297], which provide more pronounced work hardening than pure dislocation slip and therefore delay the occurrence of necking. The reason for the increase in the work hardening rate associated with the TWIP and TRIP effect is considered to be the continuous refinement of the microstructure due to the formation of twin boundaries and

martensite/austenite phase boundaries, which constitute obstacles for dislocation movement by the dynamic Hall-Petch effect [118,298].

Whether a material deforms by a combination of dislocation slip and TRIP/TWIP or by dislocation slip alone is thought to be governed by the stacking fault energy (SFE) [23,24]. The SFE is the energy associated with the presence of a stacking fault (SF) that forms in a face-centered cubic (*fcc*) matrix and is terminated by a pair of Shockley partial dislocations. Thermodynamically, the SFE is considered to be a two-atomic layer thick high ε–martensite embryo [235]. Experimentally, stacking faults are created by plastic deformation. According to the current paradigm, low experimental SFE values (<20 $mJ \cdot m^{-2}$) favor TRIP, while intermediate SFE values (20 – 40 $mJ \cdot m^{-2}$) lead to TWIP and materials with even higher SFE values deform exclusively by dislocation slip (>40 $mJ \cdot m^{-2}$) [24,299]. The SFE is commonly considered an intrinsic materials property, irrespective of whether it is experimental or thermodynamic, and depends on chemical composition, temperature and pressure [39,187,188,196]. Within this paradigm, a material's mechanical properties, and hence the combination of prevalent deformation mechanisms, can be tailored by adjusting its SFE.

Recent advances in first principle calculations challenge the assumption that plastic deformation of *fcc* metals and alloys is governed alone by their respective intrinsic SFE [256,300]. Instead, it appears that plastic deformation and the prevalence of certain deformation mechanisms is governed by the generalized stacking fault energy surface (GSFE) [256,300]. Furthermore, theoretical (thermodynamic) SFE values determined by applying density functional theory (DFT) are systematically lower than SFE values determined by experiments. Moreover, thermodynamic SFE values become negative for metastable materials,

which is incommensurate with experimental SFE values, which are positive by definition [206,227,248,301]. Wei & Tasan [227] as well as Sun et al. [206] suggested that the experimental SFE determination neglects the resistance against the movement of Shockley partial dislocations, which would alter the force balance acting on the Shockley partials. Molecular dynamics simulations by Shih et al. [228] confirmed that the solute drag experienced by Shockley partial dislocations has an effect on the stacking fault width and, therefore, on the experimentally determined SFE. Recently, it was demonstrated by Werner et al. [248,301] that the systematic gap between theoretical and experimental SFE values can be bridged by considering the resistance against the movement of Shockley partials (τ_{CRSS}^{P}) in the force balance over a stacking fault. Pragmatically, this resistance was postulated to be proportional to the critical resolved shear stress (CRSS) for twinning (τ_{CRSS}^{Twin}). This approach yielded unprecedented quantitative agreement between theoretical and experimental SFE values for stable as well as metastable *fcc* materials (including HEAs and MEAs). However, this puts forward the following question: How can τ_{CRSS}^{P} be assessed reliably for a vast compositional space as constituted by HEAs and MEAs?

Transmission electron microscopy (TEM) is commonly used to determine τ_{CRSS}^{Twin} from the onset of deformation. The latter is applied ex-situ or in-situ [120,154]. The experimental work associated with determining τ_{CRSS}^{Twin} after ex-situ loading is laborious and the accuracy of the determined values for τ_{CRSS}^{Twin} is directly related to the chosen stress/strain intervals. On the other hand, in-situ TEM provides the opportunity to observe the motion of isolated Shockley partial dislocations and therefore the determination of $\tau_{CRSS}^{Twin}/\tau_{CRSS}^{P}$. However, investigating a vast compositional space with in-situ TEM is certainly not possible and findings indicate

that the mechanical behavior of a thin foil cannot be translated easily to that of a bulk material [302]. Wang et al. [113] pointed out an alternative path to determine τ_{CRSS}^{P} by probing the stacking fault probability (SFP) in-situ with X-ray or neutron diffraction during plastic deformation and infer τ_{CRSS}^{p} from the relation between SFP and true stress.

In this work, the experimental assessment of the temperature dependency of the SFE for FeCoCrNi is coupled with first principles calculations and the prevalent deformation mechanism. Furthermore, the proposal by Wang et al. [113] to determine the critical resolved shear stress for Shockley partials from SFP vs. true stress curves is explored in an attempt to bridge the gap between negative SFE values from DFT and positive SFE values from experiments.

7.3 Experimental methods

7.3.1 Material

The FeCoCrNi samples were prepared from pure metals by arc-melting. To ensure chemical homogeneity, the materials were re-melted several times and subsequently cast into Cu-molds. Homogenization was performed in an argon atmosphere for 24 h at 1200 °C with subsequent quenching into water. The samples were cold-rolled up to a thickness reduction of ~80% and afterwards annealed at 800 °C for 1 h to achieve full recrystallization, which resulted in an average grain size of approximately ~5 µm. Tensile specimens with gauge dimensions of 25 mm × 4 mm × 3 mm were machined by wire electrical discharge machining from the as-recrystallized material.

7.3.2 Neutron diffraction and analysis of diffraction data

The in-situ neutron diffraction experiments were performed at the TAKUMI Engineering Materials Diffractometer, beamline-19 of the Materials and Life Science Experimental Facility at the Japan Proton Accelerator Research Complex. Low-temperature experiments were carried out with the cryogenic loading machine [303]. The tensile direction was inclined 45° relative to the incident neutron beam. Accordingly, diffractograms were acquired with scattering vectors parallel to and normal to the tensile direction on the two detector banks, which are installed at –90 ° and +90 ° with respect to the incident neutron beam, respectively. Thus, during the in-situ tensile tests data was acquired both along the loading and in the transverse direction. Temperatures were monitored with a Chromel/AuFe0.07% thermocouple that was attached to the samples. Prior to loading, the samples were held for ∼1 h at low temperatures (25 K, 40 K and 140 K). Tensile loading experiments were carried out at a strain rate of 2.67×10^{-5} s $^{-1}$.

Rietveld refinement of the diffractograms was performed with the Z-Rietveld software [304]. The strain for individual lattice planes ε_{hkl} was obtained from:

$$\varepsilon_{hkl} = \frac{(d_{hkl} - d^0_{hkl})}{d^0_{hkl}} \tag{7.1}$$

where d_{hkl} is the lattice spacing of the *{hkl}* family of lattice planes upon loading and d^0_{hkl} is the strain-free lattice spacing. The SFP was determined based on Warren's method [161]:

$$SFP = \frac{32\pi}{3\sqrt{3}}(\varepsilon_{222} - \varepsilon_{111}) \tag{7.2}$$

with ε_{111} and ε_{222} the lattice strains for $\{111\}$ and $\{222\}$, respectively.

7.3.3 Materials characterization

The microstructure of the as fractured specimens was investigated with TEM on a JEOL JEM-2100F transmission electron microscope. TEM samples were prepared by focused ion beam (FIB) milling, using an FEI Scios DualBeam SEM/FIB system. To prevent beam damage the FIB lamellae were capped with a protective platinum (Pt) deposit. Gallium (Ga^+) ion beams of 30 kV per 5 nA and 30 kV per 0.1 nA were used for sample-cutting and early-stage milling, respectively. Finally, Ga^+-ion beams of 16 kV per 23 pA and 2 kV per 4.3 pA were employed to achieve the final milling and to minimize any amorphous and damaged layers.

7.3.4 Computational methods

The SFE values for the FeCoCrNi alloy at the four test temperatures were calculated using Density Functional Theory (DFT) modeling and the Coherent Potential Approximation (CPA) [181,182] as implemented in the exact muffin-tin orbitals (EMTO) package [182,251]. The *fcc* lattice was modelled for a stack of nine (111) planes consisting of one atom each and stacked in the standard sequence *ABCABCABC*. The lattice vectors of the *fcc* cell were $a_1 = a_0\langle 101\rangle / 2, a_2 = a_0\langle 011\rangle / 2$ and $a_3 = a_0\sqrt{3}\langle 111\rangle / 3$, with a_0 the *fcc* lattice parameter. Shifting a_3 by $a_0\langle 11\bar{2}\rangle/6$ introduced an intrinsic stacking fault via the periodic boundary condition to produce the new stacking sequence *ABCABCABC* | *BCABC* …. The stacking fault energy was then obtained by:

$$\gamma_{isf}^{DFT} = \left(F_{SF} - F_{fcc}\right)/A \tag{7.3}$$

with F_{fcc} and F_{SF} the Helmholtz energies of the supercells before and after introducing an SF of area A. The Helmholtz energies consisted of the DFT total

energy and the magnetic entropy contribution as applied in Ref. [189]. First-principles calculations were conducted at the atomic volumes derived from the experimental lattice parameters at the test temperatures to partially account for the effect of a finite temperature. The exchange-correlation functional was approximated using the Perdew, Burke, and Ernzerhof (PBE) generalized gradient approximation [254]. The resolution of the k-point mesh was tested for energy convergence and consisted of 10556 uniformly distributed points with an error of < 0.1 $mJ \cdot m^{-2}$ in SFE.

7.4 Results

7.4.1 Mechanical properties

The mechanical properties of the FeCoCrNi HEA tested at four different temperatures were reported and evaluated elsewhere in detail [109]. Key mechanical parameters as well as the lattice parameter of the undeformed HEA are given in Table 7.1 for the four test temperatures.

Table 7.1: Mechanical properties of the FeCoCrNi alloy for the four test temperaturs 25 K, 40 K, 140 K, and 295 K. Yield strength (σ_y), ultimate tensile strength (σ_{UTS}), strain till failure $(\boldsymbol{\varepsilon_f})$, contribution of work hardening (θ), and the stress free lattice parameter (a_0) [109].

Temperature [K]	$\boldsymbol{\sigma_y}$ **[MPa]**	$\boldsymbol{\sigma_{UTS}}$ **[MPA]**	$\boldsymbol{\varepsilon_f}$ **[%]**	$\boldsymbol{\theta}$ **[MPa]**	$\boldsymbol{a_0}$ **[Å]**
295	331	1009	45.0	678	3.5723
140	502	1886	58.7	1384	3.5644
40	637	2377	58.9	1740	3.5637
25	676	2396	58.4	1720	3.5636

It is apparent that lowering the deformation temperature enhances the mechanical properties of the FeCoCrNi HEA significantly; yield strength (σ_y) and ultimate tensile strength (σ_{UTS}) increase by a factor of 2 and 2.4, respectively, upon lowering the deformation temperature from 295 K to 25 K. In addition, the strain to failure (ε_f) increases from 45.0 % at 295 K to 58.7 % at 140 K and remains unchanged at 40 K and 25 K. The observed improvement in mechanical properties of the FeCoCrNi HEA at cryogenic temperatures agrees with the correlation of deformation temperature and mechanical properties of HEAs reported in the literature [154,293]. Lowering the deformation temperature is considered to result in a drastically higher thermal contribution to the Peierls stress, hence rendering solid solution strengthening more potent at low temperatures [109]. Below room temperature, the Hall-Petch coefficient depends only weakly on temperature, such that its contribution is negligible as compared to the Peierls stress contribution [64]. The improved ductility of HEAs and MEAs at low temperatures is commonly attributed to a more pronounced contribution of the TWIP effect [305], which increases the work hardening rate as a result of the dynamic Hall-Petch effect [119,120].

7.4.2 Microstructural evolution upon plastic deformation

Diffractograms of the undeformed HEA and upon reaching the UTS for the four temperatures are given in Figure 7.1a–d. Prior to deformation the HEA is single-phase *fcc*, irrespective of temperature.

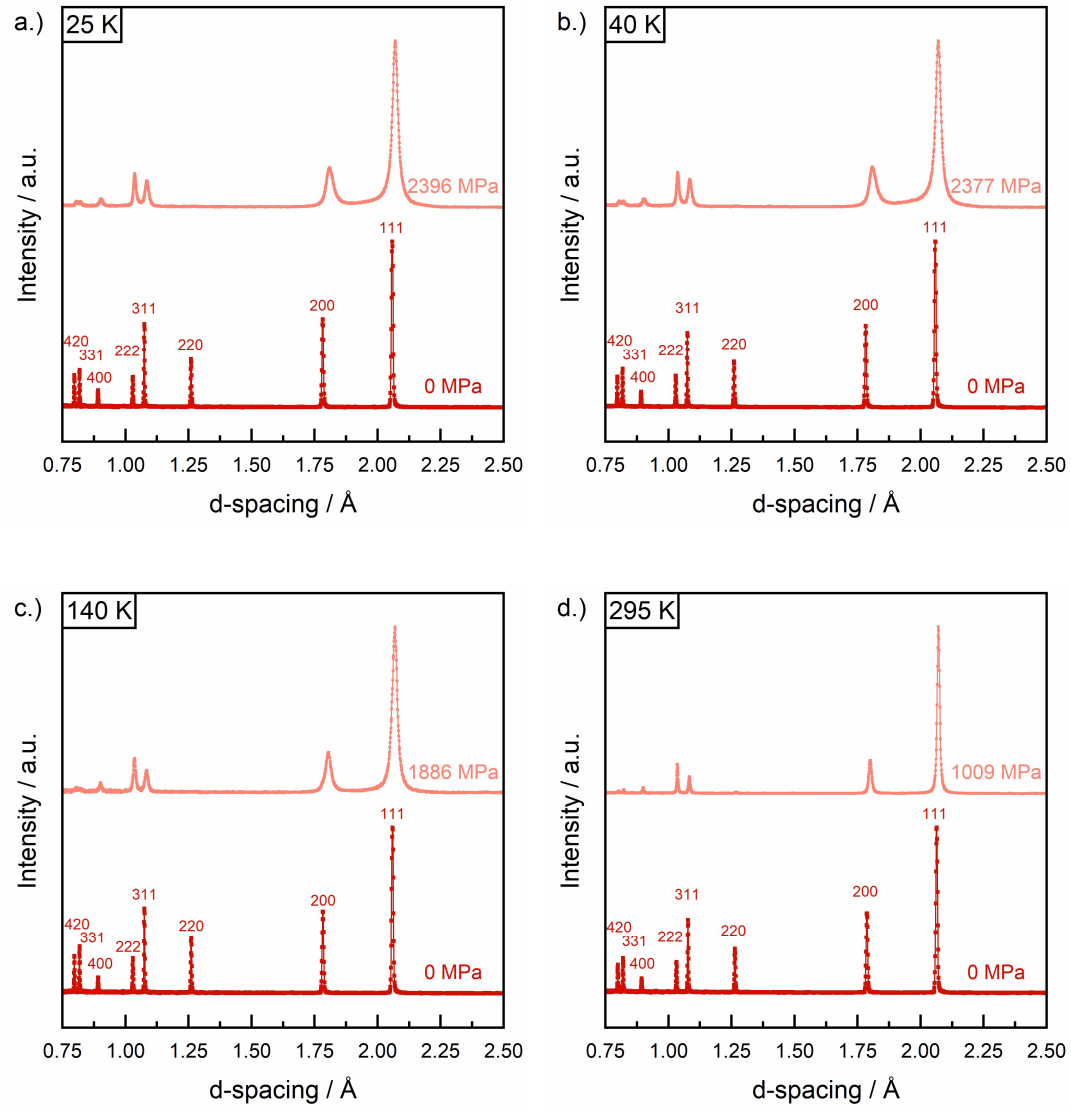

Figure 7.1: Normalized diffractograms of the FeCoCrNi HEA in the undeformed state, and upon reaching the ultimate tensile strength – a. 25 K, b. 40 K, c. 140 K and d. 295 K.

The diffractograms of the specimens upon reaching UTS do not reveal additional peaks, indicating that the *fcc* lattice of FeCoCrNi HEA is stable and does not transform martensitically upon deformation. This is in line with previous investigations that confirm the absence of deformation-induced martensite (DIM) in FeCoCrNi deformed at cryogenic temperatures [109,113]. The bright field images in Figure 7.2 confirm that FeCoCrNi does not form DIM at cryogenic

temperature, but forms deformation twins instead. In contrast to the findings by Wang et al. [113], the sample deformed at 295 K did not show signs of deformation twinning. It is reasoned that this absence is related to the smaller grain size of the FeCoCrNi HEA in this work as compared to the FeCoCrNi samples investigated by Wang et al. [113]. A smaller grain size has been demonstrated to reduce the propensity for, and eventually fully suppress, twinning [134,198,220–222], because the CRSS for twinning increases with decreasing grain size [134,306].

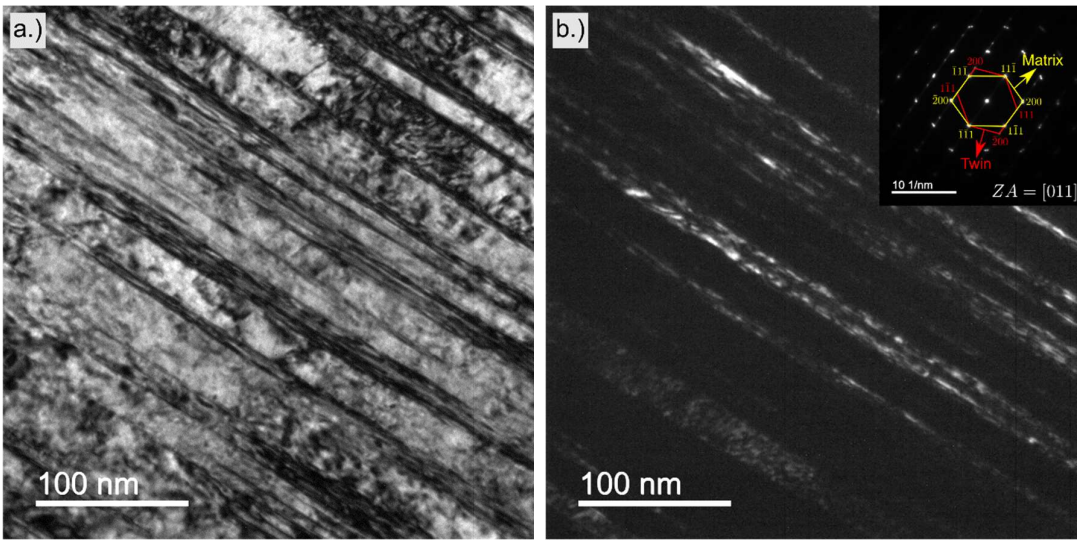

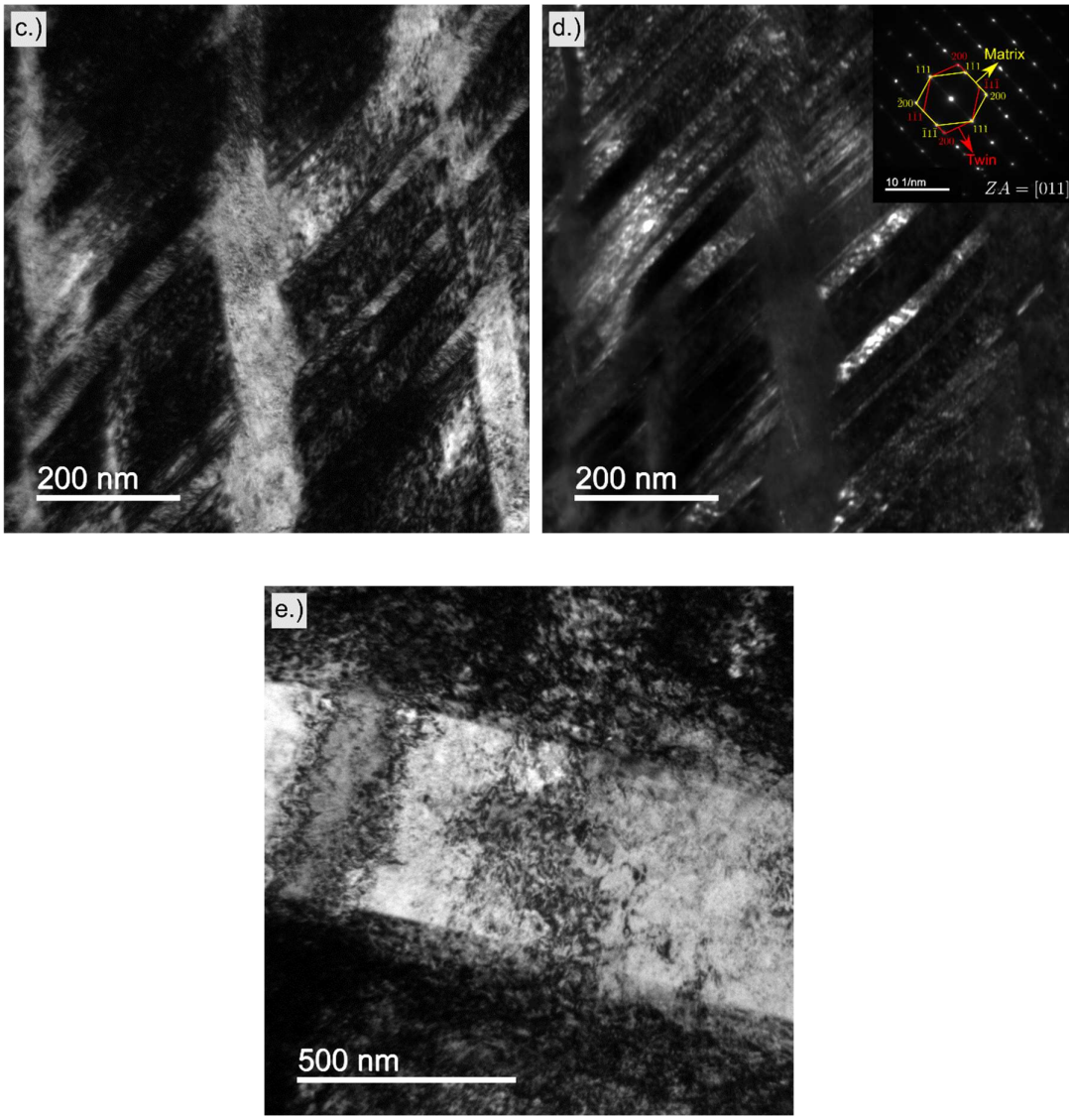

Figure 7.2: Bright field images obtained by transmission electron microscopy of the as-fractured FeCoCrNi HEA samples deformed at – a.) 25 K, c.) 140 K and e.) 295 K. As well as the respective dark field images and the corresponding selected area diffraction patterns deformed at – b.) 25 K and d.) 140 K.

7.4.3 Evolution of the stacking fault probability with true stress

The evolution of the stacking fault probability for the four test temperatures, determined according to Eqs. (7.1) and (7.2), is given in Figure 7.3 a– d as a function of the true stress. Comparing the SFP vs. true stress curves, reveals three

distinctive aspects: i) the achievable magnitude of the SFP is temperature dependent, such that a lower deformation temperature results in a higher SFP, ii) at first the SFP remains approximately zero, but starts to increase upon surpassing a threshold stress, iii) the rate of increase upon surpassing the threshold stress is temperature dependent.

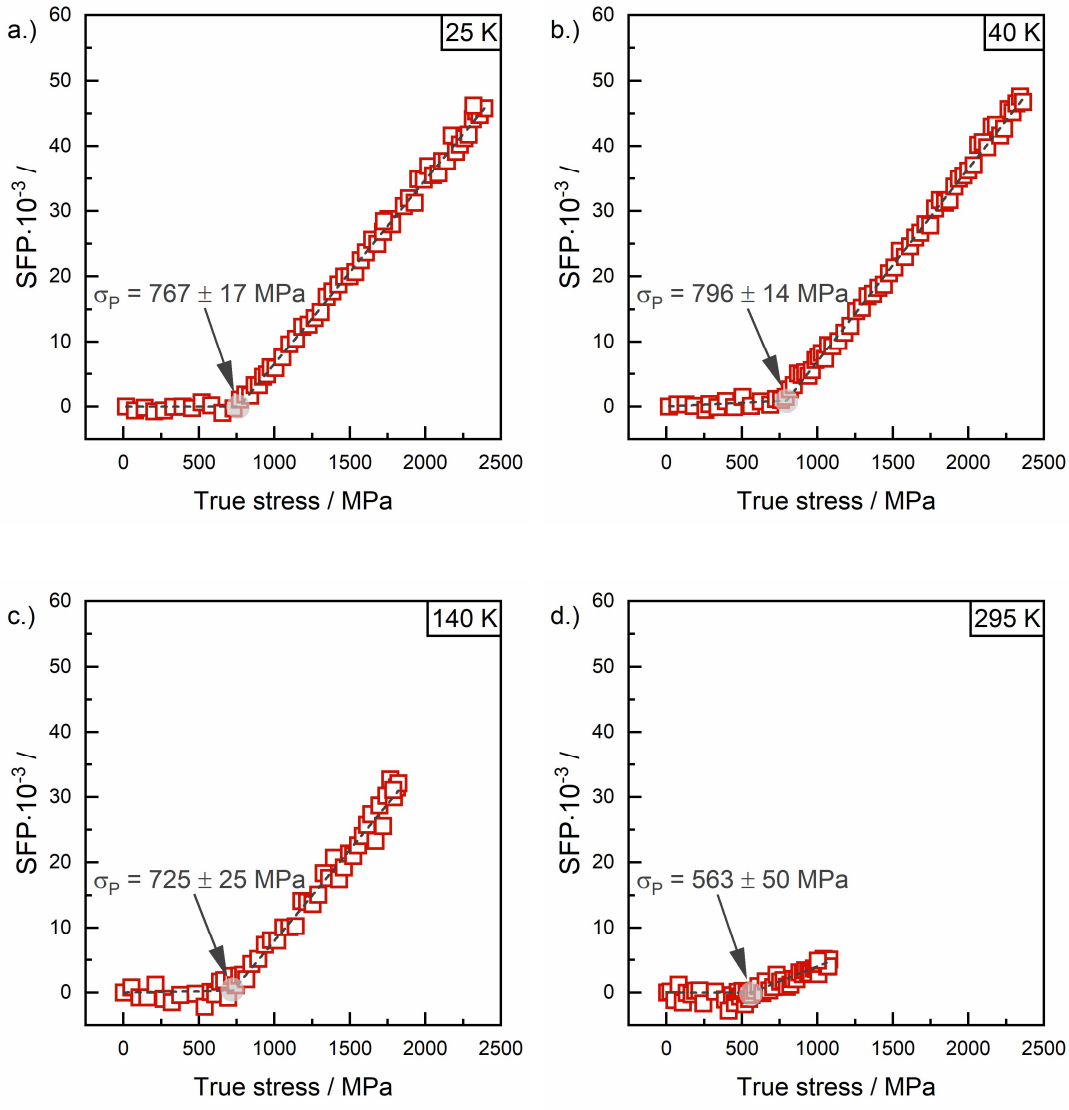

Figure 7.3: Stacking fault probability (SFP) determined according to Eq. (7.2) as a function of the true stress for the four different deformation temperatures – a.) 25 K, b.) 40 K, c.) 140 K and d.) 295 K.

In line with the trends reported in the literature [112,113,307], the SFP attained at fracture decreases with increasing temperature from approx. $45 \cdot 10^{-3}$ at 25 K and 40 K to $5 \cdot 10^{-3}$ at 295 K. Evidently, lowering the deformation temperature increases the ease of stacking fault and twin formation, as corroborated by TEM (cf. Figure 7.2) and thus increases their respective contribution to strain hardening [109,307]. Intriguingly, in the temperature range 25 K to 140 K the SFP increases at 0.028 MPa^{-1} with true stress at virtually the same rate, while at 295 K it is only one third of this rate: 0.009 MPa^{-1}. Certainly, this indicates that lowering the deformation temperature promotes SF formation. However, if the deformation temperature has a direct effect on SF-formation, the observed constant rate of SF-formation at cryogenic temperatures cannot be explained. Instead, the difference in the SFP's rate may be correlated with the effect of thermal activation on the movement of full and Shockley partial dislocations.

The threshold stress beyond which SFP increases was determined from Figure 7.3 and is taken as the critical stress for widening of the SFs (σ_P). The determined values for σ_P are compared with the yield stress σ_y in Figure 7.4. Clearly, the difference between σ_y and σ_P becomes smaller with decreasing temperature, in agreement with findings by Kireeva et al. [242,308–310] and Abuzaid & Sehitoglu [311], who stated that lowering the deformation temperature shifts the onset of twinning to lower plastic strains and higher stresses.

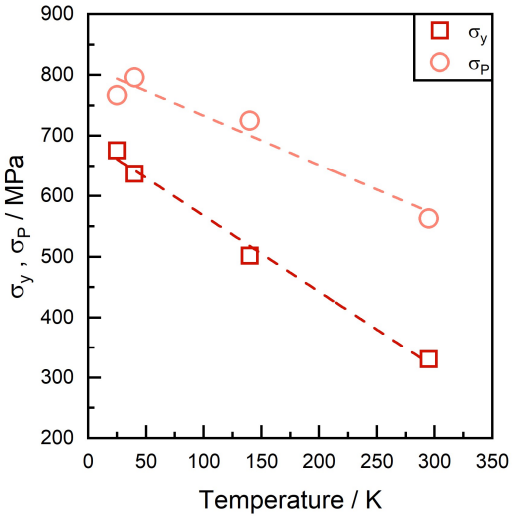

Figure 7.4: Yield strength (σ_y) and critical stress for widening of stacking faults (σ_P) as a function of the deformation temperature. The dashed lines are given to guide the eye.

7.4.4 Stacking fault energy as a function of temperature

Experimental stacking fault energies (γ_{isf}^{Exp}) were calculated with the equation proposed by Reed and Schramm [157]:

$$\gamma_{isf}^{Exp} = \frac{6.6 a_0 G_{111}}{\pi\sqrt{3}} \frac{\langle \varepsilon_{111}^2 \rangle}{SFP} A^{-0.37} \tag{7.4}$$

where G_{111} is the shear modulus in the {111} plane, a_0 is the lattice parameter and A is the Zener anisotropy.

The determined SFE values for the four test temperatures asymptotically approach a constant value with increasing true stress (Figure 7.5 a–d). A similar dependence of γ_{isf}^{Exp} on the true stress has been reported previously for HEAs/ MEAs and for stainless steels [112,113,307]. In line with the literature, the average values for the steady state regimes are taken as the experimental SFE values (see the horizontal

dashed lines in Figure 7.5 [112,113,307]). Evidently, the steady state regime is not yet reached at 295 K (Figure 7.5d). Therefore, the lowest SFE value is taken as the experimental SFE. It is reasoned that the absence of a plateau for 295 K is linked to the limited strain hardening at this temperature, which prevents wide stacking faults from forming in grains oriented less favorable for SF-formation/twinning with respect to the tensile axis.

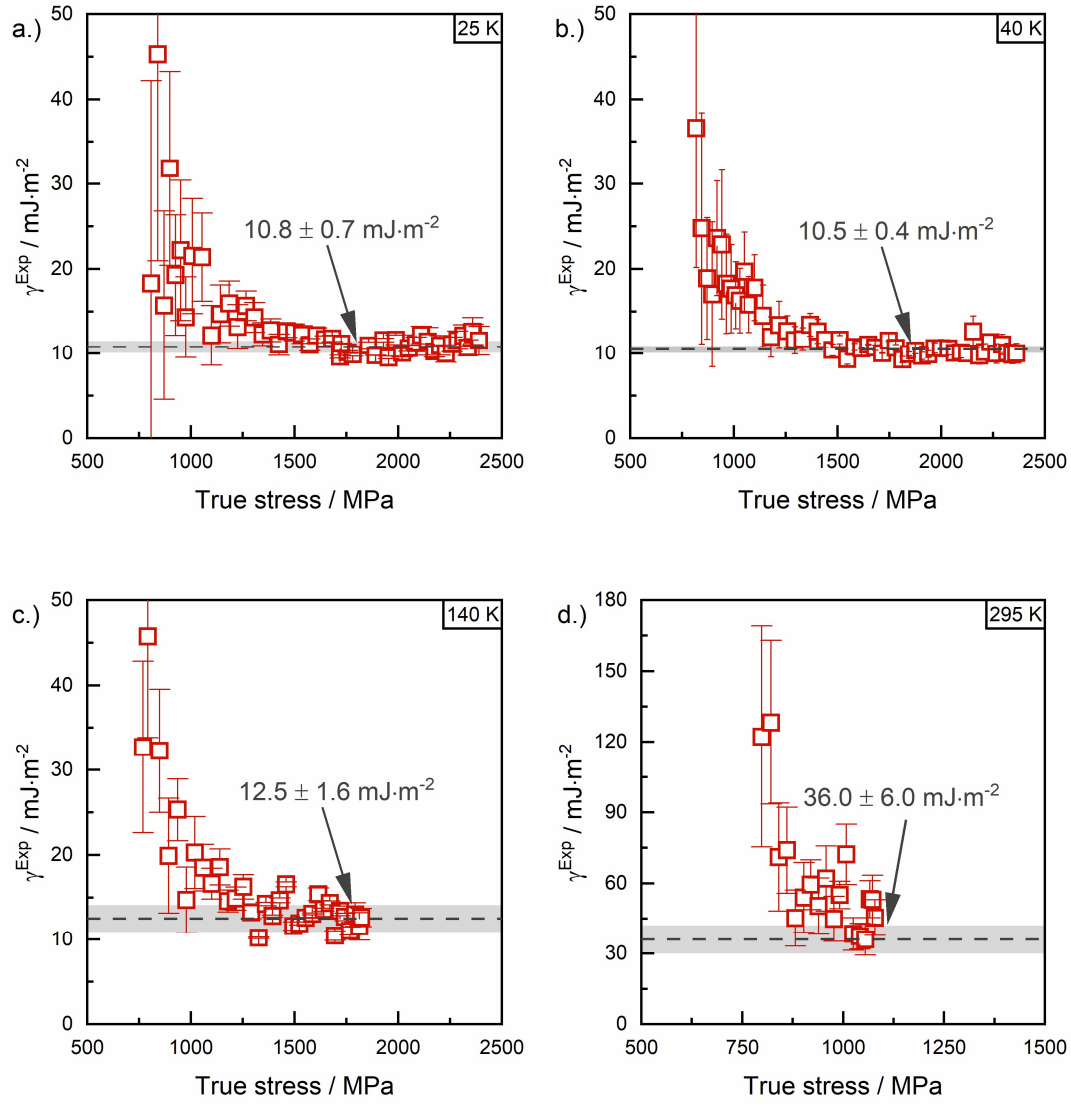

Figure 7.5: Stacking fault energy (γ_{isf}^{Exp}) determined according to Eq. (7.4) as a function of the true stress for the four different deformation temperatures – a.) 25 K, b.) 40 K, c.) 140 K and d.) 295 K.

The experimental SFE values in Figure 7.6 show a non-linear dependence on temperature and approach a constant value, for temperatures up to (at least) 140 K. This behavior resembles the experimental SFE values of Cu-Al alloys that exhibit an asymptotic trend towards a constant, positive value for increasing Al-content. This asymptotic behavior was demonstrated to be a consequence of the aforementioned, incomplete force balance over a stacking fault that biases positive experimental SFE values [206,301]. So far, no SFE values for the FeCoCrNi have been reported at temperatures as low as 25 K and 40 K. However, the SFE value of 36 mJ·m^{-2} at 295 K (cf. Table 7.2) is close to the values reported earlier in the literature, i.e. 27 – 32.5 mJ·m^{-2} [113,238,312], albeit slightly higher. The current, slightly higher SFE value is attributed to the small grain size in the samples investigated here. It was previously demonstrated that experimentally determined SFE values depend on grain size by a Hall-Petch type dependence, implying that smaller grains have a higher experimental SFE value [198,200,248].

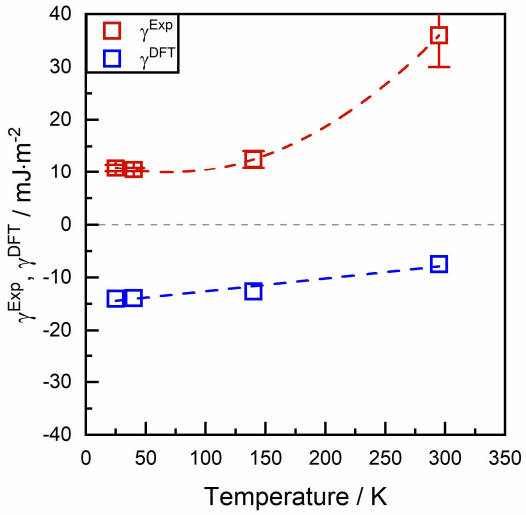

Figure 7.6: Experimental (γ_{isf}^{Exp}) and theoretical stacking fault energy (γ_{isf}^{DFT}) of the FeCoCrNi samples as a function of temperature.

Table 7.2: Stacking fault energy values of the FeCoCrCni specimens determined by DFT (γ_{isf}^{DFT}) and neutron diffraction (γ_{isf}^{Exp}).

	Temperature [K]			
	25	**40**	**140**	**295**
γ_{isf}^{DFT} [mJ·m^{-2}]	-7.5	-12.6	-13.9	-14
γ_{isf}^{Exp} [mJ·m^{-2}]	36	12.5	10.5	10.8

In contrast to the experimental values, the theoretical DFT values are negative and depend linearly on temperature and increase with 0.025 mJ·m^{-2} per K. This value is commensurate with the temperature dependence of SFE reported for stainless steels and HEAs [192,313]. The negative theoretical SFE values obtained from DFT illustrate that experimental validation of DFT simulations is not straightforward. The DFT values calculated for the SFE at 25 K and 40 K are higher than the typical values reported in the literature for 0 K [206]. In this respect it is recognized that 0 K SFE values reported in the literature rely on a lattice parameter value obtained with DFT, which is an underestimate of the actual lattice parameter [156,206]. For the room temperature sample investigated here, taking the lattice parameter as 3.577 Å instead of 3.5723 Å, results in a change in γ_{isf}^{DFT} from -7.5 mJ·m^{-2} to -1 mJ·m^{-2}. Analogously, results by Niessen et al. [218] demonstrate that the value for the lattice parameter has a significant influence on the SFE values calculated with DFT. It is therefore essential that experimental SFE values are compared to theoretical SFE values for the same (experimental) lattice parameter rather than for the value calculated with DFT.

7.5 Discussion

7.5.1 Critical resolved shear stress for twinning as a function of temperature

George et al. [314] thoroughly addressed the effect of temperature on the twinning stress in their review on the mechanical properties of HEAs and MEAs. Basically, the literature on this topic reports two irreconcilable observations. Certain investigations claim an increase in twinning stress with decreasing deformation temperature [242,308–311], while others report that the twinning stress is insensitive to temperature, or decreases with decreasing deformation temperature [112,113,119,120,154].

Generally, the observations of insensitivity or decreasing twinning stress upon lowering the deformation temperature in HEAs and MEAs rely on ex-situ TEM investigations of polycrystalline materials [119,120,154]. This approach has two sources of uncertainty. Firstly, the accuracy with which the onset of twinning can be detected with this method depends on the stress/strain intervals at which the ex-situ TEM characterization is performed. This becomes especially critical when the work hardening rate increases at a lower deformation temperature. Consequently, the stress/strain intervals should be selected along with the deformation temperature, meaning that for a lower temperature the interval between successive measurements should be reduced to guarantee an accurate critical twinning stress. Secondly, since deformation twinning is orientation dependent, the Schmid factor of the active/observed twin system is required to determine the twinning stress unambiguously. In ex-situ TEM, relating the crystal

orientation under investigation to the loading direction is challenging and far from straightforward. Therefore, the CRSS is often obtained from dividing the applied stress by the Taylor factor [119,120,154]. This may contribute to uncertainty in the determined twinning stress, despite preparation of TEM foils with a surface normal inclined 45 degrees relative to the loading direction as by Laplanche et al. [154].

Claims of an increasing twinning stress upon lowering the deformation temperature are often derived from ex-situ TEM observations of twinning in single crystals [242,308–311]. For single crystals the orientation dependence of twinning can be properly accounted for, but the selected stress/strain intervals in relation to temperature are still a source of uncertainty.

As noted by George et al. [314], in addition to the conflicting groups of experimental results, none of the models presented to date correctly describes the twinning stress for a variety of different *fcc* materials. The only hypothesis, which describes the twinning stress for *fcc* materials seemingly correctly, was previously presented in [248,301]. Herein it is postulated and quantitatively validated that the twinning stress multiplied by the Burgers vector of Shockley partial dislocations reconciles experimental and theoretical SFE values:

$$\gamma_{isf}^{Exp} = \gamma_{isf}^{DFT} + b_p \tau_{Twin} \tag{7.5}$$

$$\tau_{Twin} = \frac{\gamma_{isf}^{Exp} - \gamma_{isf}^{DFT}}{b_p} \tag{7.6}$$

The hypothesis departs from the assumption that the twinning stress is equal to the stress required to separate two Shockley partial dislocations. According to Eq. (7.6), τ_{Twin} can be calculated if γ_{isf}^{Exp} and γ_{isf}^{DFT} are known. The values for τ_{Twin} thus obtained are given for the leading partial dislocation in Figure 7.7a together with

the twinning stress determined from the threshold stress values in Figure 7.3 under the assumption that the Schmid factor is 0.47 (corresponding to a tensile direction parallel to $\langle 110 \rangle$). The CRSS values determined with the independent procedures more or less coincide for the specimen deformed at 295 K, but a major discrepancy occurs at 140 K, 40 K and 25 K. Values obtained through Eq. (7.6) appear to be constant up to 140 K, thereafter the twinning stress increases with temperature. On the other side, the values determined from threshold values in Figure 7.3 decrease with increasing temperature.

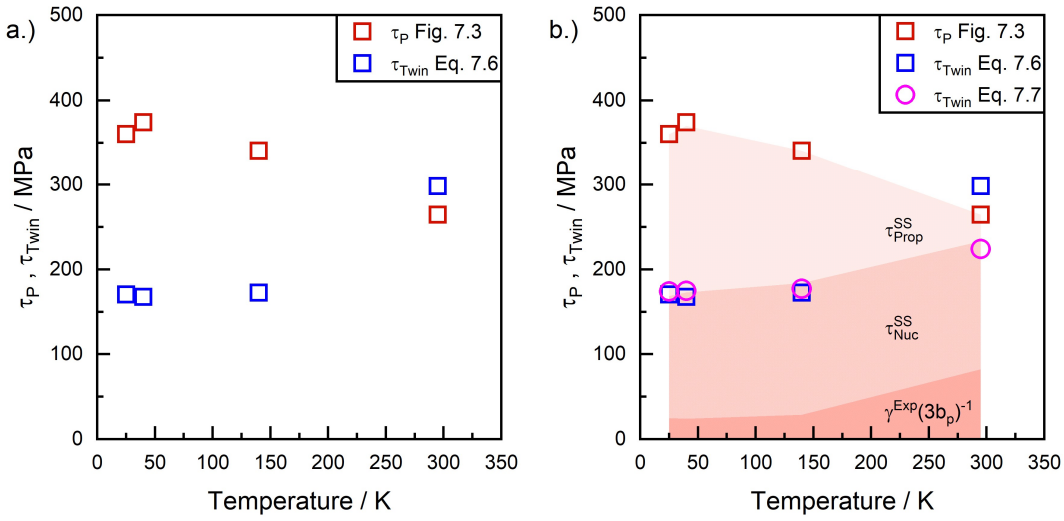

Figure 7.7: a.) Critical resolved shear stress for Shockley partial movement (τ_P) and for twinning (τ_{Twin}) determined from Eq. (7.6) and from Fig. 7.3 under the assumption of a Schmid factor of 0.47, b.) Critical resolved shear stress for Shockley partial movement (τ_P), given with the values for τ_{Twin} determined from Eqs. (7.6) and (7.7), as well as the contributions determined from Eq. (7.11), determined according to Eqs. (7.13), and (7.14).

Steinmetz et al. [135] presented a model for deformation twinning:

$$\tau_{Twin} = \frac{\gamma_{isf}^{Exp}}{3b_p} + \frac{3Gb_p}{L} \tag{7.7}$$

where L is the twin embryo length. In Steinmetz' model [135] deformation twinning is nucleation controlled, so τ_{Twin} in Eq. (7.7) solely accounts for the nucleation barrier of twin formation. Assuming $L = 260\,nm$, the values determined for τ_{Twin} (the blue circles in Figure 7.7b) agree excellently with the values determined according to Eq. (7.6) in the temperature range up to (at least) 140 K. This excellent agreement strongly suggests that the difference between γ_{isf}^{DFT} and γ_{isf}^{Exp} arises from the nucleation barrier for wide SF/ twin formation.

Kubilay & Curtin [315] reason that the critical resolved shear stress for twinning consists of a nucleation (τ_{Nuc}) and a growth/propagation contribution (τ_{Prop}):

$$\tau_{Twin} = \tau_{Nuc} + \tau_{Prop} \tag{7.8}$$

According to Kubilay & Curtin [315], the nucleation and propagation terms are:

$$\tau_{Nuc} = \tau_{Nuc}^{SS} + \frac{\gamma_{isf}^{Exp}}{nb_p} \tag{7.9}$$

$$\tau_{Prop} = \tau_{Prop}^{SS} \tag{7.10}$$

where τ_{Prop}^{SS} and τ_{Nuc}^{SS} are the contributions of solute strengthening to τ_{Twin} and $n = 3$ for the Mahajan & Chin [126] model as well as the Steinmetz et al. [135] model (Eq. (7.7)), which was demonstrated to apply for twinning in HEAs [25]. Considering that the Warren model [161] for determining SFP and, thus, SFE from X-ray and neutron diffraction data assumes the formation of "infinitely" wide stacking faults, implying nucleation and growth, and assuming $\tau_{Twin} \approx \tau_P$, it follows:

$$\tau_P = \tau_{Nuc}^{SS} + \frac{\gamma_{isf}^{Exp}}{3b_p} + \tau_{Prop}^{SS} \quad (7.11)$$

Obviously, $\tau_{Nuc}^{SS} = \frac{3Gb_p}{L}$ in Eq. (7.7). Following Eq. (7.11), the sum of τ_{Nuc}^{SS} and τ_{Prop}^{SS} corresponds to the difference between $\frac{\gamma_{isf}^{Exp}}{3b_p}$ and τ_P

$$\tau_{Nuc}^{SS} + \tau_{Prop}^{SS} = \tau_P - \frac{\gamma_{isf}^{Exp}}{nb_p}. \quad (7.12)$$

Kubilay & Curtin [315] argued that for twinning $\tau_{Nuc}^{SS} \approx \tau_{Prop}^{SS}$. This contradicts the opinion by Christian & Mahajan [287], who stated that an increase in deformation temperature and SFE may change the ratio of nucleation to propagation stress. Their claim concurs with observations reported by Tranchant et al. [286] that the rate controlling step for twinning in Cu-Al alloys changes from nucleation to propagation for an Al-content of approximately 8 – 10 at.%. This composition interval corresponds to a change in γ_{isf}^{DFT} from a positive (for lower contents) to a negative value [301]. Recognizing that γ_{isf}^{DFT} attains negative values for metastable materials, while γ_{isf}^{Exp} is positive by default, it is reasoned that the ratio of τ_{Nuc}^{SS} and τ_{Prop}^{SS} can change with temperature and composition. Pragmatically, γ_{isf}^{DFT} and γ_{isf}^{Exp} can be used for scaling the contributions of nucleation and propagation in twinning. For a stable material, both γ_{isf}^{DFT} and γ_{isf}^{Exp} are positive and $\gamma_{isf}^{DFT} < \gamma_{isf}^{Exp}$; for a metastable material $\gamma_{isf}^{DFT}<0$ and γ_{isf}^{Exp} is positive but small and, generally, $\left|\gamma_{isf}^{DFT}\right| < \gamma_{isf}^{Exp}$. Then, under the condition that Eq. (7.12) prevails, the contributions of nucleation and propagation can be scaled as follows:

$$\tau_{Nuc}^{SS} = \left(\tau_P - \frac{\gamma_{isf}^{Exp}}{3b_p}\right)\left(\frac{\gamma_{isf}^{Exp}}{\gamma_{isf}^{Exp} + \left|\gamma_{isf}^{DFT}\right|}\right) \quad (7.13)$$

$$\tau_{Prop}^{SS} = \left(\tau_P - \frac{\gamma_{isf}^{Exp}}{3b_p}\right)\left(\frac{\left|\gamma_{isf}^{DFT}\right|}{\gamma_{isf}^{Exp} + \left|\gamma_{isf}^{DFT}\right|}\right) \quad (7.14)$$

Using Eqs. (7.13 and (7.14, the values obtained for $\frac{\gamma_{isf}^{Exp}}{3b_p}$, τ_{Nuc}^{SS}, and τ_{Prop}^{SS} are given in Figure 7.7b by the shaded areas. It is apparent that, the contribution of the nucleation term ($\frac{\gamma_{isf}^{Exp}}{3b_p} + \tau_{Nuc}^{SS}$) to τ_P coincides with Eq. (7.7) and with τ_{Twin} evaluated with Eq. (7.6) (apart from the value at 295 K; see below). Accordingly, the difference between γ_{isf}^{DFT} and γ_{isf}^{Exp} correlates with the stress necessary for the nucleation of SFs. It is noted that the methods for determining SFE values by means of XRD and ND techniques (Eqs. 2 and 4) are calibrated on SFE values as originally experimentally determined with TEM techniques. Thus, the calibration is based on dissociated dislocations rather than on infinitely wide stacking faults. The values for τ_P comprise both nucleation and propagation contributions, because in Warren's assumption SFs can only be detected once they have an "infinite" width, implying that the resolved shear stress must have overcome both nucleation and propagation barriers.

Possible explanations for the lack of agreement between the three independent methods in the case of the room temperature sample (cf. Figure 7.7b) are the following. Firstly, the γ_{isf}^{Exp} versus true stress curve displayed in Figure 7.6 does not reach a stable plateau, and the actual value for γ_{isf}^{Exp} might be lower than 36 mJ·m^{-2}. According to Eq. (7.6), a discrepancy of e.g. 3 mJ·m^{-2} corresponds to a variation of 20 MPa in τ_{Twin}. Secondly, the uncertainty of σ_P, as established from the

piecewise linear fit, is greater for the 295 K specimen than for the specimens tested at cryogenic temperatures (cf. Figure 7.3). Thirdly, the DFT calculations are expected to have a higher level of uncertainty at elevated temperatures compared to calculations close to 0 K.

7.5.2 Deformation twinning as a function of deformation temperature

Deformation of the FeCoCrNi HEA at cryogenic temperatures leads to the formation of deformation twins (cf. Figure 7.2), while no deformation twins were observed in the specimen deformed at room temperature. Interpreting deformation twins in terms of the Mahajan & Chin [126] model (cf. Figure 7.8), the rate determining step for twinning is the convergence of the trailing partial dislocations on two co-planar slip systems.

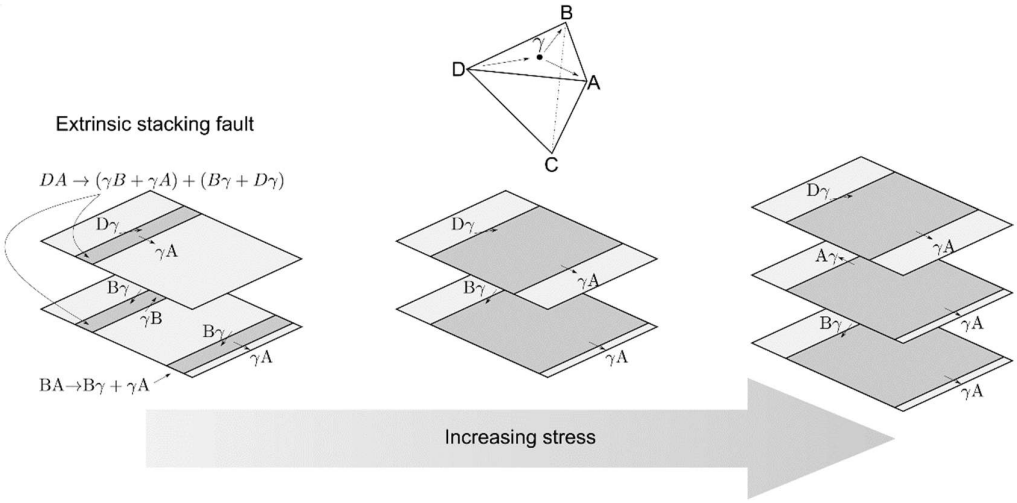

Figure 7.8: Schematic of the Mahajan & Chin [126] model for twinning.

Considering that the values for τ_P in Figure 7.7a determined from the SFP vs. true stress curves in Figure 7.3 are calculated for the leading Shockley partial dislocation, they do not correspond to the onset of twinning. Instead, twinning is expected when the resolved shear stress for the trailing partial dislocation exceeds the critical resolved shear stress, i.e. τ_P. For a tensile direction along <110>, the Schmid factor for the trailing partial dislocation is (0.235), i.e., half that of the leading Shockley partial dislocation (0.47). Hence, deformation twins are expected to form at a true stress that is twice that of the values determined for σ_P from the SFE vs. true stress curves. For specimens deformed at cryogenic temperatures the applied stress does exceed the stress necessary to form deformation twins. However, the true stress for the onset of twinning at room temperature would be 1126 MPa. This value is higher than the UTS at room temperature, so deformation twins are not expected to form, in agreement with the observations (Figure 7.2). Further, the nucleation stress $(\frac{\gamma_{isf}^{Exp}}{3b_p} + \tau_{Nuc}^{SS})$ is reached for the trailing partial dislocation at an applied stress of 991 MPa, which is only 18 MPa lower than the UTS of the 295 K specimen. Hence, the absence of deformation twins in the 295 K specimen is thought to be linked to the fact that the nucleation stress is only slightly exceeded and overcoming τ_P would require an applied stress higher than the UTS.

7.5.3 Correlation between stacking fault energy and prevailing deformation mechanism(s)

According to the DFT calculations, *fcc* FeCoCrNi is metastable ($\gamma_{isf}^{DFT} < 0$) for all four deformation temperatures and should, according to Olson & Cohen [235],

have a driving force to form martensite upon deformation. However, the diffractograms in Figure 7.1 show that the material remains *fcc* during deformation, irrespective of the deformation temperature. The absence of DIM was also observed in other metastable HEAs and MEAs, such as CoCrFeMnNi [294], $FeMn_{40}Co_{10}Cr_{10}$ [240]. The presented results indicate that the predominant deformation mechanism of metastable *fcc* materials may not be described alone in relation to their intrinsic SFE.

Recently, Lu et al. [136] pointed out that for slightly negative γ_{isf}^{DFT} values, *fcc* materials may deform by transformation-mediated twinning (TMT). First, wide SFs and fine ε −martensite platelets form during deformation, as the latter is energetically favorable ($\gamma_{isf}^{DFT} < 0$). On continued deformation, SFs start to form on the basal plane of ε −martensite, which eventually reverts to *fcc* austenite, where the reverted austenite exhibits a twin orientation with respect to the matrix austenite. The formation of SFs in ε −martensite upon deformation has been corroborated for a metastable FeMnC steel by Pramanik et al. [316]. Furthermore, Wei et al. [317] confirmed via in-situ SEM/EBSD experiments that reverted austenite forms from ε −martensite via the formation of basal stacking faults in a FeMnCo MEA. Since the γ_{isf}^{DFT} values of the investigated FeCoCrNi HEA fall within the γ_{isf}^{DFT} −range, which according to Lu et al. can lead to TMT, cf. Fig. 4a in Ref. [136], it is considered likely that the absence of diffraction peaks corresponding to ε −martensite is related to the occurrence of TMT.

7.6 Conclusions

The present study investigated the relation between deformation temperature, experimental as well theoretical SFE values, and the occurrence of deformation twinning in an *fcc* FeCoCrNi HEA by neutron diffraction, transmission electron microscopy and DFT modelling. The conclusions are:

- Experimentally determined SFE values are positive and exhibit an asymptotic behavior upon lowering the deformation temperature. In contrast, SFE values determined from DFT are negative and exhibit a linear dependence on temperature.
- The critical resolved shear stress for Shockley partial dislocations can be inferred from *SFP* vs. true stress plots and increases with decreasing deformation temperature.
- Contributions of nucleation and propagation to the critical resolved shear stress for Shockley partial dislocations can be identified based on the ratio of experimental and theoretical SFE values.
- Correcting experimental SFE values for the contribution of nucleation to the critical resolved shear stress for Shockley partial dislocations yields negative SFE values, which coincide with values predicted by DFT.

8 Summary and Conclusions

The primary conclusion that can be drawn from the work presented in this Ph.D. thesis is that experimental and theoretical stacking fault energy values differ for both metastable and stable face-centered cubic alloys, as well as pure face-centered cubic metals. The discrepancy arises from the resistance against the movement of Shockley partial dislocations, which has been so far neglected in the experimental determination of the stacking fault energy. For detailed conclusions, the reader is referred to the individual manuscripts in Chapters 5 – 7.

Nevertheless, some general conclusions can be drawn.

First, experimental stacking fault energy values should be regarded as apparent values and do not correspond to an intrinsic materials property. Instead, they are influenced by a materials microstructure, as shown for the example of the grain size dependence, which may explain the reduction in propensity for twin and martensite formation upon grain refinement.

Second, experimental stacking fault energies can be reconciled with theoretical stacking fault energy values by considering the resistance against the movement of Shockley partial dislocations in the force balance over a stacking fault, which the experimental SFE assessment departs from. Accordingly, corrected experimental SFE values of metastable face-centered cubic materials are negative and correspond well to SFE values predicted by density functional theory calculations.

Third, models predicting the critical resolved shear stress for twinning based on experimental SFE values rely on (arbitrary) fitting parameters and are commonly

solely applicable to specific alloy systems and/or narrow compositional spaces. Furthermore, the hitherto available models predict the twinning stress for high- and medium-entropy alloys incorrectly. On the contrary, the proposed hypothesis that the difference between experimental and theoretical SFE values depends on the twinning stress, provides a consistent quantitative interpretation of data for both alloys with positive and negative stacking fault energy.

Fourth, the suggested correction for experimental SFE values relies on the accurate assessment of the critical resolved shear stress for twinning, which is not straightforward to assess experimentally. Ex-situ transmission mission electron microscopy of specimens strained to different plastic strains enables the assessment, but is labor intensive. Instead, it is suggested that the resistance against the movement of Shockley partial dislocations can be inferred from stacking fault probabilities vs. true stress curves obtained by in-situ neutron or X-ray diffraction, which shows promising results.

9 Further work

The current Ph.D. project revealed an opportunity to reconcile the discrepancy between experimental and theoretical stacking fault energy values, which arises from the negligence of the resistance against Shockley partial dislocation movement in the experimental assessment of the stacking fault energy. The chapter comprises suggestions for further research topics that were not covered in the submitted Ph.D. thesis and deserve further research.

9.1 The effect of interstitials on the stacking fault energy

The effect of interstitial elements such as nitrogen and carbon on the stacking fault energy is still a matter of ongoing debate. It is suggested that the effect of interstitial elements on the stacking fault energy should be investigated in light of the findings presented in this Ph.D. thesis. It may be that some of the disagreement on the effect of interstitials originates from the effect of N-/C-addition on the excess stacking fault energy arising from the critical resolved shear stress for twinning. It could be that in alloys with contents of Cr, V, Mo, i.e. elements with a high affinity for N and C, interstitial alloying may have a more marked effect on the excess SFE than in alloys with low contents of these high-affinity elements, e.g. the Fe-Mn-C system. Furthermore, on comparing results regarding the effect of interstitial elements on the experimental SFE, it is crucial to take the effect of the grain size into account, or exclude grain size effects by solely comparing materials with similar grain size. Here, preliminary results obtained on AISI 347 loaded with different nitrogen contents are presented.

The following sections comprises preliminary results on the effect of nitrogen on the stacking fault energy and the deformation mechanisms in metastable AISI 347.

9.1.1 Experimental methods

The chemical composition of the as-nitrided AISI 347 specimens is given in Table 9. Prior to high-temperature solution nitriding (HTSN), tensile specimens with gauge dimensions of 25 mm × 4 mm × 3 mm were machined by wire electrical discharge machining from the as-annealed material. HTSN was performed in a custom-build horizontal Kanthal tube furnace at 1150 °C (1423 K) for 22 h at 13 mbar, 35 mbar, and 105 mbar N_2 partial pressure. High-pressure gas quenching was applied to avoid nitride formation during cooling. The N-content of the as-nitrided specimens was determined by Instrumental Gas Analysis on a LECO TC500 and corresponds to an average of three measurements.

Table 3: Chemical composition of the as-nitrided AISI 347 specimens.

	Chemical composition in wt %							
Specimen	Fe	C	N	Cr	Ni	Mn	Mo	Nb.
13 mbar	Bal.	0.03	0.09	17.56	9.00	1.48	0.02	0.59
35 mbar	Bal.	0.03	0.12	17.75	9.12	1.51	0.01	0.59
105 mbar	Bal.	0.03	0.18	17.76	9.05	1.60	0.01	0.59

The in-situ neutron diffraction experiments were performed at the TAKUMI Engineering Materials Diffractometer, beamline-19 of the Materials and Life Science Experimental Facility at the Japan Proton Accelerator Research Complex. The tensile direction was inclined 45 ° relative to the incident neutron beam. Diffractograms were thus acquired with scattering vectors parallel to and normal to the tensile direction on the two detector banks, which are installed at –90 ° and +90 ° with respect to the incident neutron beam, respectively. Thus, during the in-situ tensile tests data was acquired both along loading and transverse direction. Tensile loading experiments were carried out at a strain rate of 2.67×10^{-5} s^{-1}. Data analysis was carried out as mentioned in Manuscript III (Chapter 7).

9.1.2 Preliminary experimental results

The stress strain curves of the as-nitrided AISI 347 specimens are shown in Figure 9.1. It is apparent that N-alloying leads to an increase in yield strength and ultimate tensile strength, while maintaining the ductility.

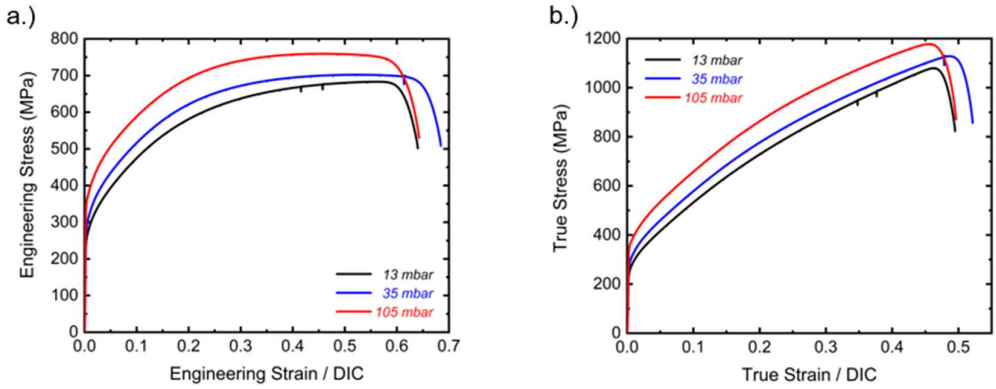

Figure 9.1: a.) Engineering stress strain curves of the nitrided AISI 347 specimens, b.) True stress strain curves of the nitrided AISI 347 specimens.

Prior to loading, the specimens consisted of face-centered cubic austenite and Nb(C,N), cf.

Figure 9.2 a.) – f.). The diffractograms for specimens 1N (13 mbar) and the 2N (35 mbar) at higher strains showed peaks corresponding to the 110 reflection of α' –martensite at d spacing of approx. 1.95 Å. On the other hand, specimen 3N (105 mbar) exhibited no signs of strain-induced martensite formation.

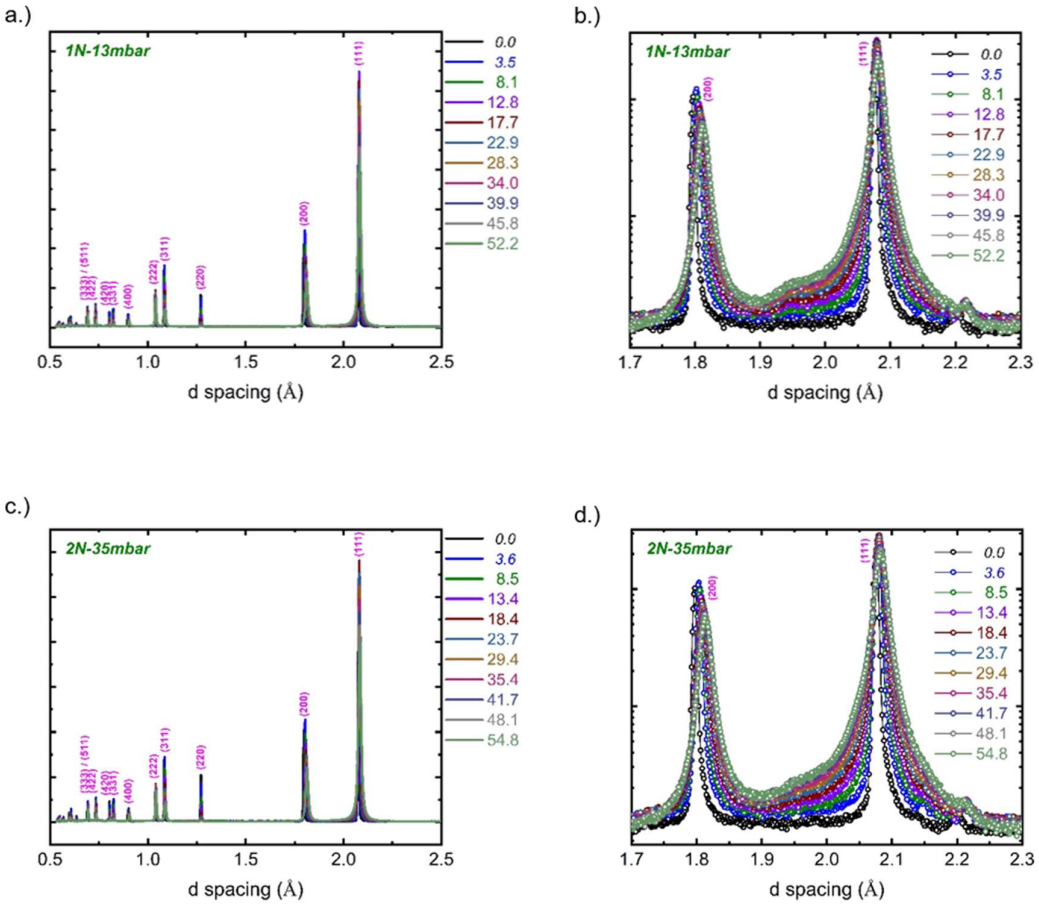

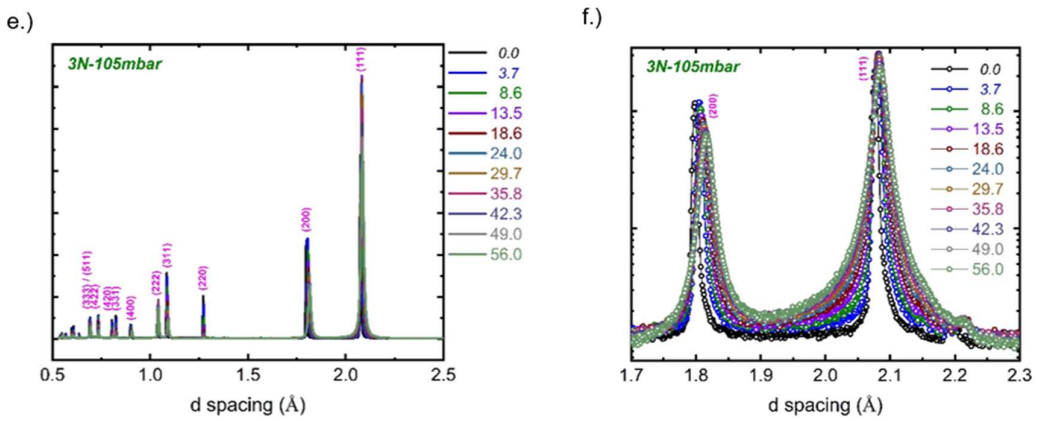

Figure 9.2: a.) Diffractograms of the 1N specimen upon loading, b.) Detailed view of the 1N specimen diffractograms, c.) Diffractograms of the 2N specimen upon loading, d.) Detailed view of the 2N specimen diffractograms, c.) Diffractograms of the 3N specimen upon loading, d.) Detailed view of the 3N specimen diffractograms.

The observation of diffraction peaks from α' −martensite upon loading in the 1N and 2N specimen, is corroborated by corresponding phase maps of as-fractured specimens in Figure 9.3 a.) and c.), respectively. In addition to α' −martensite, it is apparent that a high density of deformation twins has formed. In contrast to the 1N and 2N specimens, the 3N specimen exhibits no signs of α' −martensite formation. Instead, deformation twinning in conjunction with dislocation glide appears to be the prevalent deformation mechanisms for 3N. Apparently, the addition of 0.18 wt % N is sufficient to stabilize austenite and prevent strain-induced martensite formation upon tensile loading.

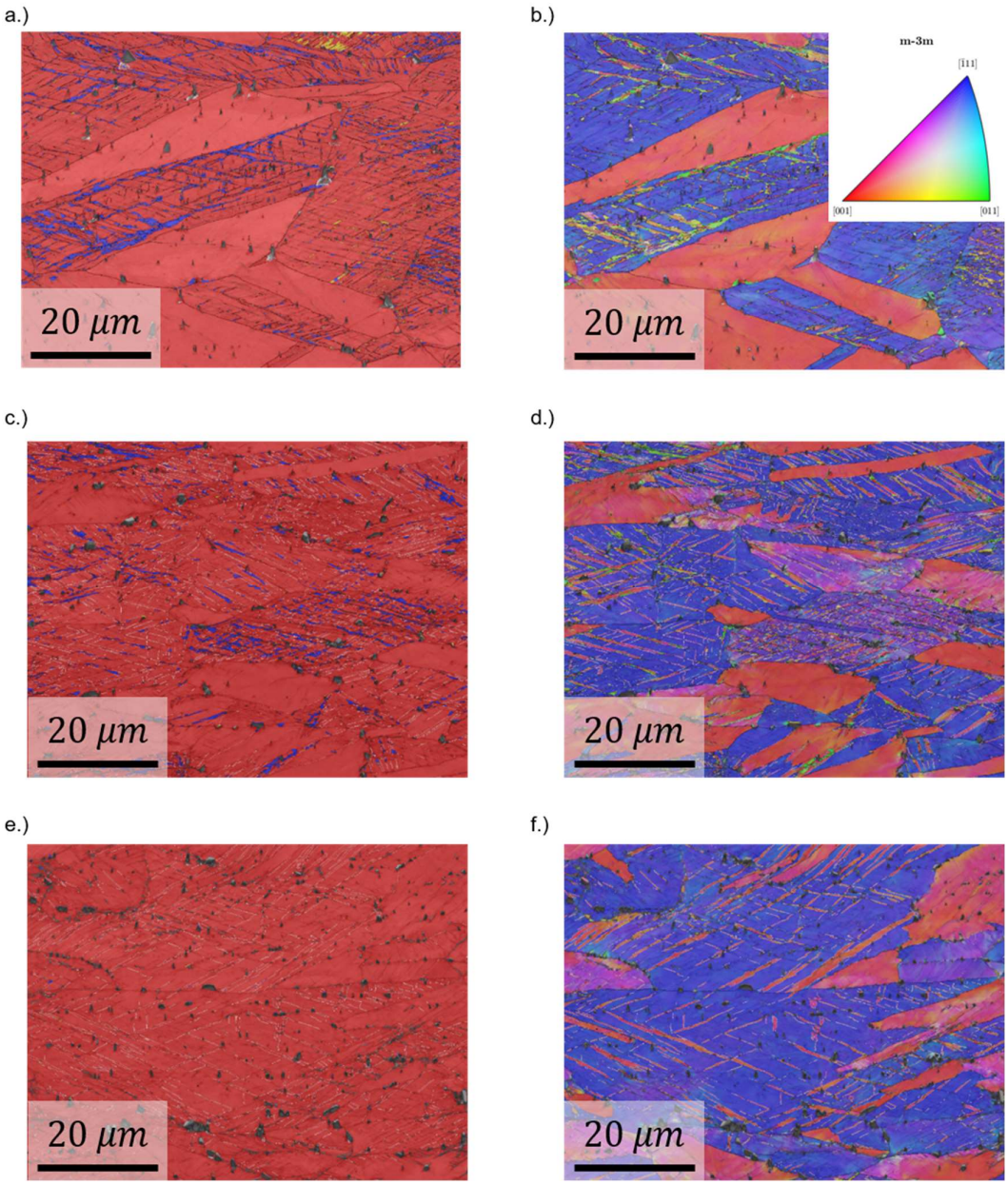

Figure 9.3: Loading direction for all specimens parallel to the horizontal axis. Austenite red and α' –martensite blue. a.) Phase map of 1N specimen, b.) Orientation map of 1N specimen, c.) Phase map of 2N specimen, d.) Orientation map of 2N specimen, e.) Phase map of 3N specimen, and f.) Orientation map of 3N specimen.

The lattice strain evolution of the 111 and 222 reflections as a function of the true stress of the 1N, 2N and 3N specimens are given in Figure 9.4a. It is apparent that upon surpassing a stress threshold, the lattice strains diverges for the two sets of

lattice planes, which indicates the formation of wide stacking faults. The stacking fault probabilities determined from the divergence (cf. Eq. (7.2)) are given in Figure 9.4b for the three specimens. Apparently, the threshold stresses for stacking fault formation in specimens 1N and 2N are equal; for the 3N specimen the necessary stress to form wide stacking faults is higher. This may be caused by a higher stacking fault energy for the 3N specimen (cf. Figure 9.4c), as well as the increase in the nucleation and propagation stress for Shockley partial dislocations as discussed in Manuscript III.

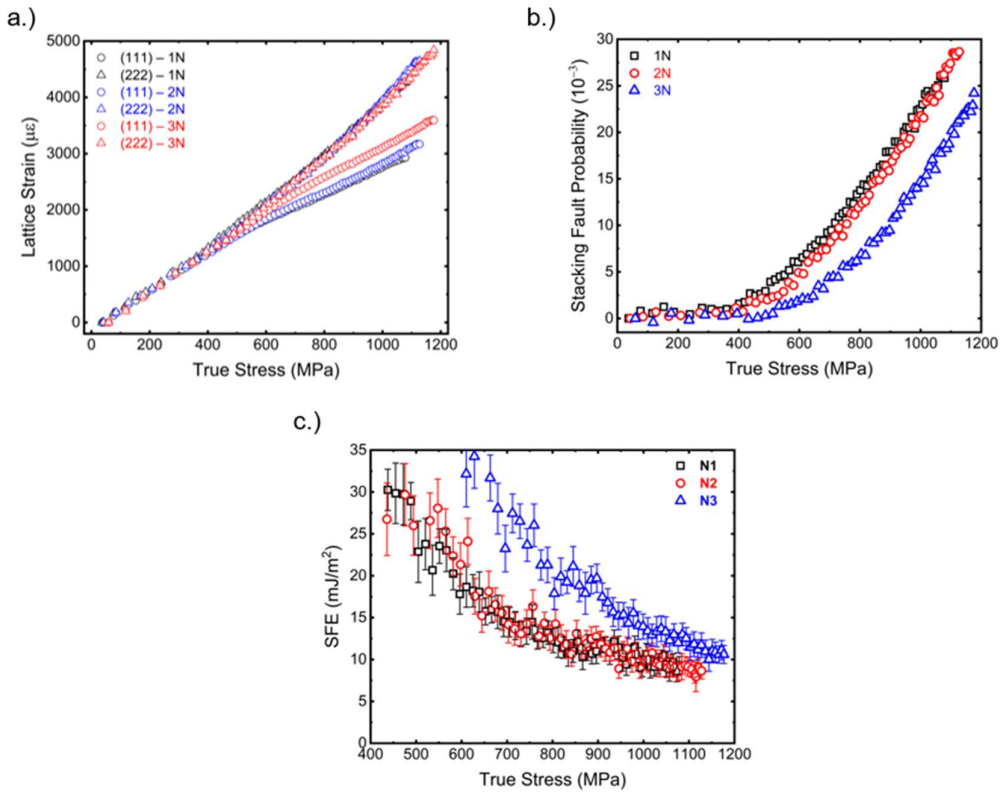

Figure 9.4: a.) Lattice strain evolution for the 111 and 222 reflection along the loading direction, b.) Evolution of the stacking fault probability versus true, and c.) Evolution of the experimental stacking fault energy versus true stress for the 1N, 2N, and 3N specimens, respectively.

Although, the difference in the experimental stacking fault energies is small (approx. 3-5 $mJ \cdot m^{-2}$), the transition from martensite formation to deformation in the composition range 0.12 – 0.18 wt.% N corresponds very well with the DFT predictions presented in Niessen et al. [218] for AISI 304[4], where a transition from negative to positive stacking fault energy at approx. 0.1 wt.% N.

Despite being preliminary, the presented results indicate that N-addition to AISI 347 leads to an increase in the material's stacking fault energy, which is accompanied by a transition from martensite formation to deformation twinning. Furthermore, the results show that higher strength at maintained ductility can be achieved by targeted interstitial alloying.

9.2 Considering the critical resolved shear stress for twinning in alloy design

As discussed in Chapter 2.7, the point of onset of twinning and/or martensite formation affects the magnitude of work hardening strongly. It appears that an earlier onset, at least of deformation twinning, leads to higher work hardening by suppressing cross slip and therefore dislocation annihilation. This implies that in order to design alloys with excellent combinations of high strength and high ductility it is essential to not only tailor a material's SFE, but also to control the onset of twinning/martensite formation by controlling the mobility of Shockley partial dislocations. As such, it is desirable to develop a method that can predict the critical resolved shear stress for twinning in a more straightforward manner than by density

[4] It noted that the substitutional compositions of AISI 347 and AISI 304 are almost identical. The only difference is the presence of Nb, which was deliberately chosen, because NbC strongly retards grain growth during high temperature solution nitriding for controlled nitrogen dissolution.

functional theory calculations and that also includes the effects of the microstructure. In light of this research it is recommended that the formation of deformation twins and deformation induced martensite should be regarded as being governed by thermodynamics, i.e. the intrinsic SFE, and kinetics, i.e. the resistance against Shockley partial movement.

9.3 Effect of precipitates on the stacking fault energy and deformation mechanisms

If, as herein suggested, the experimental SFE depends on a material's microstructure, it is of potential interest to investigate the influence of precipitates on experimental SFE values. To this extent, both coherent as well as incoherent precipitates should be investigated with respect to their effect on the SFE and linked to the propensity for twinning and martensite formation.

References

[1] D. Raabe, Z. Li, D. Ponge, Metastability alloy design, MRS Bull. 44 (2019) 266–272. https://doi.org/10.1557/mrs.2019.72.

[2] T.M. Pollock, A. Van Der Ven, The evolving landscape for alloy design, MRS Bull. 44 (2019) 238–246. https://doi.org/10.1557/mrs.2019.69.

[3] R.O. Ritchie, The conflicts between strength and toughness, Nat. Mater. 10 (2011) 817–822. https://doi.org/10.1038/nmat3115.

[4] S.W. Wu, G. Wang, Y.D. Jia, J. Yi, Q.J. Zhai, C.T. Liu, B.A. Sun, H.J. Chu, J. Shen, P.K. Liaw, T.Y. Zhang, Enhancement of strength-ductility trade-off in a high-entropy alloy through a heterogeneous structure, Acta Mater. 165 (2019) 444–458. https://doi.org/10.1016/J.ACTAMAT.2018.12.012.

[5] C. Herrera, D. Ponge, D. Raabe, Design of a novel Mn-based 1 GPa duplex stainless TRIP steel with 60% ductility by a reduction of austenite stability, Acta Mater. 59 (2011) 4653–4664. https://doi.org/10.1016/j.actamat.2011.04.011.

[6] L.B. Chen, R. Wei, K. Tang, J. Zhang, F. Jiang, L. He, J. Sun, Heavy carbon alloyed FCC-structured high entropy alloy with excellent combination of strength and ductility, Mater. Sci. Eng. A. 716 (2018) 150–156. https://doi.org/10.1016/j.msea.2018.01.045.

[7] J. Su, D. Raabe, Z. Li, Hierarchical microstructure design to tune the mechanical behavior of an interstitial TRIP-TWIP high-entropy alloy, Acta Mater. 163 (2019) 40–54. https://doi.org/10.1016/j.actamat.2018.10.017.

[8] Y. Wei, Y. Li, L. Zhu, Y. Liu, X. Lei, G. Wang, Y. Wu, Z. Mi, J. Liu, H. Wang, H. Gao, Evading the strength-ductility trade-off dilemma in steel through gradient hierarchical nanotwins, Nat. Commun. 5 (2014) 1–8. https://doi.org/10.1038/ncomms4580.

[9] I. Moravcik, H. Hadraba, L. Li, I. Dlouhy, D. Raabe, Z. Li, Yield strength increase of a CoCrNi medium entropy alloy by interstitial nitrogen doping at maintained ductility, Scr. Mater. 178 (2020) 391–397. https://doi.org/10.1016/j.scriptamat.2019.12.007.

[10] Z. Lei, X. Liu, Y. Wu, H. Wang, S. Jiang, S. Wang, X. Hui, Y. Wu, B. Gault, P. Kontis, D. Raabe, L. Gu, Q. Zhang, H. Chen, H. Wang, J. Liu, K. An, Q. Zeng, T.G. Nieh, Z. Lu, Enhanced strength and ductility in a high-entropy alloy via ordered oxygen complexes, Nature. 563 (2018) 546–550. https://doi.org/10.1038/s41586-018-0685-y.

[11] J. Feng, H. Zhao, H. Peng, G. Wang, L. Zhang, Y. Wen, Enhancement of strength-ductility combination in recovery-annealed Fe-Mn-C twinning-induced plasticity steels by Si alloying, Mater. Res. Express. 5 (2018). https://doi.org/10.1088/2053-1591/aacdaf.

[12] C. Lei, X. Deng, X. Li, Z. Wang, Simultaneous enhancement of strength and ductility through coordination deformation and multi-stage transformation induced plasticity (TRIP) effect in heterogeneous metastable austenitic steel, Scr. Mater. 162 (2019) 421–425. https://doi.org/10.1016/j.scriptamat.2018.12.007.

[13] Y. Han, H. Li, H. Feng, K. Li, Y. Tian, Z. Jiang, Simultaneous enhancement in strength and ductility of Fe50Mn30Co10Cr10 high-entropy alloy via

nitrogen alloying, J. Mater. Sci. Technol. 65 (2021) 210–215. https://doi.org/10.1016/j.jmst.2020.04.072.

[14] G. Gao, H. Zhang, X. Gui, P. Luo, Z. Tan, B. Bai, Enhanced ductility and toughness in an ultrahigh-strength Mn-Si-Cr-C steel: The great potential of ultrafine filmy retained austenite, Acta Mater. 76 (2014) 425–433. https://doi.org/10.1016/j.actamat.2014.05.055.

[15] Z. Li, K.G. Pradeep, Y. Deng, D. Raabe, C.C. Tasan, Metastable high-entropy dual-phase alloys overcome the strength-ductility trade-off, Nature. 534 (2016) 227–230. https://doi.org/10.1038/nature17981.

[16] T.Z. Khan, T. Kirk, G. Vazquez, P. Singh, A. V. Smirnov, D.D. Johnson, K. Youssef, R. Arróyave, Towards stacking fault energy engineering in FCC high entropy alloys, Acta Mater. 224 (2022) 117472. https://doi.org/10.1016/J.ACTAMAT.2021.117472.

[17] S.J. Lee, J. Han, S. Lee, S.H. Kang, S.M. Lee, Y.K. Lee, Design for Fe-high Mn alloy with an improved combination of strength and ductility, Sci. Rep. 7 (2017) 1–9. https://doi.org/10.1038/s41598-017-03862-y.

[18] D.T. Pierce, J.A. Jiménez, J. Bentley, D. Raabe, J.E. Wittig, The influence of stacking fault energy on the microstructural and strain-hardening evolution of Fe-Mn-Al-Si steels during tensile deformation, Acta Mater. 100 (2015) 178–190. https://doi.org/10.1016/j.actamat.2015.08.030.

[19] S. Lu, X. Sun, X. An, W. Li, Y. Chen, H. Zhang, L. Vitos, Transformation-mediated twinning, (2019). https://arxiv.org/abs/1910.11748v2 (accessed August 30, 2021).

[20] Z. Li, F. Körmann, B. Grabowski, J. Neugebauer, D. Raabe, Ab initio assisted design of quinary dual-phase high-entropy alloys with transformation-induced plasticity, Acta Mater. 136 (2017) 262–270. https://doi.org/10.1016/j.actamat.2017.07.023.

[21] T.H. Lee, E. Shin, C.S. Oh, H.Y. Ha, S.J. Kim, Correlation between stacking fault energy and deformation microstructure in high-interstitial-alloyed austenitic steels, Acta Mater. 58 (2010) 3173–3186. https://doi.org/10.1016/j.actamat.2010.01.056.

[22] L. Rémy, INTERACTION BETWEEN SLIP AND TWINNING SYSTEMS AND THE INFLUENCE OF TWINNING ON THE MECHANICAL BEHAVIOR OF fcc METALS AND ALLOYS., Metall. Trans. A, Phys. Metall. Mater. Sci. 12 A (1981) 387–408. https://doi.org/10.1007/bf02648536.

[23] Y. Tian, O.I. Gorbatov, A. Borgenstam, A. V. Ruban, P. Hedström, Deformation Microstructure and Deformation-Induced Martensite in Austenitic Fe-Cr-Ni Alloys Depending on Stacking Fault Energy, Metall. Mater. Trans. A Phys. Metall. Mater. Sci. 48 (2017) 1–7. https://doi.org/10.1007/s11661-016-3839-2.

[24] S. Allain, J.P. Chateau, O. Bouaziz, S. Migot, N. Guelton, Correlations between the calculated stacking fault energy and the plasticity mechanisms in Fe-Mn-C alloys, Mater. Sci. Eng. A. 387–389 (2004) 158–162. https://doi.org/10.1016/j.msea.2004.01.059.

[25] L. Ding, A. Hilhorst, H. Idrissi, P.J. Jacques, Potential TRIP/TWIP coupled effects in equiatomic CrCoNi medium-entropy alloy, Acta Mater. 234 (2022) 118049. https://doi.org/10.1016/j.actamat.2022.118049.

[26] P. Behjati, A. Kermanpur, A. Najafizadeh, H. Samaei Baghbadorani, L.P. Karjalainen, J.G. Jung, Y.K. Lee, Design of a new Ni-free austenitic stainless steel with unique ultrahigh strength-high ductility synergy, Mater. Des. 63 (2014) 500–507. https://doi.org/10.1016/j.matdes.2014.06.069.

[27] R. Mohammadzadeh, A. Akbari, Grain refinement of a nickel and manganese free austenitic stainless steel produced by pressurized solution nitriding, Mater. Charact. 93 (2014) 119–128. https://doi.org/10.1016/j.matchar.2014.04.001.

[28] G. Balachandran, M.L. Bhatia, N.B. Ballal, P.K. Rao, Some theoretical aspects on designing nickel free high nitrogen austenitic stainless steels, ISIJ Int. 41 (2001) 1018–1027. https://doi.org/10.2355/isijinternational.41.1018.

[29] Z. Li, C.C. Tasan, H. Springer, B. Gault, D. Raabe, Interstitial atoms enable joint twinning and transformation induced plasticity in strong and ductile high-entropy alloys, Sci. Rep. 7 (2017) 1–7. https://doi.org/10.1038/srep40704.

[30] Z.C. Luo, M.X. Huang, The role of interstitial carbon atoms on the strain-hardening rate of twinning-induced plasticity steels, Scr. Mater. 178 (2020) 264–268. https://doi.org/10.1016/j.scriptamat.2019.11.047.

[31] T. Tsuchiyama, K. Inoue, K. Hyodo, D. Akama, N. Nakada, S. Takaki, T. Koyano, Comparison of microstructure and hardness between high-carbon and high-nitrogen martensites, ISIJ Int. 59 (2019) 161–168. https://doi.org/10.2355/isijinternational.ISIJINT-2018-404.

[32] J. Nakano, A thermo-mechanical correlation with driving forces for hcp martensite and twin formations in the Fe-Mn-C system exhibiting multicomposition sets, Sci. Technol. Adv. Mater. 14 (2013) 14207–14214.

https://doi.org/10.1088/1468-6996/14/1/014207.

[33] M. Fujikura, K. Takada, K. Ishida, EFFECT OF MANGANESE AND NITROGEN ON THE MECHANICAL PROPERTIES OF Fe-18%Cr-10%Ni STAINLESS STEELS., Trans Iron Steel Inst Jap. 15 (1975) 464–469. https://doi.org/10.2355/isijinternational1966.15.464.

[34] Y. Kawahara, R. Teranishi, C. Takushima, J.I. Hamada, K. Kaneko, Effect of nitrogen addition on the stacking-fault energies in Si-added austenitic stainless steel, ISIJ Int. 61 (2021) 1029–1036. https://doi.org/10.2355/ISIJINTERNATIONAL.ISIJINT-2020-609.

[35] L. Bracke, J. Penning, N. Akdut, The influence of Cr and N additions on the mechanical properties of FeMnC steels, Metall. Mater. Trans. A Phys. Metall. Mater. Sci. 38 (2007) 520–528. https://doi.org/10.1007/s11661-006-9084-3.

[36] T.H. Lee, H.Y. Ha, B. Hwang, S.J. Kim, E. Shin, Effect of carbon fraction on stacking fault energy of austenitic stainless steels, Metall. Mater. Trans. A Phys. Metall. Mater. Sci. 43 (2012) 4455–4459. https://doi.org/10.1007/s11661-012-1423-y.

[37] R.E. Stoltz, J.B. Vander Sande, The effect of nitrogen on stacking fault energy of Fe-Ni-Cr-Mn steels, Metall. Trans. A. 11 (1980) 1033–1037. https://doi.org/10.1007/BF02654717.

[38] N. Saenarjhan, J.H. Kang, S.J. Kim, Effects of carbon and nitrogen on austenite stability and tensile deformation behavior of 15Cr-15Mn-4Ni based austenitic stainless steels, Mater. Sci. Eng. A. 742 (2019) 608–616. https://doi.org/10.1016/j.msea.2018.11.048.

[39] R.E. Schramm, R.P. Reed, Stacking fault energies of seven commercial austenitic stainless steels, Metall. Trans. A. 6 (1975) 1345–1351. https://doi.org/10.1007/BF02641927.

[40] S. Wang, K. Yang, Y. Shan, L. Li, Plastic deformation and fracture behaviors of nitrogen-alloyed austenitic stainless steels, Mater. Sci. Eng. A. 490 (2008) 95–104. https://doi.org/10.1016/j.msea.2008.01.015.

[41] S.J. Lee, Y.S. Jung, S. Il Baik, Y.W. Kim, M. Kang, W. Woo, Y.K. Lee, The effect of nitrogen on the stacking fault energy in Fe-15Mn-2Cr-0.6C-xN twinning-induced plasticity steels, Scr. Mater. 92 (2014) 23–26. https://doi.org/10.1016/j.scriptamat.2014.08.004.

[42] V.M. Blinov, A.M. Glezer, I.O. Bannykh, E.I. Lukin, E.N. Blinova, O.A. Bannykh, E. V. Blinov, O.P. Chernogorova, M.A. Samoilova, D. V. Chernenok, Effect of Carbon and Nitrogen on the Stacking Fault Energy in Austenitic Steels, Russ. Metall. 2022 (2022) 347–354. https://doi.org/10.1134/S0036029522040061.

[43] V. Gavriljuk, Y. Petrov, B. Shanina, Effect of nitrogen on the electron structure and stacking fault energy in austenitic steels, Scr. Mater. 55 (2006) 537–540. https://doi.org/10.1016/j.scriptamat.2006.05.025.

[44] E.P. George, D. Raabe, R.O. Ritchie, High-entropy alloys, Nat. Rev. Mater. 4 (2019) 515–534. https://doi.org/10.1038/s41578-019-0121-4.

[45] J.W. Yeh, S.K. Chen, S.J. Lin, J.Y. Gan, T.S. Chin, T.T. Shun, C.H. Tsau, S.Y. Chang, Nanostructured high-entropy alloys with multiple principal elements: Novel alloy design concepts and outcomes, Adv. Eng. Mater. 6 (2004) 299–303. https://doi.org/10.1002/adem.200300567.

[46] J.-W.W. Yeh, Alloy design strategies and future trends in high-entropy alloys, JOM. 65 (2013) 1759–1771. https://doi.org/10.1007/s11837-013-0761-6.

[47] M.H. Tsai, J.W. Yeh, High-entropy alloys: A critical review, Mater. Res. Lett. 2 (2014) 107–123. https://doi.org/10.1080/21663831.2014.912690.

[48] D.B.B. Miracle, O.N.N. Senkov, A critical review of high entropy alloys and related concepts, Acta Mater. 122 (2017) 448–511. https://doi.org/10.1016/j.actamat.2016.08.081.

[49] F. Otto, Y. Yang, H. Bei, E.P. George, Relative effects of enthalpy and entropy on the phase stability of equiatomic high-entropy alloys, Acta Mater. 61 (2013) 2628–2638. https://doi.org/10.1016/j.actamat.2013.01.042.

[50] W. Hume-Rothery, H.M. Powell, On the Theory of Super-Lattice Structures in Alloys, Zeitschrift Für Krist. - Cryst. Mater. 91 (1935) 23–47. https://doi.org/10.1524/zkri.1935.91.1.23.

[51] K.G. Pradeep, N. Wanderka, P. Choi, J. Banhart, B.S. Murty, D. Raabe, Atomic-scale compositional characterization of a nanocrystalline AlCrCuFeNiZn high-entropy alloy using atom probe tomography, Acta Mater. 61 (2013) 4696–4706. https://doi.org/10.1016/j.actamat.2013.04.059.

[52] S. Praveen, B.S. Murty, R.S. Kottada, Alloying behavior in multi-component AlCoCrCuFe and NiCoCrCuFe high entropy alloys, Mater. Sci. Eng. A. 534 (2012) 83–89. https://doi.org/10.1016/j.msea.2011.11.044.

[53] N.G. Jones, J.W. Aveson, A. Bhowmik, B.D. Conduit, H.J. Stone, On the entropic stabilisation of an Al0.5CrFeCoNiCu high entropy alloy, Intermetallics. 54 (2014) 148–153.

https://doi.org/10.1016/j.intermet.2014.06.004.

[54] M. Glienke, M. Vaidya, K. Gururaj, L. Daum, B. Tas, L. Rogal, K.G. Pradeep, S. V. Divinski, G. Wilde, Grain boundary diffusion in CoCrFeMnNi high entropy alloy: Kinetic hints towards a phase decomposition, Acta Mater. 195 (2020) 304–316. https://doi.org/10.1016/j.actamat.2020.05.009.

[55] S. Singh, N. Wanderka, B.S. Murty, U. Glatzel, J. Banhart, Decomposition in multi-component AlCoCrCuFeNi high-entropy alloy, Acta Mater. 59 (2011) 182–190. https://doi.org/10.1016/j.actamat.2010.09.023.

[56] B.E. MacDonald, Z. Fu, X. Wang, Z. Li, W. Chen, Y. Zhou, D. Raabe, J. Schoenung, H. Hahn, E.J. Lavernia, Influence of phase decomposition on mechanical behavior of an equiatomic CoCuFeMnNi high entropy alloy, Acta Mater. 181 (2019) 25–35. https://doi.org/10.1016/j.actamat.2019.09.030.

[57] E.J. Pickering, R. Muñoz-Moreno, H.J. Stone, N.G. Jones, Precipitation in the equiatomic high-entropy alloy CrMnFeCoNi, Scr. Mater. 113 (2016) 106–109. https://doi.org/10.1016/j.scriptamat.2015.10.025.

[58] F. Otto, A. Dlouhý, K.G. Pradeep, M. Kuběnová, D. Raabe, G. Eggeler, E.P. George, Decomposition of the single-phase high-entropy alloy CrMnFeCoNi after prolonged anneals at intermediate temperatures, Acta Mater. 112 (2016) 40–52. https://doi.org/10.1016/j.actamat.2016.04.005.

[59] E.J. Pickering, N.G. Jones, High-entropy alloys: a critical assessment of their founding principles and future prospects, Int. Mater. Rev. 61 (2016) 183–202. https://doi.org/10.1080/09506608.2016.1180020.

[60] Y.J. Li, A. Savan, A. Ludwig, Atomic scale understanding of phase stability

and decomposition of a nanocrystalline CrMnFeCoNi Cantor alloy, Appl. Phys. Lett. 119 (2021) 201910. https://doi.org/10.1063/5.0069107.

[61] I. Toda-Caraballo, A general formulation for solid solution hardening effect in multicomponent alloys, Scr. Mater. 127 (2017) 113–117. https://doi.org/10.1016/j.scriptamat.2016.09.009.

[62] C. Varvenne, A. Luque, W.A. Curtin, Theory of strengthening in fcc high entropy alloys, Acta Mater. 118 (2016) 164–176. https://doi.org/10.1016/j.actamat.2016.07.040.

[63] I. Toda-Caraballo, J.S. Wróbel, S.L. Dudarev, D. Nguyen-Manh, P.E.J. Rivera-Díaz-Del-Castillo, Interatomic spacing distribution in multicomponent alloys, Acta Mater. 97 (2015) 156–169. https://doi.org/10.1016/j.actamat.2015.07.010.

[64] S. Yoshida, T. Ikeuchi, T. Bhattacharjee, Y. Bai, A. Shibata, N. Tsuji, Effect of elemental combination on friction stress and Hall-Petch relationship in face-centered cubic high / medium entropy alloys, Acta Mater. 171 (2019) 201–215. https://doi.org/10.1016/j.actamat.2019.04.017.

[65] C. Lee, G. Song, M.C. Gao, R. Feng, P. Chen, J. Brechtl, Y. Chen, K. An, W. Guo, J.D. Poplawsky, S. Li, A.T. Samaei, W. Chen, A. Hu, H. Choo, P.K. Liaw, Lattice distortion in a strong and ductile refractory high-entropy alloy, Acta Mater. 160 (2018) 158–172. https://doi.org/10.1016/j.actamat.2018.08.053.

[66] J.W. Yeh, Recent progress in high-entropy alloys, Ann. Chim. Sci. Des Mater. 31 (2006) 633–648. https://doi.org/10.3166/acsm.31.633-648.

[67] K.Y. Tsai, M.H. Tsai, J.W. Yeh, Sluggish diffusion in Co-Cr-Fe-Mn-Ni high-entropy alloys, Acta Mater. 61 (2013) 4887–4897. https://doi.org/10.1016/j.actamat.2013.04.058.

[68] J. Dąbrowa, M. Danielewski, State-of-the-art diffusion studies in the high entropy alloys, Metals (Basel). 10 (2020). https://doi.org/10.3390/met10030347.

[69] S. V. Divinski, A. V. Pokoev, N. Esakkiraja, A. Paul, A Mystery of “Sluggish Diffusion” in High-Entropy Alloys: The Truth or a Myth?, Diffus. Found. 17 (2018) 69–104. https://doi.org/10.4028/www.scientific.net/df.17.69.

[70] A. Paul, Comments on “Sluggish diffusion in Co–Cr–Fe–Mn–Ni high-entropy alloys” by K.Y. Tsai, M.H. Tsai and J.W. Yeh, Acta Materialia 61 (2013) 4887–4897, Scr. Mater. 135 (2017) 153–157. https://doi.org/10.1016/j.scriptamat.2017.03.026.

[71] A. Durand, L. Peng, G. Laplanche, J.R. Morris, E.P. George, G. Eggeler, Interdiffusion in Cr–Fe–Co–Ni medium-entropy alloys, Intermetallics. 122 (2020). https://doi.org/10.1016/j.intermet.2020.106789.

[72] M. Vaidya, K.G. Pradeep, B.S. Murty, G. Wilde, S. V. Divinski, Bulk tracer diffusion in CoCrFeNi and CoCrFeMnNi high entropy alloys, Acta Mater. 146 (2018) 211–224. https://doi.org/10.1016/j.actamat.2017.12.052.

[73] Y. Zhang, Y.J. Zhou, J.P. Lin, G.L. Chen, P.K. Liaw, Solid-solution phase formation rules for multi-component alloys, Adv. Eng. Mater. 10 (2008) 534–538. https://doi.org/10.1002/adem.200700240.

[74] S. Guo, C.T. Liu, Phase stability in high entropy alloys: Formation of solid-

solution phase or amorphous phase, Prog. Nat. Sci. Mater. Int. 21 (2011) 433–446. https://doi.org/10.1016/S1002-0071(12)60080-X.

[75] Y. Zhang, T.T. Zuo, Z. Tang, M.C. Gao, K.A. Dahmen, P.K. Liaw, Z.P. Lu, Microstructures and properties of high-entropy alloys, Prog. Mater. Sci. 61 (2014) 1–93. https://doi.org/10.1016/j.pmatsci.2013.10.001.

[76] O.N. Senkov, D.B. Miracle, A new thermodynamic parameter to predict formation of solid solution or intermetallic phases in high entropy alloys, J. Alloys Compd. 658 (2016) 603–607. https://doi.org/10.1016/j.jallcom.2015.10.279.

[77] S. Guo, Phase selection rules for cast high entropy alloys: An overview, Mater. Sci. Technol. (United Kingdom). 31 (2015) 1223–1230. https://doi.org/10.1179/1743284715Y.0000000018.

[78] W. Cai, V. V. Bulatov, J. Chang, J. Li, S. Yip, Chapter 64 Dislocation core effects on mobility, in: Dislocations in Solids, Elsevier, 2004: pp. 1–80. https://doi.org/10.1016/S1572-4859(05)80003-8.

[79] R.L. Fleischer, Solution hardening, Acta Metall. 9 (1961) 996–1000. https://doi.org/10.1016/0001-6160(61)90242-5.

[80] R. Labusch, A Statistical Theory of Solid Solution Hardening, Phys. Status Solidi. 41 (1970) 659–669. https://doi.org/10.1002/pssb.19700410221.

[81] B. Yin, S. Yoshida, N. Tsuji, W.A. Curtin, Yield strength and misfit volumes of NiCoCr and implications for short-range-order, Nat. Commun. 11 (2020). https://doi.org/10.1038/s41467-020-16083-1.

[82] G. Taylor, The mechanism of plastic deformation of crystals. Part I.—

Theoretical, Proc. R. Soc. London. Ser. A, Contain. Pap. a Math. Phys. Character. 145 (1934) 362–387. https://doi.org/10.1098/rspa.1934.0106.

[83] E.O. Hall, The deformation and ageing of mild steel: III Discussion of results, Proc. Phys. Soc. Sect. B. 64 (1951) 747–753. https://doi.org/10.1088/0370-1301/64/9/303.

[84] N.J. Petch, The cleavage strength of polycrystals, J. Iron Steel InstInst. 174 (1953) 25–28.

[85] J.A. Venables, The martensite transformation in stainless steel, Philos. Mag. 7 (1962) 35–44. https://doi.org/10.1080/14786436208201856.

[86] M.A. Meyers, A. Mishra, D.J. Benson, Mechanical properties of nanocrystalline materials, Prog. Mater. Sci. 51 (2006) 427–556. https://doi.org/10.1016/j.pmatsci.2005.08.003.

[87] M. Dao, L. Lu, R.J. Asaro, J.T.M. De Hosson, E. Ma, Toward a quantitative understanding of mechanical behavior of nanocrystalline metals, Acta Mater. 55 (2007) 4041–4065. https://doi.org/10.1016/j.actamat.2007.01.038.

[88] H. Van Swygenhoven, P.M. Derlet, Grain-boundary sliding in nanocrystalline fcc metals, Phys. Rev. B - Condens. Matter Mater. Phys. 64 (2001) 224105. https://doi.org/10.1103/PhysRevB.64.224105.

[89] J. Schiøtz, F.D. Di Tolla, K.W. Jacobsen, Softening of nanocrystalline metals at very small grain sizes, Nature. 391 (1998) 561–563. https://doi.org/10.1038/35328.

[90] K.M. Youssef, R.O. Scattergood, K.L. Murty, J.A. Horton, C.C. Koch, Ultrahigh strength and high ductility of bulk nanocrystalline copper, Appl.

Phys. Lett. 87 (2005) 91904. https://doi.org/10.1063/1.2034122.

[91] K.S. Kumar, S. Suresh, M.F. Chisholm, J.A. Horton, P. Wang, Deformation of electrodeposited nanocrystalline nickel, Acta Mater. 51 (2003) 387–405. https://doi.org/10.1016/S1359-6454(02)00421-4.

[92] J.D. Eshelby, F.C. Frank, F.R.N. Nabarro, XLI. The equilibrium of linear arrays of dislocations., London, Edinburgh, Dublin Philos. Mag. J. Sci. 42 (1951) 351–364. https://doi.org/10.1080/14786445108561060.

[93] M.F. Ashby, The deformation of plastically non-homogeneous materials, Philos. Mag. 21 (1970) 399–424. https://doi.org/10.1080/14786437008238426.

[94] Y. Li, A.J. Bushby, D.J. Dunstan, The Hall-Petch effect as a manifestation of the general size effect, Proc. R. Soc. A Math. Phys. Eng. Sci. 472 (2016). https://doi.org/10.1098/rspa.2015.0890.

[95] D.J. Dunstan, A.J. Bushby, Grain size dependence of the strength of metals: The Hall-Petch effect does not scale as the inverse square root of grain size, Int. J. Plast. 53 (2014) 56–65. https://doi.org/10.1016/j.ijplas.2013.07.004.

[96] D. Chen, F. He, B. Han, Q. Wu, Y. Tong, Y. Zhao, Z. Wang, J. Wang, J. jung Kai, Synergistic effect of Ti and Al on L12-phase design in CoCrFeNi-based high entropy alloys, Intermetallics. 110 (2019) 106476. https://doi.org/10.1016/j.intermet.2019.106476.

[97] Y.J. Liang, L. Wang, Y. Wen, B. Cheng, Q. Wu, T. Cao, Q. Xiao, Y. Xue, G. Sha, Y. Wang, Y. Ren, X. Li, L. Wang, F. Wang, H. Cai, High-content ductile coherent nanoprecipitates achieve ultrastrong high-entropy alloys, Nat.

Commun. 9 (2018) 1–8. https://doi.org/10.1038/s41467-018-06600-8.

[98] Y.L. Zhao, T. Yang, Y.R. Li, L. Fan, B. Han, Z.B. Jiao, D. Chen, C.T. Liu, J.J. Kai, Superior high-temperature properties and deformation-induced planar faults in a novel L12-strengthened high-entropy alloy, Acta Mater. 188 (2020) 517–527. https://doi.org/10.1016/j.actamat.2020.02.028.

[99] T. Yang, Y. Zhao, W. Liu, J. Kai, C. Liu, L12-strengthened high-entropy alloys for advanced structural applications, J. Mater. Res. 33 (2018) 2983–2997. https://doi.org/10.1557/jmr.2018.186.

[100] Y.C. Huang, C.S. Tsao, C. Lin, Y.C. Lai, S.K. Wu, C.H. Chen, Evolution of Guinier-Preston zones in cold-rolled Al0.2CoCrFeNi high-entropy alloy studied by synchrotron small-angle X-ray scattering, Mater. Sci. Eng. A. 769 (2020) 138526. https://doi.org/10.1016/j.msea.2019.138526.

[101] B. Gwalani, V. Soni, D. Choudhuri, M. Lee, J.Y. Hwang, S.J. Nam, H. Ryu, S.H. Hong, R. Banerjee, Stability of ordered L12 and B2 precipitates in face centered cubic based high entropy alloys - Al0.3CoFeCrNi and Al0.3CuFeCrNi2, Scr. Mater. 123 (2016) 130–134. https://doi.org/10.1016/j.scriptamat.2016.06.019.

[102] D. Hull, D.J. Bacon, Introduction to Dislocations, Fifth Edition, Elsevier, 2011. https://doi.org/10.1016/C2009-0-64358-0.

[103] E. Aerts, P. Delavignette, R. Siems, S. Amelinckx, Stacking fault energy in silicon, J. Appl. Phys. 33 (1962) 3078–3080. https://doi.org/10.1063/1.1728570.

[104] H. Saka, Y. Sueki, T. Imura, On the intrinsic temperature dependence of the

stacking-fault energy in copper-aluminium alloys, Philos. Mag. A Phys. Condens. Matter, Struct. Defects Mech. Prop. 37 (1978) 273–289. https://doi.org/10.1080/01418617808235440.

[105] H. Saka, T. Kondo, T. Imura, The temperature dependence of the stacking-fault energy in silver-base alloys, Philos. Mag. A Phys. Condens. Matter, Struct. Defects Mech. Prop. 47 (1983) 859–868. https://doi.org/10.1080/01418618308243125.

[106] R. Xiong, H. Peng, S. Wang, H. Si, Y. Wen, Effect of stacking fault energy on work hardening behaviors in Fe-Mn-Si-C high manganese steels by varying silicon and carbon contents, Mater. Des. 85 (2015) 707–714. https://doi.org/10.1016/j.matdes.2015.07.072.

[107] A. Rohatgi, K.S. Vecchio, G.T. Gray, The influence of stacking fault energy on the mechanical behavior of Cu and Cu-al alloys: Deformation twinning, work hardening, and dynamic recovery, Metall. Mater. Trans. A Phys. Metall. Mater. Sci. 32 (2001) 135–145. https://doi.org/10.1007/s11661-001-0109-7.

[108] D. Molnár, X. Sun, S. Lu, W. Li, G. Engberg, L. Vitos, Effect of temperature on the stacking fault energy and deformation behaviour in 316L austenitic stainless steel, Mater. Sci. Eng. A. 759 (2019) 490–497. https://doi.org/10.1016/j.msea.2019.05.079.

[109] M. Naeem, H. He, S. Harjo, T. Kawasaki, W. Lin, J.J. Kai, Z. Wu, S. Lan, X.L. Wang, Temperature-dependent hardening contributions in CrFeCoNi high-entropy alloy, Acta Mater. 221 (2021) 117371. https://doi.org/10.1016/j.actamat.2021.117371.

[110] M. Kang, W. Woo, Y.K. Lee, B.S. Seong, Neutron diffraction analysis of

stacking fault energy in Fe-18Mn-2Al-0.6C twinning-induced plasticity steels, Mater. Lett. 76 (2012) 93–95. https://doi.org/10.1016/j.matlet.2012.02.075.

[111] W. Woo, M. Naeem, J.S. Jeong, C.M. Lee, S. Harjo, T. Kawasaki, H. He, X.L. Wang, Comparison of dislocation density, twin fault probability, and stacking fault energy between CrCoNi and CrCoNiFe medium entropy alloys deformed at 293 and 140K, Mater. Sci. Eng. A. 781 (2020) 139224. https://doi.org/10.1016/j.msea.2020.139224.

[112] L. Tang, K. Yan, B. Cai, Y. Wang, B. Liu, S. Kabra, M.M. Attallah, Y. Liu, Deformation mechanisms of FeCoCrNiMo0.2 high entropy alloy at 77 and 15 K, Scr. Mater. 178 (2020) 166–170. https://doi.org/10.1016/j.scriptamat.2019.11.026.

[113] Y. Wang, B. Liu, K. Yan, M. Wang, S. Kabra, Y.L. Chiu, D. Dye, P.D. Lee, Y. Liu, B. Cai, Probing deformation mechanisms of a FeCoCrNi high-entropy alloy at 293 and 77 K using in situ neutron diffraction, Acta Mater. 154 (2018) 79–89. https://doi.org/10.1016/j.actamat.2018.05.013.

[114] J.S. Jeong, W. Woo, K.H. Oh, S.K. Kwon, Y.M. Koo, In situ neutron diffraction study of the microstructure and tensile deformation behavior in Al-added high manganese austenitic steels, Acta Mater. 60 (2012) 2290–2299. https://doi.org/10.1016/j.actamat.2011.12.043.

[115] T.H. Lee, C.S. Oh, S.J. Kim, Effects of nitrogen on deformation-induced martensitic transformation in metastable austenitic Fe-18Cr-10Mn-N steels, Scr. Mater. 58 (2008) 110–113. https://doi.org/10.1016/j.scriptamat.2007.09.029.

[116] J.K. Kim, B.C. De Cooman, Stacking fault energy and deformation

mechanisms in Fe-xMn-0.6C-yAl TWIP steel, Mater. Sci. Eng. A. 676 (2016) 216–231. https://doi.org/10.1016/j.msea.2016.08.106.

[117] S. Allain, J.-P.P. Chateau, O. Bouaziz, A physical model of the twinning-induced plasticity effect in a high manganese austenitic steel, Mater. Sci. Eng. A. 387–389 (2004) 143–147. https://doi.org/10.1016/j.msea.2004.01.060.

[118] O. Bouaziz, N. Guelton, Modelling of TWIP effect on work-hardening, Mater. Sci. Eng. A. 319–321 (2001) 246–249. https://doi.org/10.1016/S0921-5093(00)02019-0.

[119] M. Schneider, G. Laplanche, Effects of temperature on mechanical properties and deformation mechanisms of the equiatomic CrFeNi medium-entropy alloy, Acta Mater. 204 (2021) 116470. https://doi.org/10.1016/j.actamat.2020.11.012.

[120] G. Laplanche, A. Kostka, O.M. Horst, G. Eggeler, E.P. George, Microstructure evolution and critical stress for twinning in the CrMnFeCoNi high-entropy alloy, Acta Mater. 118 (2016) 152–163. https://doi.org/10.1016/j.actamat.2016.07.038.

[121] S.F. Liu, Y. Wu, H.T. Wang, W.T. Lin, Y.Y. Shang, J.B. Liu, K. An, X.J. Liu, H. Wang, Z.P. Lu, Transformation-reinforced high-entropy alloys with superior mechanical properties via tailoring stacking fault energy, J. Alloys Compd. 792 (2019) 444–455. https://doi.org/10.1016/j.jallcom.2019.04.035.

[122] D. Wei, X. Li, W. Heng, Y. Koizumi, F. He, W.M. Choi, B.J. Lee, H.S. Kim, H. Kato, A. Chiba, Novel Co-rich high entropy alloys with superior tensile properties, Mater. Res. Lett. 7 (2019) 82–88.

https://doi.org/10.1080/21663831.2018.1553803.

[123] G. (Orsay) Fontaine, No Title, University of Orsay, 1968.

[124] J.A. Venables, Deformation twinning in face-centred cubic metals, Philos. Mag. 6 (1961) 379–396. https://doi.org/10.1080/14786436108235892.

[125] J.B. Cohen, J. Weertman, A dislocation model for twinning in f.c.c. metals, Acta Metall. 11 (1963) 996–998. https://doi.org/10.1016/0001-6160(63)90074-9.

[126] S. Mahajan, G.Y. Chin, Formation of deformation twins in f.c.c. crystals, Acta Metall. 21 (1973) 1353–1363. https://doi.org/10.1016/0001-6160(73)90085-0.

[127] S.M. Copley, B.H. Kear, The dependence of the width of a dissociated dislocation on dislocation velocity, Acta Metall. 16 (1968) 227–231. https://doi.org/10.1016/0001-6160(68)90118-1.

[128] T.S. Byun, On the stress dependence of partial dislocation separation and deformation microstructure in austenitic stainless steels, Acta Mater. 51 (2003) 3063–3071. https://doi.org/10.1016/S1359-6454(03)00117-4.

[129] B.C. De Cooman, Y. Estrin, S.K. Kim, Twinning-induced plasticity (TWIP) steels, Acta Mater. 142 (2018) 283–362. https://doi.org/10.1016/j.actamat.2017.06.046.

[130] N. Narita, J. Takamura, Deformation twinning in silver- and copper-alloy crystals, Philos. Mag. 29 (1974) 1001–1028. https://doi.org/10.1080/14786437408226586.

[131] H. Suzuki, C.S. Barrett, Deformation twinning in silver-gold alloys, Acta

Metall. 6 (1958) 156–165. https://doi.org/10.1016/0001-6160(58)90002-6.

[132] B. Mahato, T. Sahu, S.K. Shee, P. Sahu, T. Sawaguchi, J. Kömi, L.P. Karjalainen, Simultaneous twinning nucleation mechanisms in an Fe–Mn–Si–Al twinning induced plasticity steel, Acta Mater. 132 (2017) 264–275. https://doi.org/10.1016/j.actamat.2017.04.046.

[133] M.A. Meyers, O. Vöhringer, V.A. Lubarda, The onset of twinning in metals: A constitutive description, Acta Mater. 49 (2001) 4025–4039. https://doi.org/10.1016/S1359-6454(01)00300-7.

[134] I. Gutierrez-Urrutia, S. Zaefferer, D. Raabe, The effect of grain size and grain orientation on deformation twinning in a Fe-22wt.% Mn-0.6wt.% C TWIP steel, Mater. Sci. Eng. A. 527 (2010) 3552–3560. https://doi.org/10.1016/j.msea.2010.02.041.

[135] D.R. Steinmetz, T. Jäpel, B. Wietbrock, P. Eisenlohr, I. Gutierrez-Urrutia, A. Saeed-Akbari, T. Hickel, F. Roters, D. Raabe, A. Saeed–Akbari, T. Hickel, F. Roters, D. Raabe, Revealing the strain-hardening behavior of twinning-induced plasticity steels: Theory, simulations, experiments, Acta Mater. 61 (2013) 494–510. https://doi.org/10.1016/j.actamat.2012.09.064.

[136] S. Lu, X. Sun, Y. Tian, X. An, W. Li, Y. Chen, H. Zhang, L. Vitos, Theory of transformation-mediated twinning, PNAS Nexus. 2 (2023) 1–11. https://doi.org/10.1093/pnasnexus/pgac282.

[137] Z. Nishiyama, Martensitic transformation, Academic Press, 1978.

[138] M. Villa, M.F. Hansen, M.A.J. Somers, Martensite formation in Fe-C alloys at cryogenic temperatures, Scr. Mater. 141 (2017) 129–132.

https://doi.org/10.1016/j.scriptamat.2017.08.005.

[139] M. Villa, M.A.J. Somers, On the Role of Isothermal Martensite Formation during Cryogenic Treatment of Steels, HTM - J. Heat Treat. Mater. 75 (2020) 263–286. https://doi.org/10.3139/105.110420.

[140] G.B. Olson, M. Cohen, A mechanism for the strain-induced nucleation of martensitic transformations, J. Less-Common Met. 28 (1972) 107–118. https://doi.org/10.1016/0022-5088(72)90173-7.

[141] J.R.R. Patel, M. Cohen, Criterion for the action of applied stress in the martensitic transformation, Acta Metall. 1 (1953) 531–538. https://doi.org/10.1016/0001-6160(53)90083-2.

[142] P. MANGONON, THOMAS G, MARTENSITE PHASES IN 304 STAINLESS STEEL, Met Trans. 1 (1970) 1577–1586. https://doi.org/10.1007/bf02642003.

[143] A. Das, S. Sivaprasad, M. Ghosh, P.C. Chakraborti, S. Tarafder, Morphologies and characteristics of deformation induced martensite during tensile deformation of 304 LN stainless steel, Mater. Sci. Eng. A. 486 (2008) 283–286. https://doi.org/10.1016/j.msea.2007.09.005.

[144] J. Talonen, H. Hänninen, Formation of shear bands and strain-induced martensite during plastic deformation of metastable austenitic stainless steels, Acta Mater. 55 (2007) 6108–6118. https://doi.org/10.1016/j.actamat.2007.07.015.

[145] A.J. Bogers, W.G. Burgers, Partial dislocations on the {110} planes in the B.C.C. lattice and the transition of the F.C.C. into the B.C.C. lattice, Acta

Metall. 12 (1964) 255–261. https://doi.org/10.1016/0001-6160(64)90194-4.

[146] H. Schumann, Bildung von α-Martensit im Schnittbereich von ϵ-Martensitplatten, Krist. Und Tech. 12 (1977) 363–370. https://doi.org/10.1002/crat.19770120405.

[147] L. BRACKE, L. KESTENS, J. PENNING, Transformation mechanism of α′-martensite in an austenitic Fe–Mn–C–N alloy, Scr. Mater. 57 (2007) 385–388. https://doi.org/10.1016/j.scriptamat.2007.05.003.

[148] G. Kurdjumov, G., Sachs, Über den Mechanismus der Stahlhärtung, Ann. Phys. 416 (1935) 609–635. https://doi.org/10.1002/andp.19354160704.

[149] G. Wassermann, Influence of the α-γ transformation of an irreversible Ni steel onto crystal orientation and tensile strength, Eisenhütte. 16 (1933).

[150] M.J. Whelan, Dislocation interactions in face-centred cubic metals, with particular reference to stainless steel, Proc. R. Soc. London. Ser. A. Math. Phys. Sci. 249 (1959) 114–137. https://doi.org/10.1098/rspa.1959.0011.

[151] P.C.J. Gallagher, Stacking-fault energy in dilute silver alloys from extended node measurements, J. Appl. Phys. 39 (1968) 160–162. https://doi.org/10.1063/1.1655725.

[152] D.J.H. Cockayne, I.L.F. Ray, M.J. Whelan, Investigations of dislocation strain fields using weak beams, Philos. Mag. 20 (1969) 1265–1270. https://doi.org/10.1080/14786436908228210.

[153] D.J.H. Cockayne, M.L. Jenkins, I.L.F. Ray, The measurement of stacking-fault energies of pure face-centred cubic metals, Philos. Mag. 24 (1971) 1383–1392. https://doi.org/10.1080/14786437108217419.

[154] G. Laplanche, A. Kostka, C. Reinhart, J. Hunfeld, G. Eggeler, E.P. George, Reasons for the superior mechanical properties of medium-entropy CrCoNi compared to high-entropy CrMnFeCoNi, Acta Mater. 128 (2017) 292–303. https://doi.org/10.1016/j.actamat.2017.02.036.

[155] D.J.H. Cockayne, V. Vitek, Effect of Core Structure on the Determination of the Stacking-Fault Energy in Close-Packed Metals, Phys. Status Solidi. 65 (1974) 751–764. https://doi.org/10.1002/pssb.2220650236.

[156] C. Wagner, A. Ferrari, J. Schreuer, J.P. Couzinié, Y. Ikeda, F. Körmann, G. Eggeler, E.P. George, G. Laplanche, Effects of Cr/Ni ratio on physical properties of Cr-Mn-Fe-Co-Ni high-entropy alloys, Acta Mater. 227 (2022) 117693. https://doi.org/10.1016/j.actamat.2022.117693.

[157] R.P. Reed, R.E. Schramm, Relationship between stacking-fault energy and x-ray measurements of stacking-fault probability and microstrain, J. Appl. Phys. 45 (1974) 4705–4711. https://doi.org/10.1063/1.1663122.

[158] H.M. Otte, Measurement of stacking-fault energies by x-ray diffraction, J. Appl. Phys. 38 (1967) 217–222. https://doi.org/10.1063/1.1708958.

[159] R.P.I. Adler, H.M. Otte, Dislocation configurations in wire-drawn polycrystalline copper alloys: A study by X-ray diffraction, Mater. Sci. Eng. 1 (1966) 222–238. https://doi.org/10.1016/0025-5416(66)90034-6.

[160] R.E. Smallman, K.H. Westmacott, Stacking faults in face-centred cubic metals and alloys, Philos. Mag. 2 (1957) 669–683. https://doi.org/10.1080/14786435708242709.

[161] B. Warren, X-ray Diffraction, 1990.

[162] G.K. Williamson, W.H. Hall, X-ray line broadening from filed aluminium and wolfram, Acta Metall. 1 (1953) 22–31. https://doi.org/10.1016/0001-6160(53)90006-6.

[163] T. Ungár, A. Borbély, The effect of dislocation contrast on x-ray line broadening: A new approach to line profile analysis, Appl. Phys. Lett. 69 (1996) 3173–3175. https://doi.org/10.1063/1.117951.

[164] B.E. Warren, B.L. Averbach, The separation of stacking fault broadening in cold-worked metals [9], J. Appl. Phys. 23 (1952) 1059. https://doi.org/10.1063/1.1702352.

[165] G. Ribárik, J. Gubicza, T. Ungár, Correlation between strength and microstructure of ball-milled Al-Mg alloys determined by X-ray diffraction, Mater. Sci. Eng. A. 387–389 (2004) 343–347. https://doi.org/10.1016/j.msea.2004.01.089.

[166] M. Wilkens, The determination of density and distribution of dislocations in deformed single crystals from broadened X-ray diffraction profiles, Phys. Status Solidi. 2 (1970) 359–370. https://doi.org/10.1002/pssa.19700020224.

[167] T. Ungár, I. Dragomir, Á. Révész, A. Borbély, The contrast factors of dislocations in cubic crystals: the dislocation model of strain anisotropy in practice, Urn:Issn:0021-8898. 32 (1999) 992–1002. https://doi.org/10.1107/S0021889899009334.

[168] T. Ungár, Microstructural parameters from X-ray diffraction peak broadening, Scr. Mater. 51 (2004) 777–781. https://doi.org/10.1016/j.scriptamat.2004.05.007.

[169] W. Li, S. Lu, Q.M. Hu, S.K. Kwon, B. Johansson, L. Vitos, Generalized stacking fault energies of alloys, J. Phys. Condens. Matter. 26 (2014) 265005. https://doi.org/10.1088/0953-8984/26/26/265005.

[170] D.T. Pierce, J.A. Jiménez, J. Bentley, D. Raabe, C. Oskay, J.E. Wittig, The influence of manganese content on the stacking fault and austenite/ε-martensite interfacial energies in Fe-Mn-(Al-Si) steels investigated by experiment and theory, Acta Mater. 68 (2014) 238–253. https://doi.org/10.1016/j.actamat.2014.01.001.

[171] A. Dumay, J.P. Chateau, S. Allain, S. Migot, O. Bouaziz, Influence of addition elements on the stacking-fault energy and mechanical properties of an austenitic Fe-Mn-C steel, Mater. Sci. Eng. A. 483–484 (2008) 184–187. https://doi.org/10.1016/j.msea.2006.12.170.

[172] Z. Dong, S. Schönecker, D. Chen, W. Li, S. Lu, L. Vitos, Influence of Mn content on the intrinsic energy barriers of paramagnetic FeMn alloys from longitudinal spin fluctuation theory, Int. J. Plast. 119 (2019) 123–139. https://doi.org/10.1016/j.ijplas.2019.02.020.

[173] H. SUZUKI, Chemical Interaction of Solute Atoms with Dislocations, Sci. Reports Res. Institutes, Tohoku Univ. Ser. A, Physics, Chem. Metall. 4 (1952) 455–463. https://core.ac.uk/reader/235854030 (accessed May 23, 2023).

[174] H. Suzuki, Segregation of solute atoms to stacking faults, J. Phys. Soc. Japan. 17 (1962) 322–325. https://doi.org/10.1143/JPSJ.17.322.

[175] J.O. Andersson, T. Helander, L. Höglund, P. Shi, B. Sundman, Thermo-Calc & DICTRA, computational tools for materials science, Calphad Comput.

Coupling Phase Diagrams Thermochem. 26 (2002) 273–312. https://doi.org/10.1016/S0364-5916(02)00037-8.

[176] A.T. Dinsdale, SGTE data for pure elements, Calphad. 15 (1991) 317–425. https://doi.org/10.1016/0364-5916(91)90030-N.

[177] S. Bigdeli, H. Ehtehsami, Q. Chen, H. Mao, P. Korzhavy, M. Selleby, New description of metastable hcp phase for unaries Fe and Mn: Coupling between first-principles calculations and CALPHAD modeling, Phys. Status Solidi Basic Res. 253 (2016) 1830–1836. https://doi.org/10.1002/pssb.201600096.

[178] S. Bigdeli, M. Selleby, A thermodynamic assessment of the binary Fe-Mn system for the third generation of Calphad databases, Calphad Comput. Coupling Phase Diagrams Thermochem. 64 (2019) 185–195. https://doi.org/10.1016/j.calphad.2018.11.011.

[179] G. Kresse, J. Furthmüller, Efficient iterative schemes for ab initio total-energy calculations using a plane-wave basis set, Phys. Rev. B - Condens. Matter Mater. Phys. 54 (1996) 11169–11186. https://doi.org/10.1103/PhysRevB.54.11169.

[180] G. Kresse, J. Hafner, Ab initio molecular dynamics for liquid metals, Phys. Rev. B. 47 (1993) 558–561. https://doi.org/10.1103/PhysRevB.47.558.

[181] P. Soven, Coherent-potential model of substitutional disordered alloys, Phys. Rev. 156 (1967) 809–813. https://doi.org/10.1103/PhysRev.156.809.

[182] L. Vitos, I.A. Abrikosov, B. Johansson, Anisotropic lattice distortions in random alloys from first-principles theory, Phys. Rev. Lett. 87 (2001) 156401-

156401–4. https://doi.org/10.1103/PhysRevLett.87.156401.

[183] L. Vitos, Computational Quantum Mechanics for Materials Engineers, Springer London, 2007. https://doi.org/10.1007/978-1-84628-951-4.

[184] M. Jahnátek, J. Hafner, M. Krajčí, Shear deformation, ideal strength, and stacking fault formation of fcc metals: A density-functional study of Al and Cu, Phys. Rev. B - Condens. Matter Mater. Phys. 79 (2009) 224103. https://doi.org/10.1103/PhysRevB.79.224103.

[185] P.J.H. Denteneer, W. Van Haeringen, Stacking-fault energies in semiconductors from first-principles calculations, J. Phys. C Solid State Phys. 20 (1987) L883–L887. https://doi.org/10.1088/0022-3719/20/32/001.

[186] C. Cheng, R.J. Needs, V. Heine, Inter-layer interactions and the origin of sic polytypes, J. Phys. C Solid State Phys. 21 (1988) 1049–1063. https://doi.org/10.1088/0022-3719/21/6/012.

[187] L. Vitos, J.O. Nilsson, B. Johansson, Alloying effects on the stacking fault energy in austenitic stainless steels from first-principles theory, Acta Mater. 54 (2006) 3821–3826. https://doi.org/10.1016/j.actamat.2006.04.013.

[188] T. Yonezawa, K. Suzuki, S. Ooki, A. Hashimoto, The effect of chemical composition and heat treatment conditions on stacking fault energy for Fe-Cr-Ni austenitic stainless steel, Metall. Mater. Trans. A Phys. Metall. Mater. Sci. 44 (2013) 5884–5896. https://doi.org/10.1007/s11661-013-1943-0.

[189] W. Li, S. Lu, Q.M. Hu, B. Johansson, S.K. Kwon, M. Grehk, J.Y. Johnsson, L. Vitos, Generalized stacking fault energy of γ-Fe, Philos. Mag. 96 (2016) 524–541. https://doi.org/10.1080/14786435.2016.1140912.

[190] B. Nending, O.I. Gorbatov, J.-C.C. Tseng, P. Hedström, In Situ Bulk Observations and Ab Initio Calculations Revealing the Temperature Dependence of Stacking Fault Energy in Fe–Cr–Ni Alloys, Metall. Mater. Trans. A Phys. Metall. Mater. Sci. 52 (2021) 5357–5366. https://doi.org/10.1007/s11661-021-06473-5.

[191] L. Rémy, A. Pineau, B. Thomas, Temperature dependence of stacking fault energy in close-packed metals and alloys, Mater. Sci. Eng. 36 (1978) 47–63. https://doi.org/10.1016/0025-5416(78)90194-5.

[192] R.M. Latanision, A.W. Ruff, The temperature dependence of stacking fault energy in Fe-Cr-Ni alloys, Metall. Trans. 2 (1971) 505–509. https://doi.org/10.1007/BF02663341.

[193] X. Zhang, B. Grabowski, F. Körmann, A. V. Ruban, Y. Gong, R.C. Reed, T. Hickel, J. Neugebauer, Temperature dependence of the stacking-fault Gibbs energy for Al, Cu, and Ni, Phys. Rev. B. 98 (2018) 224106. https://doi.org/10.1103/PhysRevB.98.224106.

[194] S. Curtze, V.T. Kuokkala, A. Oikari, J. Talonen, H. Hänninen, Thermodynamic modeling of the stacking fault energy of austenitic steels, Acta Mater. 59 (2011) 1068–1076. https://doi.org/10.1016/j.actamat.2010.10.037.

[195] A. Linda, P.K. Tripathi, S. Nagar, S. Bhowmick, Effect of pressure on stacking fault energy and deformation behavior of face-centered cubic metals, Materialia. 26 (2022) 101598. https://doi.org/10.1016/j.mtla.2022.101598.

[196] J.X. Yan, Z.J. Zhang, H. Yu, K.Q. Li, Q.M. Hu, J.B. Yang, Z.F. Zhang, Effects

of pressure on the generalized stacking fault energy and twinning propensity of face-centered cubic metals, J. Alloys Compd. 866 (2021) 158869. https://doi.org/10.1016/j.jallcom.2021.158869.

[197] J.S. Hong, S.M. Choi, Y.K. Lee, Stasis mechanism of γ → ε martensitic transformation in Fe-17Mn alloy, Acta Mater. 210 (2021) 116846. https://doi.org/10.1016/j.actamat.2021.116846.

[198] J. Chen, F.T. Dong, Z.Y. Liu, G.D. Wang, Grain size dependence of twinning behaviors and resultant cryogenic impact toughness in high manganese austenitic steel, J. Mater. Res. Technol. 10 (2021) 175–187. https://doi.org/10.1016/j.jmrt.2020.12.030.

[199] S.J. Lee, K. Ushioda, H. Fujii, Evaluation of stacking-fault energy in Fe-Mn based twinning-induced plasticity steels after friction stir welding, Mater. Charact. 147 (2019) 379–383. https://doi.org/10.1016/j.matchar.2018.11.024.

[200] S.M.S.S.J. Lee, S.M.S.S.J. Lee, S.M.S.S.J. Lee, J.H. Nam, Y.K. Lee, Tensile properties and deformation mode of Si-added Fe-18Mn-0.6C steels, Acta Mater. 144 (2018) 738–747. https://doi.org/10.1016/j.actamat.2017.11.023.

[201] Y. Lee, C. Choi, Driving Force for g → « Martensitic Transformation and SFE of austenite in Fe-Mn binary system, Metall. Mater. Trans. A. 31A (2000) 355–360. https://doi.org/https://doi.org/10.1007/s11661-000-0271-3.

[202] J.Y. Lee, J.S. Hong, S.H. Kang, Y.K. Lee, The effect of austenite grain size on deformation mechanism of Fe–17Mn steel, Mater. Sci. Eng. A. 809 (2021) 140972. https://doi.org/10.1016/j.msea.2021.140972.

[203] J. Lu, L. Hultman, E. Holmström, K.H. Antonsson, M. Grehk, W. Li, L. Vitos, A. Golpayegani, Stacking fault energies in austenitic stainless steels, Acta Mater. 111 (2016) 39–46. https://doi.org/10.1016/j.actamat.2016.03.042.

[204] Z. Dong, W. Li, G. Chai, L. Vitos, Strong temperature – Dependence of Ni - alloying influence on the stacking fault energy in austenitic stainless steel, Scr. Mater. 178 (2020) 438–441. https://doi.org/10.1016/j.scriptamat.2019.12.013.

[205] D. Molnár, Stacking fault energy and deformation behaviour of austenitic stainless steels : a joint theoretical-experimental study, KTH, 2019. http://www.diva-portal.org/smash/record.jsf?pid=diva2%3A1375603&dswid=2610 (accessed May 24, 2023).

[206] X. Sun, S. Lu, R. Xie, X. An, W. Li, T. Zhang, C. Liang, X. Ding, Y. Wang, H. Zhang, L. Vitos, Can experiment determine the stacking fault energy of metastable alloys?, Mater. Des. 199 (2021) 109396. https://doi.org/10.1016/j.matdes.2020.109396.

[207] S. Lu, Q.M. Hu, B. Johansson, L. Vitos, Stacking fault energies of Mn, Co and Nb alloyed austenitic stainless steels, Acta Mater. 59 (2011) 5728–5734. https://doi.org/10.1016/j.actamat.2011.05.049.

[208] T. Ericsson, The temperature and concentration dependence of the stacking fault energy in the Co-Ni system, Acta Metall. 14 (1966) 853–865. https://doi.org/10.1016/0001-6160(66)90006-X.

[209] Y.U.N. Velosevich, P. U., Gridnev, V. N., Petrov, Influence of Mn and the stacking fault energy of Fe-Mn alloy, Phys. Met. Metallogr. (1976).

[210] R. Xiong, H. Peng, H. Si, W. Zhang, Y. Wen, Thermodynamic calculation of stacking fault energy of the Fe-Mn-Si-C high manganese steels, Mater. Sci. Eng. A. 598 (2014) 376–386. https://doi.org/10.1016/j.msea.2014.01.046.

[211] O.A. Zambrano, Stacking fault energy maps of Fe-Mn-Al-C-Si steels: Effect of temperature, grain size, and variations in compositions, J. Eng. Mater. Technol. Trans. ASME. 138 (2016) 1–9. https://doi.org/10.1115/1.4033632.

[212] Y.W. Choi, Z. Dong, W. Li, S. Schönecker, H. Kim, S.K. Kwon, L. Vitos, Predicting the stacking fault energy of austenitic Fe-Mn-Al (Si) alloys, Mater. Des. 187 (2020) 108392. https://doi.org/10.1016/j.matdes.2019.108392.

[213] G.R. Lehnhoff, K.O. Findley, B.C. De Cooman, The influence of silicon and aluminum alloying on the lattice parameter and stacking fault energy of austenitic steel, Scr. Mater. 92 (2014) 19–22. https://doi.org/10.1016/j.scriptamat.2014.07.019.

[214] X. Tian, Y. Zhang, Effect of Si content on the stacking fault energy in γ-Fe-Mn-Si-C alloys: Part I. X-ray diffraction line profile analysis, Mater. Sci. Eng. A. 516 (2009) 73–77. https://doi.org/10.1016/j.msea.2009.02.031.

[215] W. Charnock, J. Nutting, The Effect of Carbon and Nickel upon the Stacking-Fault Energy of Iron, Met. Sci. J. 1 (1967) 123–127. https://doi.org/10.1179/msc.1967.1.1.123.

[216] Y.N. Petrov, Effect of carbon and nitrogen on the stacking fault energy of high-alloyed iron-based austenite, Int. J. Mater. Res. 94 (2022) 1012–1016. https://doi.org/10.1515/ijmr-2003-0183.

[217] B. Wang, C. Hong, G. Winther, T.L. Christiansen, M.A.J. Somers,

Deformation mechanisms in meta-stable and nitrogen-stabilized austenitic stainless steel during severe surface deformation, Materialia. 12 (2020). https://doi.org/10.1016/j.mtla.2020.100751.

[218] F. Niessen, W. Li, K. V. Werner, S. Lu, L. Vitos, M. Villa, M.A.J. Somers, Ab initio study of the effect of interstitial alloying on the intrinsic stacking fault energy of paramagnetic γ-Fe and austenitic stainless steel, Acta Mater. (2023) 118967. https://doi.org/10.1016/J.ACTAMAT.2023.118967.

[219] F. Zhang, Y. Wu, H. Lou, Z. Zeng, V.B. Prakapenka, E. Greenberg, Y. Ren, J. Yan, J.S. Okasinski, X. Liu, Y. Liu, Q. Zeng, Z. Lu, Polymorphism in a high-entropy alloy, Nat. Commun. 8 (2017). https://doi.org/10.1038/ncomms15687.

[220] Y.F. Shen, N. Jia, Y.D. Wang, X. Sun, L. Zuo, D. Raabe, Suppression of twinning and phase transformation in an ultrafine grained 2 GPa strong metastable austenitic steel: Experiment and simulation, Acta Mater. 97 (2015) 305–315. https://doi.org/10.1016/j.actamat.2015.06.053.

[221] S.W. Wu, G. Wang, J. Yi, Y.D. Jia, I. Hussain, Q.J. Zhai, P.K. Liaw, Strong grain-size effect on deformation twinning of an Al0.1CoCrFeNi high-entropy alloy, Mater. Res. Lett. 5 (2017) 276–283. https://doi.org/10.1080/21663831.2016.1257514.

[222] S.J. Sun, Y.Z. Tian, H.R. Lin, H.J. Yang, X.G. Dong, Y.H. Wang, Z.F. Zhang, Transition of twinning behavior in CoCrFeMnNi high entropy alloy with grain refinement, Mater. Sci. Eng. A. 712 (2018) 603–607. https://doi.org/10.1016/j.msea.2017.12.022.

[223] G. Dini, A. Najafizadeh, S.M. Monir-Vaghefi, R. Ueji, Grain size effect on the

martensite formation in a high-manganese TWIP steel by the Rietveld method, J. Mater. Sci. Technol. 26 (2010) 181–186. https://doi.org/10.1016/S1005-0302(10)60030-8.

[224] R. Ueji, N. Tsuchida, D. Terada, N. Tsuji, Y. Tanaka, A. Takemura, K. Kunishige, Tensile properties and twinning behavior of high manganese austenitic steel with fine-grained structure, Scr. Mater. 59 (2008) 963–966. https://doi.org/10.1016/j.scriptamat.2008.06.050.

[225] J. Su, X. Wu, D. Raabe, Z. Li, Deformation-driven bidirectional transformation promotes bulk nanostructure formation in a metastable interstitial high entropy alloy, Acta Mater. 167 (2019) 23–39. https://doi.org/10.1016/j.actamat.2019.01.030.

[226] Z. Yang, S. Lu, Y. Tian, Z. Gu, J. Sun, L. Vitos, Theoretical and experimental study of phase transformation and twinning behavior in metastable high-entropy alloys, J. Mater. Sci. Technol. 99 (2022) 161–168. https://doi.org/10.1016/j.jmst.2021.05.037.

[227] S. Wei, C.C. Tasan, Deformation faulting in a metastable CoCrNiW complex concentrated alloy: A case of negative intrinsic stacking fault energy?, Acta Mater. 200 (2020) 992–1007. https://doi.org/10.1016/j.actamat.2020.09.056.

[228] M. Shih, J. Miao, M. Mills, M. Ghazisaeidi, Stacking fault energy in concentrated alloys, Nat. Commun. 12 (2021) 1–10. https://doi.org/10.1038/s41467-021-23860-z.

[229] J.B. Baudouin, G. Monnet, M. Perez, C. Domain, A. Nomoto, Effect of the applied stress and the friction stress on the dislocation dissociation in face centered cubic metals, Mater. Lett. 97 (2013) 93–96.

https://doi.org/10.1016/j.matlet.2012.10.117.

[230] P. Delavignette, S. Amelinckx, Dislocation patterns in graphite, J. Nucl. Mater. 5 (1962) 17–66. https://doi.org/10.1016/0022-3115(62)90038-7.

[231] C.B. Carter, I.L.F. Ray, I.L. F Ray, On the stacking-fault energies of copper alloys, Philos. Mag. 35 (1977) 189–200. https://doi.org/10.1080/14786437708235982.

[232] D.T. Pierce, J. Bentley, J.A. Jiménez, J.E. Wittig, Stacking fault energy measurements of Fe-Mn-Al-Si austenitic twinning-induced plasticity steels, Scr. Mater. 66 (2012) 753–756. https://doi.org/10.1016/j.scriptamat.2012.01.050.

[233] H.M. Otte, D.O. Welch, Formation of stacking faults in polycrystalline silicon bronze under tensile deformation, Philos. Mag. 9 (1964) 299–313. https://doi.org/10.1080/14786436408229193.

[234] D. Rafaja, C. Krbetschek, C. Ullrich, S. Martin, Stacking fault energy in austenitic steels determined by using in situ X-ray diffraction during bending, J. Appl. Crystallogr. 47 (2014) 936–947. https://doi.org/10.1107/S1600576714007109.

[235] G.B. Olson, M. Cohen, A general mechanism of martensitic nucleation: Part I. General concepts and the FCC→HCP transformation, Metall. Trans. A. 7 (1976) 1897–1904. https://doi.org/10.1007/BF02654987.

[236] S.J. Lee, J. Han, C.Y. Lee, I.J. Park, Y.K. Lee, Elastic strain energy induced by epsilon martensitic transformation and its contribution to the stacking-fault energy of austenite in Fe-15Mn-xC alloys, J. Alloys Compd. 617 (2014) 588–

596. https://doi.org/10.1016/j.jallcom.2014.08.054.

[237] S.Y.S.I. Lee, S.Y.S.I. Lee, J. Han, B. Hwang, Deformation behavior and tensile properties of an austenitic Fe-24Mn-4Cr-0.5C high-manganese steel: Effect of grain size, Mater. Sci. Eng. A. 742 (2019) 334–343. https://doi.org/10.1016/j.msea.2018.10.107.

[238] S.F. Liu, Y. Wu, H.T. Wang, J.Y. He, J.B. Liu, C.X. Chen, X.J. Liu, H.T. Wang, Z.P. Lu, Stacking fault energy of face-centered-cubic high entropy alloys, Intermetallics. 93 (2018) 269–273. https://doi.org/10.1016/j.intermet.2017.10.004.

[239] N.L. Okamoto, S. Fujimoto, Y. Kambara, M. Kawamura, Z.M.T. Chen, H. Matsunoshita, K. Tanaka, H. Inui, E.P. George, Size effect, critical resolved shear stress, stacking fault energy, and solid solution strengthening in the CrMnFeCoNi high-entropy alloy, Sci. Rep. 6 (2016) 1–10. https://doi.org/10.1038/srep35863.

[240] S. Picak, J. Liu, C. Hayrettin, W. Nasim, D. Canadinc, K. Xie, Y.I. Chumlyakov, I. V. Kireeva, I. Karaman, Anomalous work hardening behavior of Fe40Mn40Cr10Co10 high entropy alloy single crystals deformed by twinning and slip, Acta Mater. 181 (2019) 555–569. https://doi.org/10.1016/j.actamat.2019.09.048.

[241] H. Huang, X. Li, Z. Dong, W. Li, S. Huang, D. Meng, X. Lai, T. Liu, S. Zhu, L. Vitos, Critical stress for twinning nucleation in CrCoNi-based medium and high entropy alloys, Acta Mater. 149 (2018) 388–396. https://doi.org/10.1016/j.actamat.2018.02.037.

[242] I. Kireeva, Y. Chumlyakov, Z. Pobedennaya, A. Vyrodova, I. Kuksgauzen, D.

Kuksgauzen, Twinning and critical resolved shear stresses for twinning in single crystals of high-entropy alloys, AIP Conf. Proc. 2051 (2018) 020123. https://doi.org/10.1063/1.5083366.

[243] A. Das, Revisiting Stacking Fault Energy of Steels, Metall. Mater. Trans. A. 47 (2016) 748–768. https://doi.org/10.1007/s11661-015-3266-9.

[244] M.H. Loretto, L.M. Clarebrough, R.L. Segall, Stacking-fault tetrahedra in deformed face-centred cubic metals, Philos. Mag. 11 (1965) 459–465. https://doi.org/10.1080/14786436508224233.

[245] F. Häussermann, M. Wilkens, Bestimmung der Stapelfehlerenergie kubisch-flächenzentrierter Metalle aus der Analyse des elektronenmikroskopischen Beugungskontrastes von Stapelfehlerdipolen, Phys. Status Solidi. 18 (1966) 609–624. https://doi.org/10.1002/pssb.19660180214.

[246] M.J. Mills, P. Stadelmann, M.J. Mills, A study of the structure of Lomer and 60° dislocations in aluminium using high-resolution transmission electron microscopy, Philos. Mag. A Phys. Condens. Matter, Struct. Defects Mech. Prop. 60 (1989) 355–384. https://doi.org/10.1080/01418618908213867.

[247] P. Mullner, P.J. Ferreira, On the energy of terminated stacking faults, Philos. Mag. Lett. 73 (1996) 289–298. https://doi.org/10.1080/095008396180551.

[248] K. V. Werner, F. Niessen, M. Villa, M.A.J. Somers, Experimental validation of negative stacking fault energies in metastable face-centered cubic materials, Appl. Phys. Lett. 119 (2021) 141902. https://doi.org/10.1063/5.0063761.

[249] W. Kohn, L.J. Sham, Self-consistent equations including exchange and

correlation effects, Phys. Rev. 140 (1965) 1133–1138. https://doi.org/10.1103/PhysRev.140.A1133.

[250] P. Hohenberg, W. Kohn, Inhomogeneous electron gas, Phys. Rev. 136 (1964) 864–871. https://doi.org/10.1007/s12045-017-0529-3.

[251] L. Vitos, The EMTO-CPA Method, in: Comput. Quantum Mech. Mater. Eng., 1st ed., Springer, London, 2007: pp. 83–94. https://doi.org/10.1007/978-1-84628-951-4_5.

[252] L. Vegard, Die Konstitution der Mischkristalle und die Raumfüllung der Atome, Zeitschrift Für Phys. 5 (1921) 17–26. https://doi.org/10.1007/BF01349680.

[253] G. Grimvall, Spin disorder in paramagnetic fcc iron, Phys. Rev. B. 39 (1989) 12300–12301. https://doi.org/10.1103/PhysRevB.39.12300.

[254] J.P. Perdew, K. Burke, M. Ernzerhof, Generalized gradient approximation made simple, Phys. Rev. Lett. 77 (1996) 3865–3868. https://doi.org/10.1103/PhysRevLett.77.3865.

[255] R. Li, S. Lu, D. Kim, S. Schönecker, J. Zhao, S.K. Kwon, L. Vitos, Stacking fault energy of face-centered cubic metals: Thermodynamic and ab initio approaches, J. Phys. Condens. Matter. 28 (2016) 395001. https://doi.org/10.1088/0953-8984/28/39/395001.

[256] S. Kibey, J.B. Liu, D.D. Johnson, H. Sehitoglu, Predicting twinning stress in fcc metals: Linking twin-energy pathways to twin nucleation, Acta Mater. 55 (2007) 6843–6851. https://doi.org/10.1016/j.actamat.2007.08.042.

[257] L. Liu, R. Wang, X. Wu, L. Gan, Q. Wei, Temperature effects on the

generalized planar fault energies and twinnabilities of Al, Ni and Cu: First principles calculations, Comput. Mater. Sci. 88 (2014) 124–130. https://doi.org/10.1016/j.commatsci.2014.03.005.

[258] Z.H. Jin, S.T. Dunham, H. Gleiter, H. Hahn, P. Gumbsch, A universal scaling of planar fault energy barriers in face-centered cubic metals, Scr. Mater. 64 (2011) 605–608. https://doi.org/10.1016/J.SCRIPTAMAT.2010.11.033.

[259] M. Wilkens, M. Rapp, K. Differt, Die Stapelfehlerenergie von Silber verschiedener Reinheit, Int. J. Mater. Res. 57 (1966) 746–750. https://doi.org/10.1515/ijmr-1966-571007.

[260] L.M. Clarebrough, P. Humble, M.H. Loretto, FAULTED DEFECTS AND STACKING-FAULT ENERGY, Can. J. Phys. 45 (1967) 1135–1146. https://doi.org/10.1139/p67-083.

[261] P.G.J. Gallagher, Y.C. Llu, The diversity of stacking fault energy determinations and its significance, Acta Metall. 17 (1969) 127–137. https://doi.org/10.1016/0001-6160(69)90133-3.

[262] M.H. Loretto, L.M. Clarebrough, R.L. Segall, The stacking-fault energy of silver, Philos. Mag. 10 (1964) 731–732. https://doi.org/10.1080/14786436408228492.

[263] L.F. Vassamillet, T.B. Massalski, Stacking fault probabilities of some alloys of copper and silver with zinc and cadmium, J. Appl. Phys. 34 (1963) 3398–3402. https://doi.org/10.1063/1.1729199.

[264] P.R. Thornton, T.E. Mitchell, P.B. Hirsch, The dependence of cross-slip on stacking-fault energy in face-centred cubic metals and alloys, Philos. Mag. 7

(1962) 1349–1369. https://doi.org/10.1080/14786436208213168.

[265] L.E. Murr, Relative interfacial free energy measurements in Cu and Cu-Al alloys, Phys. Status Solidi. 3 (1970) 447–455. https://doi.org/10.1002/pssa.19700030219.

[266] M. Walter, L. Mujica Roncery, S. Weber, L. Leich, W. Theisen, XRD measurement of stacking fault energy of Cr–Ni austenitic steels: influence of temperature and alloying elements, J. Mater. Sci. 55 (2020) 13424–13437. https://doi.org/10.1007/s10853-020-04953-4.

[267] L.E. Murr, Temperature coefficient of twin-boundary energy: The determination of stacking-fault energy from the coherent twin-boundary energy in pure F.C.C. metals, Scr. Metall. 6 (1972) 203–208. https://doi.org/10.1016/0036-9748(72)90168-8.

[268] R.H. Rautioaho, An Interatomic Pair Potential for Aluminium Calculation of Stacking Fault Energy, Phys. Status Solidi. 112 (1982) 83–89. https://doi.org/10.1002/pssb.2221120108.

[269] P. Humble, M.H. Loretto, L.M. Clarebrough, The nature of defects in quenched nickel, Philos. Mag. 15 (1967) 297–303. https://doi.org/10.1080/14786436708227702.

[270] C.B. Carter, S.M. Holmes, The stacking-fault energy of nickel, Philos. Mag. 35 (1977) 1161–1171. https://doi.org/10.1080/14786437708232942.

[271] P.C.J. Gallagher, J. Washburn, The stacking-fault energy in the Ag-In series, Philos. Mag. 14 (1966) 971–978. https://doi.org/10.1080/14786436608244768.

[272] A.W. Ruff, L.K. Ives, Dislocation node determinations of the stacking fault energy in silver-tin alloys, Acta Metall. 15 (1967) 189–198. https://doi.org/10.1016/0001-6160(67)90191-5.

[273] TISONE TC, SUNDAHL RC, CHIN GY, STACKING FAULT ENERGY IN NOBLE METAL ALLOYS, Met Trans. 1 (1970) 1561–1567. https://doi.org/10.1007/bf02642001.

[274] T. Jøssang, J.P. Hirth, The energies of stacking-fault teirahedra in F.C.C. metals, Philos. Mag. 13 (1966) 657–670. https://doi.org/10.1080/14786436608212687.

[275] C.B. Carter, S.M. Holmes, The study of faulted dipoles in copper using weak-beam electron microscopy, Philos. Mag. 32 (1975) 599–614. https://doi.org/10.1080/14786437508220883.

[276] R.C. Perrin, E.J. Savino, Computer simulation of weak-beam images of extended dislocations in copper, J. Microsc. 98 (1973) 214–220. https://doi.org/10.1111/j.1365-2818.1973.tb03826.x.

[277] A. Howie, P.R. Swann, Direct measurements of stacking-fault energies from observations of dislocation nodes, Philos. Mag. 6 (1961) 1215–1226. https://doi.org/10.1080/14786436108243372.

[278] J.A. Venables, The electron microscopy of deformation twinning, J. Phys. Chem. Solids. 25 (1964) 685–692. https://doi.org/10.1016/0022-3697(64)90177-5.

[279] M.J. Szczerba, M.S. Szczerba, Slip versus twinning in low and very low stacking-fault energy Cu-Al alloy single crystals, Acta Mater. 133 (2017)

109–119. https://doi.org/10.1016/j.actamat.2017.05.011.

[280] Y.Z. Tian, L.J. Zhao, S. Chen, A. Shibata, Z.F. Zhang, N. Tsuji, Significant contribution of stacking faults to the strain hardening behavior of Cu-15%Al alloy with different grain sizes, Sci. Rep. 5 (2015) 2–10. https://doi.org/10.1038/srep16707.

[281] T. Mori, H. Fujita, TWINNING DEFORMATION IN SINGLE CRYSTALS OF Cu-8 at%Al ALLOY., Trans Jpn Inst Met. 18 (1977) 17–24. https://doi.org/10.2320/matertrans1960.18.17.

[282] P.C.J. Gallagher, The influence of alloying, temperature, and related effects on the stacking fault energy, Metall. Trans. 1 (1970) 2429–2461. https://doi.org/10.1007/BF03038370.

[283] T.C. Tisone, J.O. Brittain, M. Meshii, Stacking Faults in a Cu-15 at% Al Alloy. I. The Short Range Order and Temperature Dependence of the Stacking Fault Energy, Phys. Status Solidi. 27 (1968) 185–194. https://doi.org/10.1002/pssb.19680270119.

[284] Y. Tomokiyo, K. Kaku, T. Eguchi, The Influence of Solute Atoms on the Stacking Fault Energy in αCu–Al Alloys, Trans. Japan Inst. Met. 15 (1974) 39–45. https://doi.org/10.2320/matertrans1960.15.39.

[285] K. Kamada, Effects of annealing and irradiation on the stacking-fault energy of CuSingle Bond signAl solid solutions, J. Appl. Phys. 39 (1968) 1824–1828. https://doi.org/10.1063/1.1656437.

[286] F. Tranchant, J. Vergnol, J. Grilhé, Twinning in α Cu-A1 Crystals: An

Instability of Plastic Flow, in: Strength Met. Alloy. (ICSMA 8), Pergamon, 1989: pp. 167–172. https://doi.org/10.1016/b978-0-08-034804-9.50021-8.

[287] J.W. Christian, S. Mahajan, Deformation twinning, Prog. Mater. Sci. 39 (1995) 1–157. https://doi.org/10.1016/0079-6425(94)00007-7.

[288] L. Li, Z. Chen, S. Kuroiwa, M. Ito, K. Kishida, H. Inui, E.P. George, Tensile and compressive plastic deformation behavior of medium-entropy Cr-Co-Ni single crystals from cryogenic to elevated temperatures, Int. J. Plast. 148 (2022) 103144. https://doi.org/10.1016/j.ijplas.2021.103144.

[289] P.R. Thornton, T.E. Mitchell, Deformation twinning in alloys at low temperatures, Philos. Mag. 7 (1962) 361–375. https://doi.org/10.1080/14786436208212171.

[290] O. Vöhringer, Der Einfluss von Legierungsart und Konzentration auf die Streckgrenze von α -Kupferlegierungen, Zeitschrift Für Met. 65 (1974) 352–358.

[291] Z. Wu, H. Bei, G.M. Pharr, E.P. George, Temperature dependence of the mechanical properties of equiatomic solid solution alloys with face-centered cubic crystal structures, Acta Mater. 81 (2014) 428–441. https://doi.org/10.1016/j.actamat.2014.08.026.

[292] A. Gali, E.P. George, Tensile properties of high- and medium-entropy alloys, Intermetallics. 39 (2013) 74–78. https://doi.org/10.1016/j.intermet.2013.03.018.

[293] F. Otto, A. Dlouhý, C. Somsen, H. Bei, G. Eggeler, E.P. George, The influences of temperature and microstructure on the tensile properties of a

CoCrFeMnNi high-entropy alloy, Acta Mater. 61 (2013) 5743–5755. https://doi.org/10.1016/j.actamat.2013.06.018.

[294] M. Naeem, H. He, F. Zhang, H. Huang, S. Harjo, T. Kawasaki, B. Wang, S. Lan, Z. Wu, F. Wang, Y. Wu, Z. Lu, Z. Zhang, C.T. Liu, X.L. Wang, Cooperative deformation in high-entropy alloys at ultralow temperatures, Sci. Adv. 6 (2020) 4002–4029. https://doi.org/10.1126/sciadv.aax4002.

[295] S. Yoshida, T. Bhattacharjee, Y. Bai, N. Tsuji, Friction stress and Hall-Petch relationship in CoCrNi equi-atomic medium entropy alloy processed by severe plastic deformation and subsequent annealing, Scr. Mater. 134 (2017) 33–36. https://doi.org/10.1016/j.scriptamat.2017.02.042.

[296] Z. Wu, H. Bei, F. Otto, G.M. Pharr, E.P. George, Recovery, recrystallization, grain growth and phase stability of a family of FCC-structured multi-component equiatomic solid solution alloys, Intermetallics. 46 (2014) 131–140. https://doi.org/10.1016/j.intermet.2013.10.024.

[297] X. Wu, D. Mayweg, D. Ponge, Z. Li, Microstructure and deformation behavior of two TWIP/TRIP high entropy alloys upon grain refinement, Mater. Sci. Eng. A. 802 (2021) 140661. https://doi.org/10.1016/j.msea.2020.140661.

[298] S. Allain, J.P. Chateau, O. Bouaziz, A physical model of the twinning-induced plasticity effect in a high manganese austenitic steel, Mater. Sci. Eng. A. 387–389 (2004) 143–147. https://doi.org/10.1016/j.msea.2004.01.060.

[299] S. Curtze, V.T. Kuokkala, Dependence of tensile deformation behavior of TWIP steels on stacking fault energy, temperature and strain rate, Acta Mater. 58 (2010) 5129–5141. https://doi.org/10.1016/j.actamat.2010.05.049.

[300] D. Molnár, G. Engberg, W. Li, S. Lu, P. Hedström, S.K. Kwon, L. Vitos, Experimental study of the γ-surface of austenitic stainless steels, Acta Mater. 173 (2019) 34–43. https://doi.org/10.1016/j.actamat.2019.04.057.

[301] K. V. Werner, F. Niessen, W. Li, S. Lu, L. Vitos, M. Villa, M.A.J. Somers, Reconciling experimental and theoretical stacking fault energies in face-centered cubic materials with the experimental twinning stress, Materialia. 27 (2023) 101708. https://doi.org/10.1016/j.mtla.2023.101708.

[302] Z. Wang, W. Lu, F. An, M. Song, D. Ponge, D. Raabe, Z. Li, High stress twinning in a compositionally complex steel of very high stacking fault energy, Nat. Commun. 13 (2022) 1–8. https://doi.org/10.1038/s41467-022-31315-2.

[303] X. Jin, T. Nakamoto, S. Harjo, T. Hemmi, T. Umeno, T. Ogitsu, A. Yamamoto, M. Sugano, K. Aizawa, J. Abe, W. Gong, T. Iwahashi, Development of a cryogenic load frame for the neutron diffractometer at Takumi in Japan Proton Accelerator Research Complex, Rev. Sci. Instrum. 84 (2013) 063106. https://doi.org/10.1063/1.4810010.

[304] R. Oishi-Tomiyasu, M. Yonemura, T. Morishima, Application of matrix decomposition algorithms for singular matrices to the Pawley method in Z-Rietveld, J. Appl. Crystallogr. 45 (2012) 299–308. https://doi.org/10.1107/S0021889812003998.

[305] C. Wagner, G. Laplanche, Effects of stacking fault energy and temperature on grain boundary strengthening, intrinsic lattice strength and deformation mechanisms in CrMnFeCoNi high-entropy alloys with different Cr/Ni ratios, Acta Mater. 244 (2023) 118541.

https://doi.org/10.1016/j.actamat.2022.118541.

[306] K.M. Rahman, V.A. Vorontsov, D. Dye, The effect of grain size on the twin initiation stress in a TWIP steel, Acta Mater. 89 (2015) 247–257. https://doi.org/10.1016/j.actamat.2015.02.008.

[307] L. Tang, L. Wang, M. Wang, H. Liu, S. Kabra, Y. Chiu, B. Cai, Synergistic deformation pathways in a TWIP steel at cryogenic temperatures: In situ neutron diffraction, Acta Mater. 200 (2020) 943–958. https://doi.org/10.1016/j.actamat.2020.09.075.

[308] I. V. Kireeva, Y.I. Chumlyakov, A. V. Vyrodova, Z. V. Pobedennaya, I. Karaman, Effect of twinning on the orientation dependence of mechanical behaviour and fracture in single crystals of the equiatomic CoCrFeMnNi high-entropy alloy at 77K, Mater. Sci. Eng. A. 784 (2020) 139315. https://doi.org/10.1016/j.msea.2020.139315.

[309] I. V. Kireeva, Y.I. Chumlyakov, Z. V. Pobedennaya, A. V. Vyrodova, I. Karaman, Twinning in [001]-oriented single crystals of CoCrFeMnNi high-entropy alloy at tensile deformation, Mater. Sci. Eng. A. 713 (2018) 253–259. https://doi.org/10.1016/j.msea.2017.12.059.

[310] I. V. Kireeva, Y.I. Chumlyakov, Z. V. Pobedennaya, A. V. Vyrodova, I. V. Kuksgauzen, D.A. Kuksgauzen, Orientation and temperature dependence of a planar slip and twinning in single crystals of Al0.3CoCrFeNi high-entropy alloy, Mater. Sci. Eng. A. 737 (2018) 47–60. https://doi.org/10.1016/j.msea.2018.09.025.

[311] W. Abuzaid, H. Sehitoglu, Critical resolved shear stress for slip and twin nucleation in single crystalline FeNiCoCrMn high entropy alloy, Mater.

Charact. 129 (2017) 288–299. https://doi.org/10.1016/j.matchar.2017.05.014.

[312] A.J. Zaddach, C. Niu, C.C. Koch, D.L. Irving, Mechanical properties and stacking fault energies of NiFeCrCoMn high-entropy alloy, Jom. 65 (2013) 1780–1789. https://doi.org/10.1007/s11837-013-0771-4.

[313] S. Huang, W. Li, E. Holmström, S.K. Kwon, O. Eriksson, L. Vitos, Plastic deformation transition in FeCrCoNiAlx high-entropy alloys, Mater. Res. Lett. 7 (2019) 439–445. https://doi.org/10.1080/21663831.2019.1644683.

[314] E.P. George, W.A. Curtin, C.C. Tasan, High entropy alloys: A focused review of mechanical properties and deformation mechanisms, Acta Mater. 188 (2020) 435–474. https://doi.org/10.1016/j.actamat.2019.12.015.

[315] R.E. Kubilay, W.A. Curtin, Theory of twin strengthening in fcc high entropy alloys, Acta Mater. 216 (2021) 117119. https://doi.org/10.1016/j.actamat.2021.117119.

[316] S. Pramanik, A.A. Gazder, A.A. Saleh, E. V. Pereloma, Nucleation, coarsening and deformation accommodation mechanisms of ε-martensite in a high manganese steel, Mater. Sci. Eng. A. 731 (2018) 506–519. https://doi.org/10.1016/j.msea.2018.06.024.

[317] S. Wei, M. Xu, J.M. LeBeau, C.C. Tasan, Tuning mechanical metastability in FeMnCo medium entropy alloys and a peek into deformable hexagonal close-packed martensite, Appl. Phys. Lett. 119 (2021) 261905. https://doi.org/10.1063/5.0079981.

DTU Construct

Section of Materials and Surface Engineering
Produktionstorvet, Bld. 425
2800 Kongens Lyngby

www.construct.dtu.dk

ISBN: 978-87-7475-758-0